Aus dem Institut für Molekular- und Zellbiologie der Hochschule Mannheim
(Direktor: Prof. Dr. rer. nat. Mathias Hafner)

Dissecting population and single-cell heterogeneity in response to anti-cancer drugs

Inauguraldissertation
zur Erlangung des Doktor scientiarum humanarum (Dr. sc. hum.)
der
Medizinischen Fakultät Mannheim
der Ruprecht-Karls-Universität
zu
Heidelberg

vorgelegt von
Saman Honarnejad

aus
Teheran, Iran
2017

Dekan: Prof. Dr. med. Sergij Goerdt
Referent: Prof. Dr. rer. nat. Mathias Hafner

TABLE OF CONTENTS

1. INTRODUCTION 7
  1.1 Challenges to drug discovery and patient care 7
    1.1.1 High risk of failure in current drug discovery paradigm 7
    1.1.2 Variability in patient responses to anti-cancer drugs 8
    1.1.3 Cell-to-cell variability in responses to anti-cancer drugs 10
    1.1.4 Aims and approaches 13
2. MATERIALS AND METHODS 15
  1.2 Materials 15
    1.2.1 Cell culture 15
    1.2.2 Ligand and kinase inhibitors 15
    1.2.3 Antibodies 16
    1.2.4 Chemical reagents 21
      1.2.4.1 Bleaching reagents 21
      1.2.4.2 Lysis buffer for western blot 21
  1.3 METHODS 21
    1.3.1 Western blot 21
    1.3.2 ELISA 22
    1.3.3 High-content immunofluorescence (IF) imaging 24
    1.3.4 Highly multiplexed cyclic immunofluorescence (CycIF) imaging 27
      1.3.4.1 CycIF image processing 31
      1.3.4.2 CycIF data analysis 32
    1.3.5 Analysis and statistics 32
      1.3.5.1 Parameterization of dose-response curves 32
      1.3.5.2 Multiparametric analysis of dose-response curves 35
      1.3.5.3 Principal component analysis (PCA) 37
      1.3.5.4 *K*-means clustering 37
      1.3.5.5 viSNE (Stochastic Neighboring Embedding) 38
      1.3.5.6 Wanderlust 38
3. RESULTS 39
  1.4 Dissecting population averaged drug response 39
    1.4.1 Results from high-content immunofluorescence (IF) imaging and biochemical methods 39

1.4.1.1 Multiparametric analysis of dose-response curves....................................39
1.4.1.2 Averaged signal-response parameters..41
1.4.1.3 Dynamics of MAP kinase signaling in response to EGFR inhibitors.........42
1.4.1.4 Dynamics of drug target inhibition...47
1.4.1.5 Drug combination to overcome recovery..50
1.4.1.6 Principal component analysis of drug response data................................52
1.5 Dissecting single-cell level variability in drug response 56
1.5.1 Results from high-content immunofluorescence (IF) imaging............. 56
1.5.1.1 Fractional analysis of signal-response curves 56
1.5.1.2 Single-cell visualization of cytostatic states 58
1.5.2 Results from cyclic immunofluorescence (CycIF) imaging 60
1.5.2.1 *K*-means clustering in PCA space..60
1.5.2.2 viSNE visualization of drug response data 63
1.5.2.3 Fractional analysis in viSNE space 68
1.5.2.4 Wanderlust visualization of steady states..69
4. DISCUSSION 72
5. SUMMARY 83
6. ZUSAMMENFASSUNG 86
7. REFERENCES... 89
8. APPENDIX 96
1.6 List of figures 96
1.7 List of tables.. 98
1.8 List of equations 98
1.9 Publications derived from this work 98
9. CURRICULUM VITAE.. 99
10. ACKNOWLEDGMENT.. 101

LIST OF ABBREVIATIONS

ng/mL	Nanogram per mililiter
µg/mL	Microgram per mililiter
µM	Micromolar
mM	Milimolar
M	Molar
AKT	Protein kinase B (PKB)
AUC	Area Under the Curve
CDK	Cyclin-dependent Kinase
CDKI	Cyclin-dependent kinase inhibitor
CycIF	Cyclic immunofluorescence
E_{50}	Half-maximal effect
EC_{50}	Half-maximal effective concentration
EDTA	Ethylenediaminetetraacetic acid
EGF	Epidermal growth factor
EGFR	Epidermal growth factor receptor
E_{max}	Maximal effect
ERK	Extracellular-signal-regulated kinase
FBS	Fatal bovine serum
FSC	Flow cytometry standard
GI_{50}	Half-maximal growth Inhibition
H_2O_2	Hydrogen peroxide
HER2	Human epidermal growth factor receptor 2
HPLC	High performance liquid chromatography
HS	Hill slope
HTS	High-throughput screening
IC_{50}	Half-maximal inhibitory effect
IF	Immunofluorescence
KCl	Potassium chloride
KH_2PO_4	Monopotassium phosphate

MAPK	Mitogen-activated protein kinases
MEK	Mitogen-activated protein kinase kinase
MS	Mass spectrometry
mTOR	Mechanistic target of rapamycin
Na_2HPO_4	Disodium phosphate
NaCl	Sodium chloride
NaOH	Sodium hydroxide
NMEs	New molecular entities
PBS	Phosphate-buffered saline
PCA	Principal component analysis
PCs	Principal components
PMSF	Phenylmethylsulfonyl fluoride
R&D	Research and development
ROI	Region of interest
SDS	Sodium dodecyl sulfate
STN	Signal-to-Noise ratio
TSCs	Tumor stem cells
viSNE	t-distributed stochastic neighbor embedding

1. INTRODUCTION

1.1 Challenges to drug discovery and patient care

1.1.1 High risk of failure in current drug discovery paradigm

Drug discovery and development is costly, time consuming and extremely risky. Estimates suggest that it costs about $1 billion to successfully discover, develop and launch a single new drug in the market. About 80% of this cost belongs to R&D expenditure, most of which is consumed by failures at different stages of drug discovery and development pipeline, raising questions about productivity and the possible flaws in current drug discovery paradigm (Figure 1.1) (Bains, 2004; Earm and Earm, 2014).

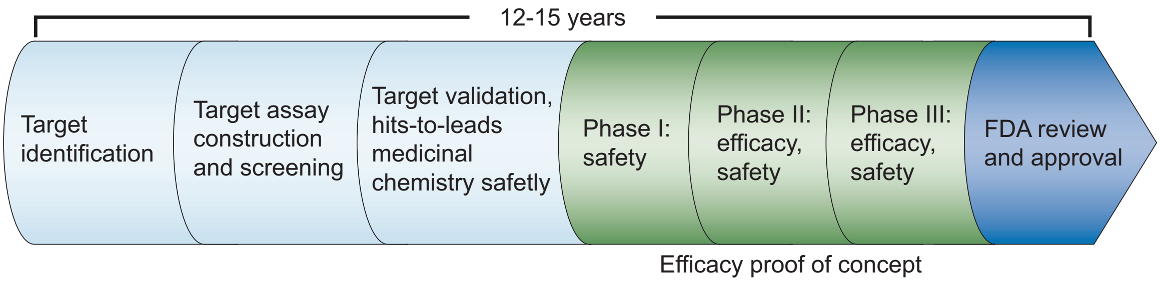
12-15 years
Target identification
Target assay construction and screening
Target validation, hits-to-leads medicinal chemistry safetly
Phase I: safety
Phase II: efficacy, safety
Phase III: efficacy, safety
FDA review and approval
Efficacy proof of concept

Figure 1.1 Drug discovery and development paradigm.
In much generalized format, a potential target for a given disease is identified and HTS assays are constructed to find chemical agents that modulate the target activity. The target is validated through secondary screens and hits are optimized to lead compounds by extensive medicinal chemistry programs and animal testing. Efficacy and safety of potential drug candidates are then evaluated in different phases of clinical development before approval by the regulatory agencies. Adapted from previously published work (Roses, 2008).

Development and utilization of high-throughput screening methods has drastically increased the number of chemical agents entering early clinical trials. However, most lead compounds that progress through high-throughput screening campaigns and medicinal chemistry studies fail to pass clinical trials typically due to lack of potency or safety (Hughes et al., 2011). It has been suggested that one way to avoid the high cost of failures is “quick win, fast fail” drug development paradigm, where technical advances in genomic and proteomic profiling methods as well as novel systems and quantitative modeling approaches are leveraged in early stages of drug development to process the potential drug candidates resulting in a reduced number of new molecular entities (NMEs) advancing into late phases of clinical trials, but those that do advance have a higher probability of success and launch (Paul et al., 2010).

1.1.2 Variability in patient responses to anti-cancer drugs

Over the past two decades, huge investments by large pharmaceutical companies has led to successful development and approval of a considerable number of targeted therapies for use in oncology and immune therapy (Arora and Scholar, 2005; Hoelder et al., 2012; Yegnasubramanian and Maitra, 2013; Zhang et al., 2009). In most types of cancers, patient stratification is the key to the use of targeted therapies, because only subsets of cancers of any type have the signaling dependencies that kinase inhibitors and similar drugs aim to inhibit (Hanahan and Weinberg, 2011). However, even in stratified patient groups a primary challenge facing development and use of such new medicines is patient-to-patient variability in responses to even the most potent and targeted therapeutics. While the focus of classic pharmacology has been on drug-target interactions and structure-activity relationships, advances in affordable genomic sequencing of patient-derived cancer tissue biopsies has led to development of an entirely new branch in pharmacology called “pharmacogenomics” with the hope of tailored and personalized cancer care. Interestingly, patient-to-patient variability is also common in mechanisms of drug resistance or relapse in originally drug-naïve populations (Yang et al., 2010).

A recent approach to understanding such variability involves genotyping a large and diverse bank (‘encyclopedia’) of patient-derived cell lines to cover the complex mutational landscapes within cancer types and subtypes, coupled with systematic measurement of drug-response across them (Barretina et al., 2012). In the case of anti-cancer drugs that block cell proliferation or induce apoptosis (Tyson et al., 2012), cells are typically exposed to drugs over a 10^4 - to 10^5 -fold concentration range, and after 72–96 hours relative viability is quantitated typically by measuring viability surrogates such as ATP content. Such data is conventionally analyzed from the perspective of IC_{50} values (or similar parameters), which are descriptive of the shape of the dose-response curve at its midpoint. However, inspection of dose-response curves reveals that they differ substantially in shape from one drug to the next and from one cell line to the next. Thus, the focus to date on potency (Garnett et al., 2012; Heiser et al., 2012) ignores the potential impact and biological importance of variation in other parameters, such as the steepness of the dose-response curve or differences in maximum effect (Figure 1.2) (Fallahi-Sichani et al., 2013).

Mutations and nongenetic factors that generate dose-response curves with $HS < 1$ and $E_{max} > 0$ are likely to be important clinically. The incremental therapeutic benefit of getting closer and closer to the maximum tolerated dose will be less for a drug with a shallow rather than steep dose-response curve. Studies on dose-response relationships for antiviral drugs have also concluded that variation in HS is important for assessing drug sensitivity and resistance. Attempts to identify new drugs or effective combination therapies might therefore focus on steepening the dose-response relationship and increasing maximum effect, not just decreasing IC_{50} (Fallahi-Sichani et al., 2013).

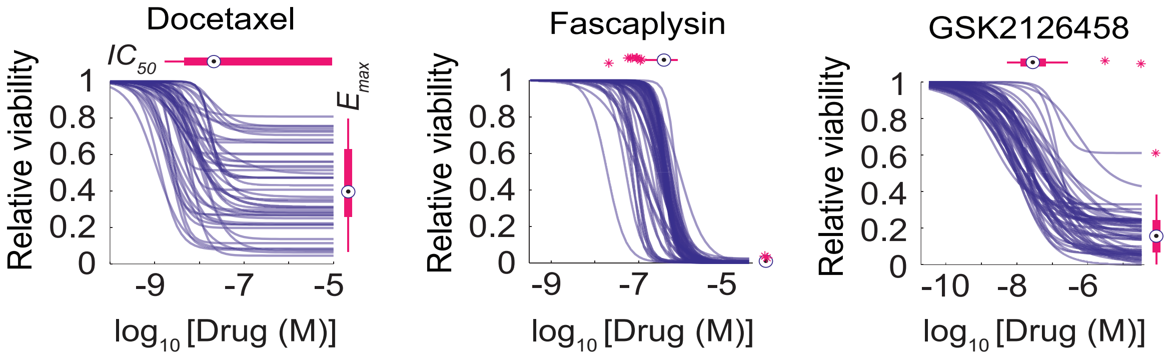

Figure 1.2 Variability in shape of drug-response behavior in breast cancer cell line.

Examples of response to anti-cancer drugs. Analysis of response to Docetaxel (anti-mitotic and microtubule stabilizing), Fascaplysin (CDK4/6 inhibitor) and GSK2126458 (PI3K inhibitor) implicate distinct dose response behaviors across 55 cancer cell lines. In Docetaxel, variability can be seen clearly at the levels of IC_{50}*,* E_{max} *and hill slope (HS) but Fascaplysin shows most variability at the level of* IC_{50} *and no variability at the level of* E_{max} *or hill slope in comparison to GSK2126458 which shows minor variability in Emax and most variability at the level of HS (Fallahi-Sichani et al., 2013).*

1.1.3 Cell-to-cell variability in responses to anti-cancer drugs

Drug action inside of a tumor rarely affects all cells in the same way, leaving opportunities for individual cells to escape and give rise to relapse and possibly resistance. While much of cell-to-cell variability in drug responses likely originates from genetic heterogeneity (Michor and Polyak, 2010), and existence of drug tolerant tumor stem cells (TSCs) (Hanahan and Weinberg, 2011), a large number of diverse studies have reported striking fate variability even in genetically identical, clonal cells in culture. Using quantitative single-cell imaging, fate variability has been traced to stochastic changes in protein concentrations that influence switching between cellular programs (Levin et al., 2011; Spencer et al., 2009) or variable positioning in the cell cycle (Yano et al., 2014). It is therefore crucial to systematically monitor how cancer cell subpopulations emerge, shift or vanish from the cellular signaling landscape in response to drug treatment (Figure 1.3).

To best of our knowledge, cell-to-cell variability in drug induced cell fate decision-making has been described primarily in compounds and ligands that induce apoptosis (Flusberg and Sorger, 2013; Spencer et al., 2009) but therapeutics that lead to induction of cytostasis have largely been unexplored.

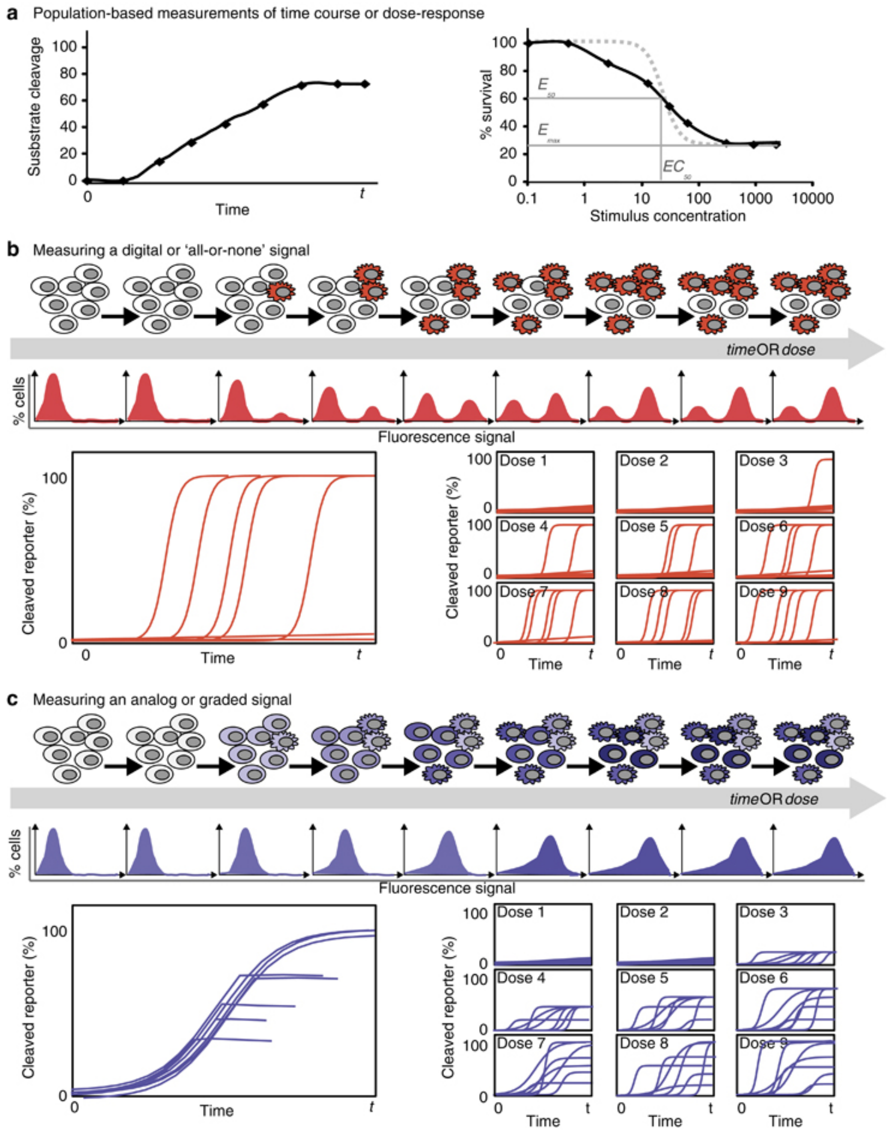

Figure 1.3 Characteristics of heterogeneous and homogeneous signaling responses for different forms of measurements.

(a) Schematic representations of population-level measurements of signaling and apoptosis over time (left) or for a dose response (right). These are expected to be similar whether the cells respond heterogeneously or homogeneously. Dose-response curves can be characterized by potency (IC_{50}*), the maximal effectiveness (*E_{max}*), the half-point of effectiveness (*E_{50}*) and the concentration at *EC_{50}*. (b-c) Schematic representations of hypothetical results of various single-cell end point measurements such as flow cytometry and dynamic*

measurements for time-dependent or dose-dependent data series. Although these are all consistent with the hypothetical population-level measurements shown in a, they illustrate how population-based measurements can fail to distinguish between heterogeneous all-or-none signals (b) and homogeneous graded signals (c)(Xia et al., 2014).

1.1.4 Aims and approaches

Currently, the main approaches to drug discovery are phenotypic screening and target-based screening. The former evaluates the induced phenotypic effects of compounds on cells and the latter measures either the binding of compounds to a purified target protein or activity of the target protein in response to compounds (Hughes et al., 2011; Reguera et al., 2014). Historically, drug discovery was driven by phenotypic screening, often with limited knowledge of biochemical and molecular details of diseases, but more recently specially in cancer therapy, advances in genomics has led to identification of druggable target candidates in the genome, making target-centric approaches more popular. Conventional phenotypic assays are typically low in throughput and only use bulk measurements of population average to examine drug responses. Target-based approaches are high in throughput but lack physiological environments to probe compound pharmacodynamics in the cellular context. Indeed, it has been argued that too much focus on genetic approaches to validate targets for use in target-based drug discovery has resulted in reduced success in discovering first-in-class medicines (Hoelder et al., 2012; Samsdodd, 2005).

Understanding the mechanisms of action of therapeutic drugs requires characterization of drug-induced changes in intracellular state. In the case of targeted anti-cancer drugs these typically involve inhibition of oncogene signaling, changes in cell cycle distribution and induction of senescence or apoptosis. Multiplex methods are required to monitor this diversity and the methods described in this thesis illustrate that microscopy is ideal for this purpose. We argue that cell-based measurements of target and close-to-target protein states (phospho-states) and abundance with automated multiplexed high-content and high-throughput microscopy methods, not only combines the advantages of both phenotypic and target-based approaches (in the case of engineered cell lines), but also allows assessment of single-cell drug responses. Single-cell profiling uncovers relationships between target inhibition and induction of cellular phenotypes that are obscured by population average methods and it fits well into the workflow of drug discovery. It can also be very economical with respect to reagents and numbers of cells (an important consideration with patient-derived materials). To this end, we propose utilization of an automated high-content immunofluorescence (IF) combined with a novel highly multiplexed cyclic immunofluorescence (CycIF) single-cell imaging method instead of conventional HTS techniques that only use bulk measurements of population average to address issues of potency and efficacy of chemical agents early in preclinical studies with an emphasis on single-cell pharmacodynamics.

2. MATERIALS AND METHODS

1.2 Materials

1.2.1 Cell culture

MCF10A, BT474, SkBr3, hMEC, H1666, H1650 and H3255 cell lines were obtained directly from the American Type Culture Collection (ATCC), 21PT and 21MT1 cells were obtained from Gray lab and HMLE and HMLER cells were obtained from Weinberg lab. MCF10A, 21PT and 21MT1 cell lines were cultured under conventional conditions in DMEM/F12 (Invitrogen) supplemented with 5% (v/v) horse serum, EGF (20 ng/ml), insulin (10 µg/ml), hydrocortisone (0.5 µg/ml), and cholera toxin (100 ng/ml) with penicillin (50 U/ml) and streptomycin (50 µg/ml) and beside BT474 cell line that was grown in RPMI media supplemented with 10% (v/v) FBS and penicillin (50 U/ml) and streptomycin (50 µg/ml), the rest of the cell lines were cultured according to ATCC culture methods.

1.2.2 Ligand and kinase inhibitors

EGF ligand was purchased from PeproTech (Cat. No. AF-100-15) and the small molecule drugs Dactolisib (NVP-BEZ235), Torkinib (PP242), Gefitinib, Erlotinib, MK2206, Triciribine, Selumetinib (AZD6244) and PD0325901 were purchased from Selleck Chemicals and Lapatinib from LC laboratories. All compounds were dissolved in DMSO as 10 mM stock solutions. For drug dose-response, ~5,000 cells for MCF10a, 21PT and 21MT1 cells or ~15,000 cells for the rest of the cell lines were plated per well in two replicate 96-well plates (Corning) in full growth media for 24 hours and then either starved over night and treated with EGF or in full serum treated with drugs for 24-48 h. For perturbations and their nominal targets see Figure 2.1.

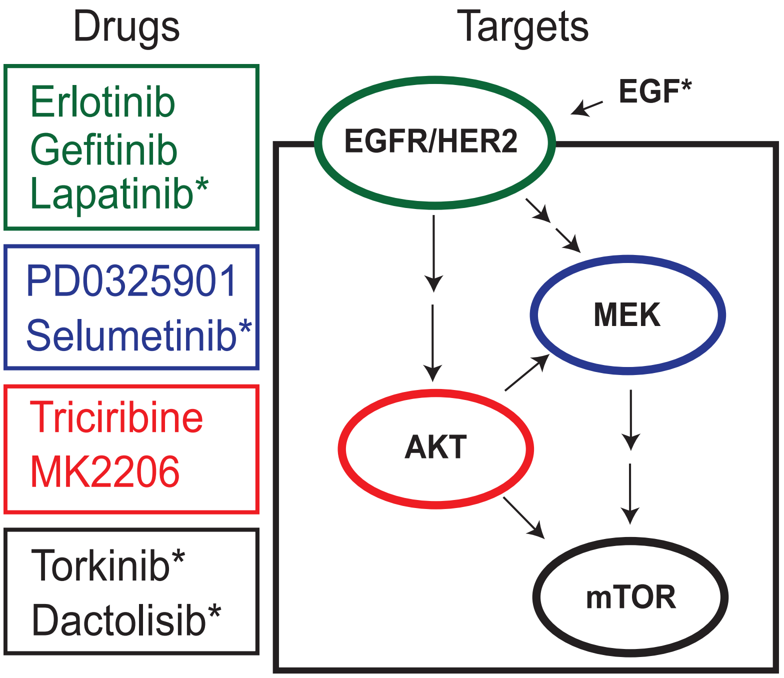
Drugs
Targets
Erlotinib
Gefitinib
Lapatinib*
PD0325901
Selumetinib*
Triciribine
MK2206
Torkinib*
Dactolisib*
EGF*
EGFR/HER2
MEK
AKT
mTOR

Figure 2.1 Nominal targets of ligand and kinase inhibitor panel.

Epidermal growth factor (EGF) binds to the extracellular domain of epidermal growth factor receptor (EGFR) causing homo- (with itself) or hetero- (with other receptors like human epidermal growth factor receptor 2) dimerization and autophosphorylation of the kinase domain. This activity leads to binding to downstream adaptor proteins and activation of MAPK and PI3K/AKT signaling pathways. Erlotinib, Gefitinib and Lapatinib compete with ATP and inhibit the kinase activity of EGFR. Lapatinib is a dual kinase inhibitor and in addition to EGFR it also inhibits the kinase activity of HER2 (human epidermal growth factor receptor 2). PD0325901 and Selumetinib (AZD6244) inhibit MAPK signaling by targeting MEK. Triciricbine and MK2206 inhibit different subunits of AKT. Torkinib (PP242) is an mTOR targeting drug and Dactolisib is a dual inhibitor of PI3K and mTOR.

1.2.3 Antibodies

Antibody validation is not a straightforward process and we typically rely on commercial antibodies already in wide spread use. In studies of cell signaling, antibody selectivity in a particular cell type is assessed using activating extracellular ligands in combination with kinase inhibitors. In principle many primary antibodies that work for use in biochemical methods such as western blotting, do not work well for immunofluorescence. One reason for this issue is that in western blotting, proteins are fully denatured after being exposed to detergents likes SDS but in immunofluorescence, antibodies might not reach their specific epitopes due to protein folding that remains intact after fixation.

For the purpose of testing and validating relevant antibodies for the targets of interest in this study, MCF10a cells were starved overnight and exposed to EGF at 8 doses in serum-free media for 24 hours. Conventional four-color immunofluorescence was used to characterize cells stained with the DNA dye Hoechst 33342 to label nuclei and one of the 30 different primary antibodies (Figure 2.2).

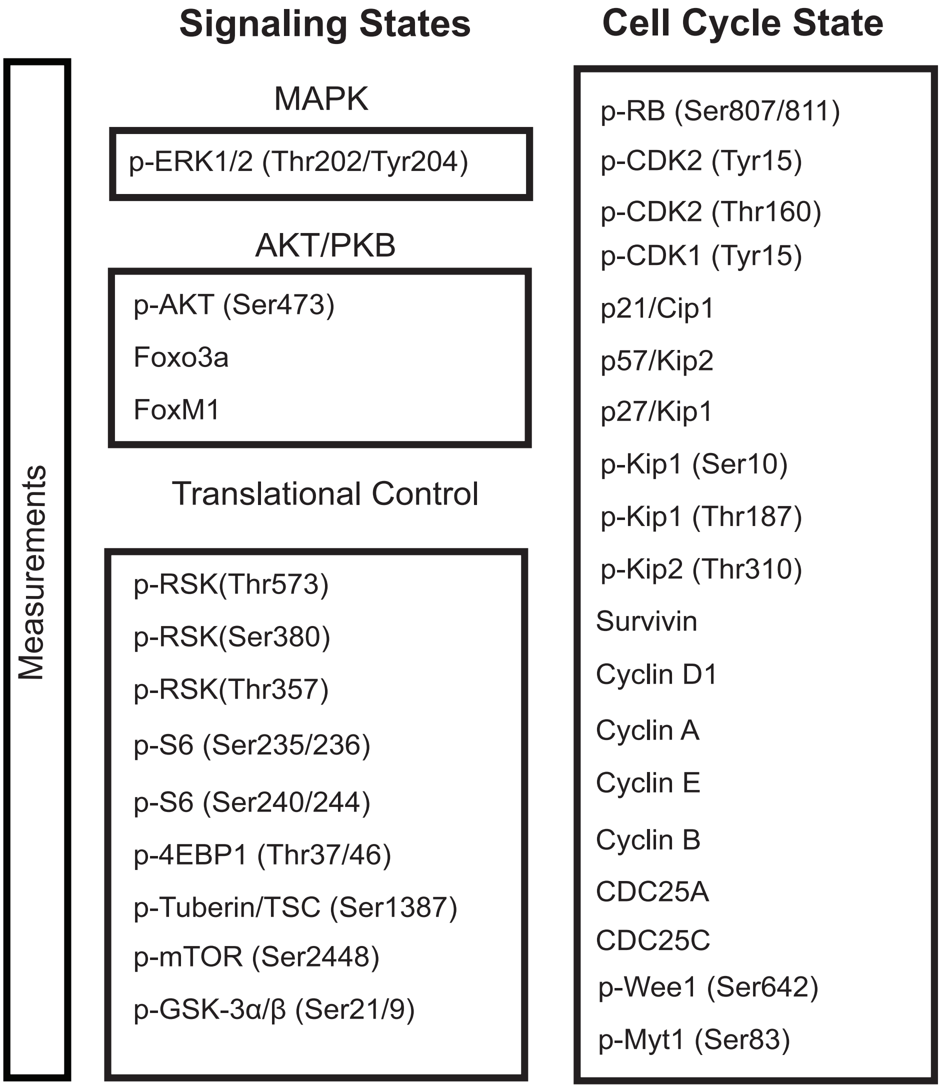
Signaling States
Cell Cycle State
Measurements
MAPK
p-ERK1/2 (Thr202/Tyr204)
AKT/PKB
p-AKT (Ser473)
Foxo3a
FoxM1
Translational Control
p-RSK(Thr573)
p-RSK(Ser380)
p-RSK(Thr357)
p-S6 (Ser235/236)
p-S6 (Ser240/244)
p-4EBP1 (Thr37/46)
p-Tuberin/TSC (Ser1387)
p-mTOR (Ser2448)
p-GSK-3α/β (Ser21/9)
p-RB (Ser807/811)
p-CDK2 (Tyr15)
p-CDK2 (Thr160)
p-CDK1 (Tyr15)
p21/Cip1
p57/Kip2
p27/Kip1
p-Kip1 (Ser10)
p-Kip1 (Thr187)
p-Kip2 (Thr310)
Survivin
Cyclin D1
Cyclin A
Cyclin E
Cyclin B
CDC25A
CDC25C
p-Wee1 (Ser642)
p-Myt1 (Ser83)

Figure 2.2 Antibodies tested for immunofluorescence imaging.
Antibodies specific to total or phosphorylated levels of different proteins that regulate signaling pathways such as those controlling MAPK, AKT or translational control as well as those specific to cell cycle regulation were probed by measuring their dynamic range in response to increasing doses of EGF.

From the tested antibodies, 20 markers showed acceptable STN ratio and we used these antibodies for drug screen using conventional immunofluorescence imaging (Figure 2.3).

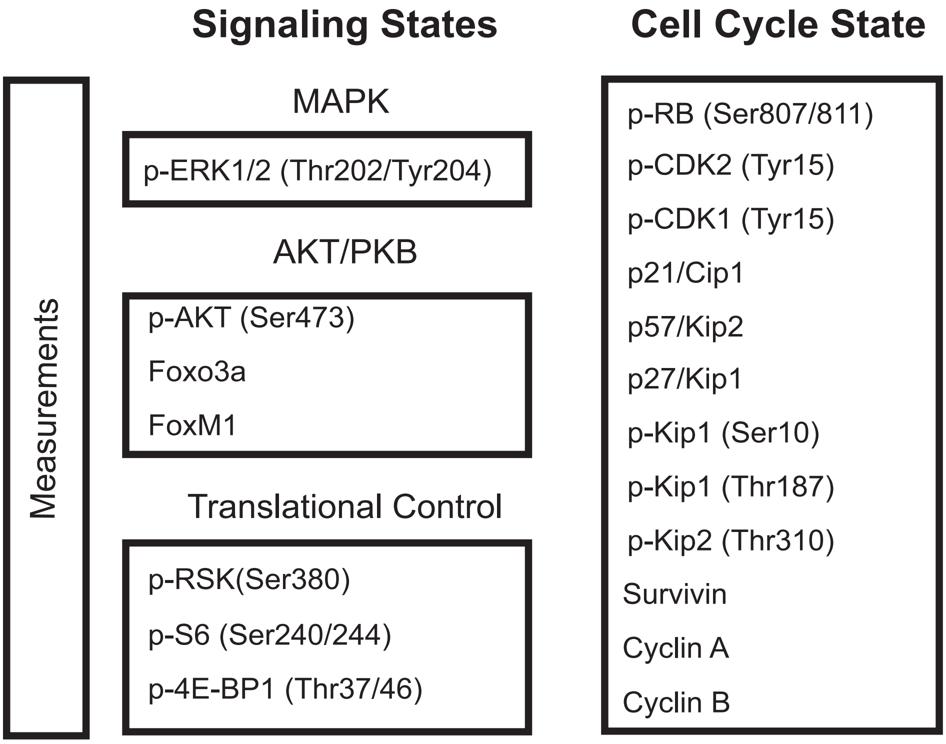
Signaling States
Cell Cycle State
Measurements
MAPK
p-ERK1/2 (Thr202/Tyr204)
AKT/PKB
p-AKT (Ser473)
Foxo3a
FoxM1
Translational Control
p-RSK(Ser380)
p-S6 (Ser240/244)
p-4E-BP1 (Thr37/46)
p-RB (Ser807/811)
p-CDK2 (Tyr15)
p-CDK1 (Tyr15)
p21/Cip1
p57/Kip2
p27/Kip1
p-Kip1 (Ser10)
p-Kip1 (Thr187)
p-Kip2 (Thr310)
Survivin
Cyclin A
Cyclin B

Figure 2.3 Antibodies used for high-content immunofluorescence imaging and drug screening.

Antibodies specific to total or phosphorylated levels of different proteins that regulate signaling pathways such as those controlling MAPK, AKT or translational control as well as those specific to cell cycle regulation were used in drug screen using conventional immunofluorescence imaging.

For the purpose of testing and validating relevant antibodies to for the targets of interest to be used in CycIF method, MCF10a cells were either starved for 24 hours and then treated with EGF at different concentrations or exposed to one of the four kinase inhibitors (denoted in Figure 2.1 with a star) in full serum and then subjected to CycIF staining (Figure 2.4). 20-channel images were registered against nuclei to align images from successive cycles, segmented and single-cell features were extracted using ImageJ software (Abràmoff et al., 2004) corresponding to whole cell, membrane, cytoplasmic and nuclear intensities.

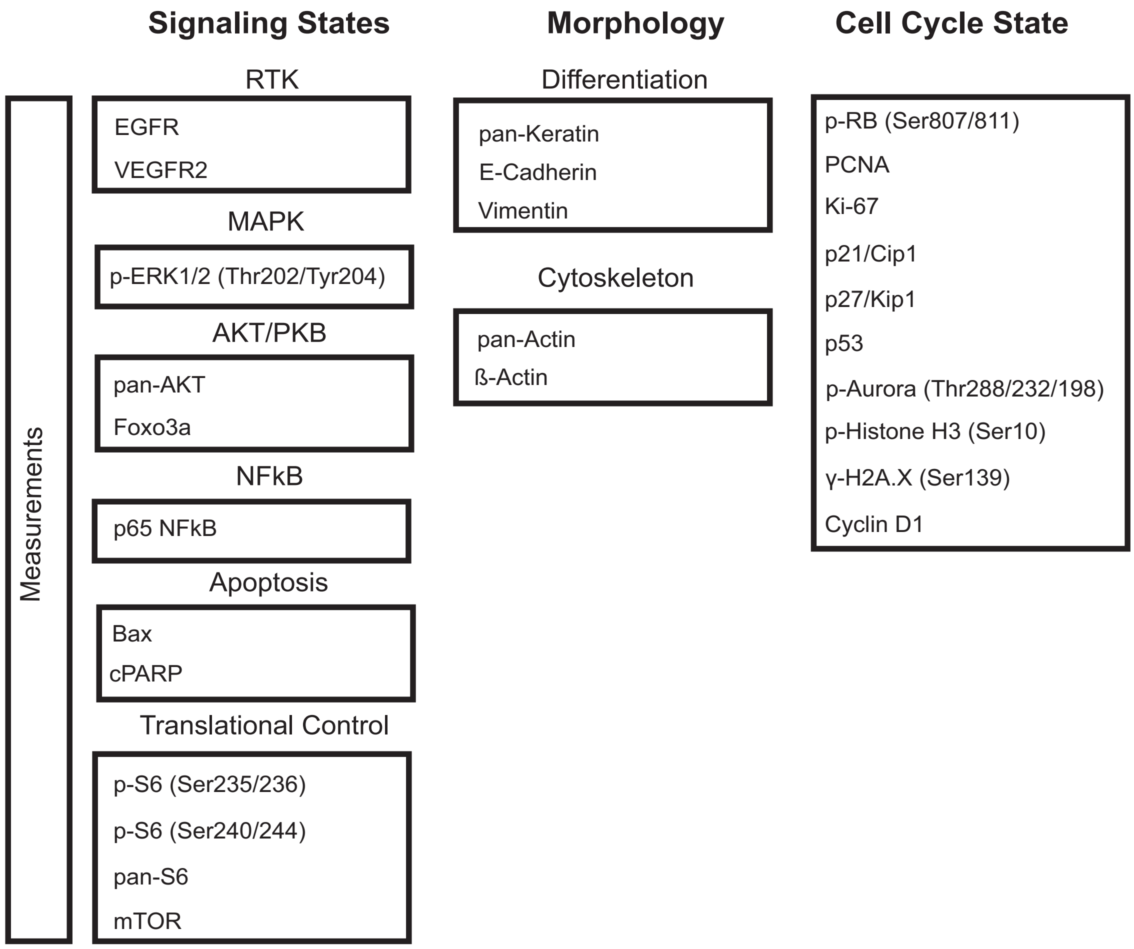
Signaling States
Morphology
Cell Cycle State
Measurements
RTK
EGFR
VEGFR2
MAPK
p-ERK1/2 (Thr202/Tyr204)
AKT/PKB
pan-AKT
Foxo3a
NFkB
p65 NFkB
Apoptosis
Bax
cPARP
Translational Control
p-S6 (Ser235/236)
p-S6 (Ser240/244)
pan-S6
mTOR
Differentiation
pan-Keratin
E-Cadherin
Vimentin
Cytoskeleton
pan-Actin
ß-Actin
p-RB (Ser807/811)
PCNA
Ki-67
p21/Cip1
p27/Kip1
p53
p-Aurora (Thr288/232/198)
p-Histone H3 (Ser10)
γ-H2A.X (Ser139)
Cyclin D1

Figure 2.4 Antibodies used for cyclic immunofluorescence (CycIF) ligand response and drug screen.

Antibodies specific to total or phosphorylated levels of different proteins that regulate signaling pathways such as those controlling MAPK, AKT, NFkB, apoptosis or translational control as well as those specific to cell differentiation, cytoskeleton and cell cycle regulation were used for EGF ligand and drug screening using CycIF.

1.2.4 Chemical reagents

1.2.4.1 Bleaching reagents

140 µl of fluorophore inactivation solution containing 3% H_2O_2 and 20 mM NaOH in PBS (137 mM NaCl, 2.7 mM KCl, 10 mM Na_2HPO_4 and 1.8 mM KH_2PO_4; pH ≈ 9.5) was added to each well and the samples were continuously illuminated with an ordinary incandescent table lamp. Fluorophore inactivation was monitored using a Cytell Imaging system in continued presence of the oxidation solution. When inactivation was complete (typically 60 min) cells were washed three times with 250 µl PBS using BioTek EL406 plate washer and then incubated with Odyssey Blocking Buffer (OBB) for an hour. After blocking, samples were subjected to the next round of staining, as described above. H_2O_2 was obtained as a 30% solution from Sigma (Cat. No. H1009), NaOH as pellets (Cat. No. S5881), and hydrochloric acid as a 37% (12 M) solution (Cat. No. 258148) (Lin et al., 2015).

1.2.4.2 Lysis buffer for western blot

1% Triton lysis buffer was prepared by adding 1 mL of Triton X-100 (10%) to 9 mL of PBS. 1 pellet of mini complete protease inhibitor (1 tablet per 10 mL) was added to the solution with 10 mM final EDTA concentration. 20 mM BME was added to the final solution.

1.3 METHODS

1.3.1 Western blot

Cells were seeded in 6-well plates and treated with Lapatinib the next day. At desired time points, the media was aspirated and cells were washed with 1 mL of ice cold PBS. PBS was aspirated completely and 150 µL of ice-cold Triton lysis buffer was added to the wells. The plates were left on ice for 20 mins and scraped occasionally. The lysates were collected from the wells and transferred to eppendorf tubes. Tubes were spun at maximum speed for 10 mins in cold room. The lysates were removed from the nuclear pellet, added to new tubes and normalized using Bradford assay. The normalized sample lysates were added to tubes containing (5x) standard buffer (SB), boiled for 1 min and stored at -80°C.

Lysates were fed into precast gels and ran in 1x SDS running buffer. Gels were transferred in transfer buffer to membranes pre soaked in 100% methanol over night in cold room. The next day membranes were blocked with Odyssey Blocking Buffer for 1 hour at room temperature with gentle shaking. Blocking buffer was aspirated and primary antibodies were added to the membranes according to vendor's recommended dilution for western blot application in Odyssey Blocking Buffer plus 0.1% Tween-20 and incubated for 2 hours at room temperature with gentle shaking. Membranes were washed 5 times for 5 mins each round with generous amounts of PBS plus 0.1% Tween-20 with gentle shaking. Secondary IRDye antibodies were diluted (1:20,000) in Odyssey Blocking Buffer plus 0.1% Tween-20 and incubated with the membranes for 1 hour with gentle shaking and protected from light. Membranes were washed 5 times for 5 mins each round with generous amounts of PBS plus 0.1% Tween-20 with gentle shaking. Finally, membranes were soaked in 1x PBS and scanned on Odyssey Infrared imaging system.

1.3.2 ELISA

Lysis buffer was prepared immediately before use and kept on ice at all times.150-200 µl/well was used in 6-well plate. IC Diluent #12 (dilute Sample Diluent Concentrate 2x diluted with an equal volume of water) + 1:140 aprotinin + 1:1000 LPC + 1:100 Thermo Halt phosphatase inhibitor cocktail + 1:500 PMSF (500 mM stock) IC Diluent #12 = 1% NP-40, 20 mM Tris (pH 8.0), 137 mM NaCl, 10% glycerol, 2 mM EDTA, 1 mM activated sodium orthovanadate. Plates were put on ice and quickly washed with ice-cold PBS. PBS was aspirated and the lysis buffer was added. Cells were scraped off the plates and put in eppendorf tubes. They were kept on ice during this time and rocked gently on ice for 30 minutes at 4°C. Then microcentrifuged at 14,000 *g* for 5 minutes at 4°C and the supernatant was slowly transferred into clean eppendorf tubes, making sure sample is well mixed and aliquotted if needed and stored at -80°C.

Capture antibody was reconstituted if needed and then vortexed. Appropriate amount of diluted capture antibody was prepared in PBS without carrier protein. Immediately 100 µl was pipetted into each desired well. Plates were sealed and incubated overnight at room temperature and gently agitated on rocker. The final concentrations of the used capture antibodies were 0.4 µg/ml for EGFR and 7 µg/ml for HER2. Blocking solution was brought to room temperature to be used. Capture antibody was aspirated followed by washing four times with 400 µl/well 1x PBS-T (0.05% Tween-20 in PBS) and once with 1x PBS. Wash buffer was gently agitated for 0.5 – 2 min before removing. After the last wash, plates were inverted on clean paper towel and aspirated. 300 µl/well of blocking solution was pipetted followed by incubation at room temperature with gentle agitation for 1-2 hours. 2 ug/well primary antibody for p-EGFR, 40 µg/well for p-HER2 was pipetted. The blocking buffer was aspirated followed by washing four times with 400 µl/well 1x PBS-T (three times for the total protein assays) and once with 1x PBS. After the last wash, plates were inverted on clean paper towel and aspirated. 100 µl/well of the samples were added in IC Diluent #12. Plates were seal and incubated for 2 hours at room temperature on rotator. Standards and samples were aspirated, followed by washing four times with 400 µl/well 1x PBS-T (three times for the total protein assays) and once with 1x PBS. Detection antibody (p-EGFR and p-HER2 at 1:200 dilution) was prepared in IC Diluent #14 and 100 µl/well was pipetted. Plates were sealed and incubated overnight at 4°C with continued rocking. The next day, wells were washed four times with 400 µl/well of 1x PBS-T and once with 1x PBS. After the last wash, plates were inverted on clean paper towel and aspirated. Donkey anti-Rabbit HRP-conjugated antibody in IC Diluent #14 (p-EGFR = 1:40,000, p-HER2 = 1:5,000) was prepared and 100 µl/well pipetted. Plates were sealed and incubated for 2 hours at room temperature rocking. Substrate solution was warmed to room temperature before use. Plates were washed four times with 400 µl/well 1x PBS-T and once with 1x PBS, followed by gentle agitation of wash buffer for 1-2 min before removing. After the last wash, plates were inverted on clean paper towel and aspirated. 100 µl/well substrate solution was added (1:1 Substrate Reagents A & B; mixed together within 15 minutes of use and protect from light) to wells. After 20 minutes incubation at room temperature, 50 µl/well stop solution was added to wells followed by pipetting up and down to mix and samples were quantified using a plate reader (Kleiman et al., 2011).

1.3.3 High-content immunofluorescence (IF) imaging

Cells were fixed in 2% paraformaldehyde for 10 min at room temperature and washed with PBS-T (0.1% Tween-20, Sigma-Aldrich), permeabilized in methanol for 10 min at room temperature, washed with PBS-T, and blocked in Odyssey Blocking Buffer (OBB, LI-COR Biosciences) for 1 hour at room temperature. Cells were incubated overnight at 4°C with primary monoclonal antibodies from rabbit, goat, or mouse in OBB (Figure 2.3, Table 1 for more details). Cells were washed three times in PBS-T and incubated with fluor-conjugated secondary antibodies against rabbit, goat, or mouse IgG diluted 1:2,000 in OBB (Table 2). Cells were washed once in PBS-T, once in PBS and incubated in 250 ng/ml Hoechst 33342 (Invitrogen) and 1:500 Whole Cell Stain Blue (Thermo Scientific) solutions. Cells were then washed twice with PBS and imaged with a 10x objective on Operetta automated epifluorescence microscope (PerkinElmer) (Table 3). Automated image segmentation and single-cell quantification of stain intensities was performed using standard routines implemented in Columbus and Harmony (PerkinElmer, Figure 2.5). For illustration purposes, representative images were RGB-transformed and merged using ImageJ (Abràmoff et al., 2004).

Table 1 List of primary antibodies for ligand and drug response.

Host	Antibody	Target residue	Dilution	Vendor
Rabbit	phospho-RSK	Ser-380	1:200	GeneTex
Rabbit	Phosphor-ERK1/2	Thr202/Tyr204	1:400	Cell Signaling
Rabbit	phospho-Akt	Ser473	1:400	Cell Signaling
Rabbit	Foxo3a	Total	1:400	Cell Signaling
Rabbit	phospho-S6	Ser235/236	1:400	Cell Signaling
Rabbit	phospho-4E-BP1	Thr37/46	1:400	Cell Signaling
Rabbit	phospho-CDK2	Tyr15	1:400	GeneTex
Rabbit	phospho-CDC2	Tyr15	1:200	Cell Signaling
Rabbit	phospho-p57Kip2	Thr310	1:200	Cell Signaling
Rabbit	phospho-p27Kip1	Ser10	1:200	GeneTex
Rabbit	phospho-p27Kip1	Thr187	1:200	Santa Cruz
Rabbit	Survivin	Total	1:800	Cell Signaling
Rabbit	p27kip1	Total	1:200	Cell Signaling
Rabbit	p21Cip1	Total	1:400	Cell Signaling
Rabbit	P57Kip2	Total	1:200	Cell Signaling
Rabbit	FoxM1	Total	1:400	Cell Signaling
Rabbit	Cyclin A	Total	1:200	Santa Cruz
Rabbit	Cyclin B1	Total	1:400	Cell Signaling
Goat	phospho-Rb	Ser807/811	1:400	Santa Cruz
Mouse	p27Kip1	Total	1:200	Becton Dickenson

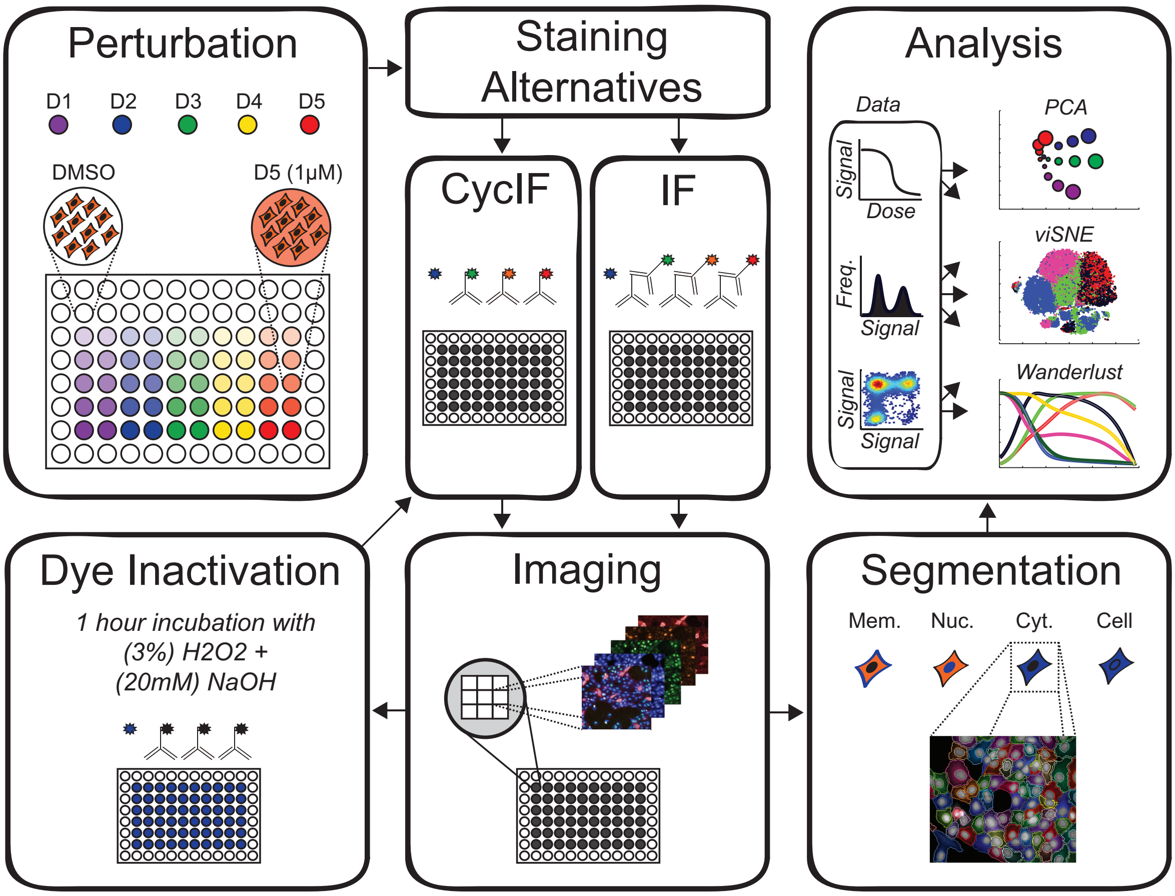
Perturbation
D1
D2
D3
D4
D5
DMSO
D5 (1μM)
Staining Alternatives
CycIF
IF
Analysis
Data
Signal
Dose
Freq.
Signal
Signal
Signal
PCA
viSNE
Wanderlust
Dye Inactivation
1 hour incubation with
(3%) H2O2 +
(20mM) NaOH
Imaging
Segmentation
Mem.
Nuc.
Cyt.
Cell

Figure 2.5 High-content/high-throughput IF and CycIF imaging pipeline. *Multi-well plates with cells that were perturbed with increasing doses of different drugs are fixed at desired time points and stained with a DNA dye and primary and then secondary antibodies for IF pipeline or alternatively with primary antibodies conjugated with alexa-fluor dyes for CycIF pipeline. Plates are scanned on an automated high-throughput epifluorescence microscope and images are segmented for IF or registered after each round of staining and segmented for CycIF. Single-cell features from different cellular compartments are generated and multiplexed high-dimensional data from mean and single-cell dose response curves are used for statistical analysis and high-dimensional visualization.*

Table 2 List of secondary antibodies for ligand and drug response.

Host	**Dye**	**Dilution**	**Vendor**
Donkey	Alexa-647	1:2000	Invitrogen
Donkey	Alexa-488	1:2000	Invitrogen
Donkey	Alexa-568	1:2000	Invitrogen

Table 3 List of filters used for IF imaging.

Filter	**Wavelength**
Excitation	360-400
Excitation	460-490
Excitation	560-580
Excitation	620-640
Emission	410-480
Emission	500-550
Emission	590-640
Emission	650-700

1.3.4 Highly multiplexed cyclic immunofluorescence (CycIF) imaging

Cells were fixed in 4% paraformaldehyde for 30 min at room temperature and washed three times with PBS, permeabilized in ice-cold methanol for 10 min at room temperature, rewashed with PBS, and blocked in Odyssey blocking buffer (LI-COR) for 1 hour at room temperature. Cells were incubated overnight at 4°C with primary antibodies in blocking buffer. For staining with fluorophore-conjugated primary antibodies, cells were washed three times with PBS and stained with Hoechst 33342 (0.1 µg/ml) for 15 min at room temperature. For primary antibodies that were not fluorophore-conjugated (i.e. for indirect immunofluorescence), cells were washed three times with PBS, incubated with fluorophore-conjugated secondary antibodies in blocking buffer for 1 hour at room temperature, washed with PBS and then stained with Hoechst 33342 for 15 min at room temperature. After image acquisition, cells were washed three times with PBS (250 µl per well) using BioTek EL406 plate washer with final aspiration so as to empty each well. 100 µl of a mixture of 3% H_2O_2 and 20 mM NaOH in PBS (137 mM NaCl, 2.7 mM KCl, 10 mM Na_2HPO_4 and 1.8 mM KH_2PO_4) (pH ≈ 9.5) were added to each well for 1 hour at room temperature and continuously illuminated with an ordinary incandescent table lamp. To monitor for fluorophore inactivation, remaining fluorescence was measured on a microscope prior to removal of the oxidation solution. Cells were then washed three times with 250 µl PBS using a plate washer and reincubated with blocking buffer. After blocking, samples were subjected to the next round of staining, as described above. H_2O_2 was obtained as a 30% solution from Sigma (Cat. No. H1009), NaOH as pellets (Cat. No. S5881), and hydrochloric acid as a 37% (12 M) solution (Cat. No. 258148) (Lin et al., 2015).

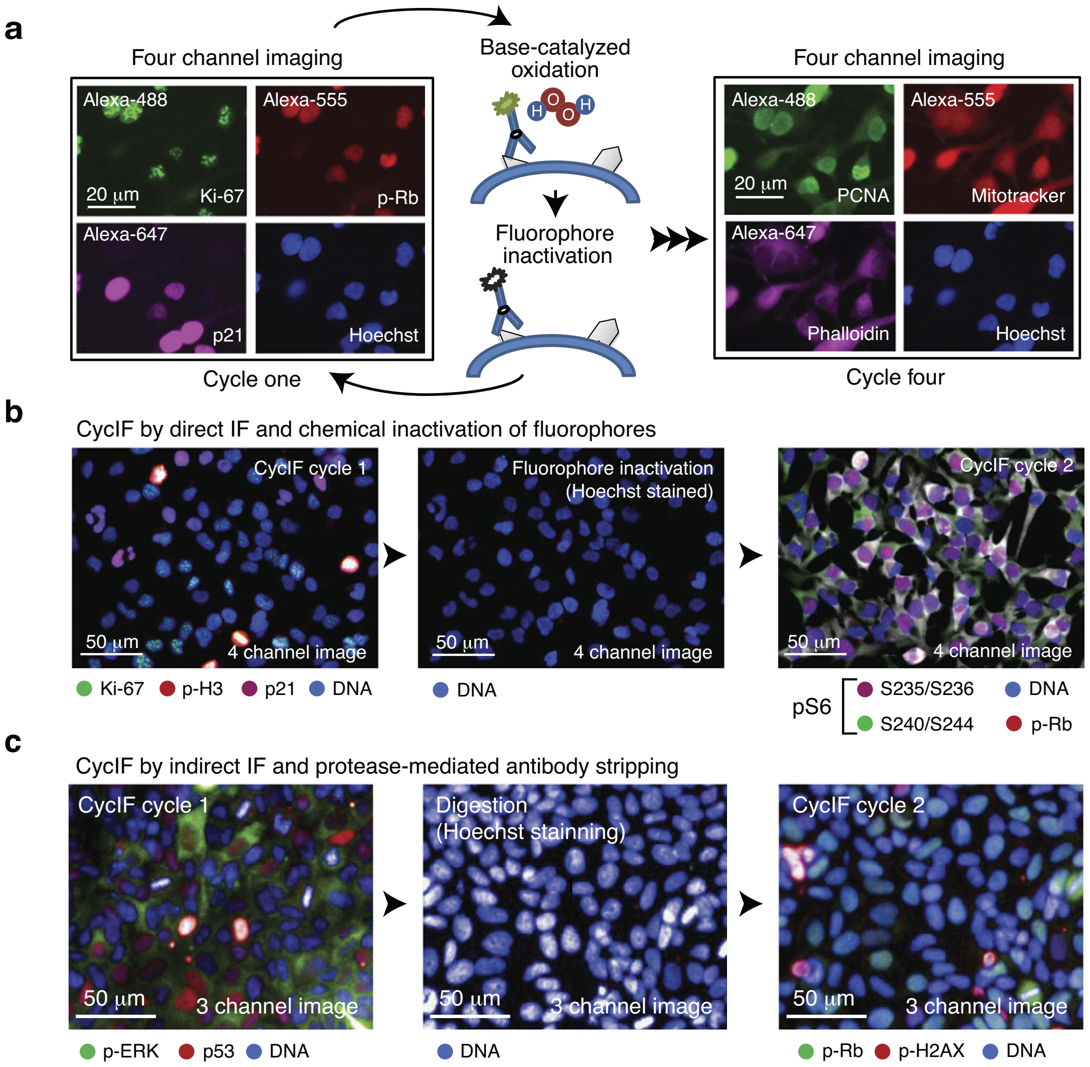
a
Four channel imaging
Alexa-488
Ki-67
20 μm
Alexa-555
p-Rb
Alexa-647
p21
Hoechst
Cycle one
Base-catalyzed oxidation
Fluorophore inactivation
Four channel imaging
Alexa-488
20 μm
PCNA
Alexa-555
Mitotracker
Alexa-647
Phalloidin
Hoechst
Cycle four
b
CycIF by direct IF and chemical inactivation of fluorophores
CycIF cycle 1
50 μm
4 channel image
Fluorophore inactivation (Hoechst stained)
50 μm
4 channel image
CycIF cycle 2
50 μm
4 channel image
● Ki-67 ● p-H3 ● p21 ● DNA
● DNA
pS6 ● S235/S236 ● S240/S244
● DNA ● p-Rb
c
CycIF by indirect IF and protease-mediated antibody stripping
CycIF cycle 1
50 μm
3 channel image
Digestion (Hoechst stainning)
50 μm
3 channel image
CycIF cycle 2
50 μm
3 channel image
● p-ERK ● p53 ● DNA
● DNA
● p-Rb ● p-H2AX ● DNA

Figure 2.6 CycIF imaging method variants.

(a) An overview of the CycIF procedure. Four-color staining alternates with fluorophore inactivation by oxidation to progressively build a multichannel image. (b) CycIF procedure using direct immunofluorescence (with fluorophore-conjugated antibodies) and chemical inactivation of fluorophores. COLO858 melanoma cells were fixed and stained using antibodies for Ki-67 (Alexa 488), p-Histone H3 (Alexa 555), p21/Cip1 (Alexa 647) and Hoechst (left panel). Cells were exposed to fluorophore-inactivation by oxidation using hydrogen peroxide, high pH and light and then reimaged (middle panel) to confirm efficient bleaching. Cells were then stained with fluorophore-conjugated antibodies for p-S6$^{S240/244}$ (Alexa 488), p-Rb$^{S807/811}$ (Alexa 555), p-S6$^{S235/236}$ (Alexa 647) and Hoechst. (c)

CycIF procedure using indirect immunofluorescence and protease-mediated antibody stripping. MCF7 cells were fixed and stained using primary antibodies for p-ERK1/2$^{T202/Y204}$ (rabbit), p53 (mouse), Alexa 488-conjugated anti-rabbit, and Alexa 647-conjugated anti-mouse secondary antibodies (left panel). Cells were digested with pepsin/papain mixture and reimaged (middle panel). Cells were restained using primary antibodies for p-Rb$^{S807/811}$ (rabbit), p-Histone H2A.X^{S139} (mouse), Alexa 488-conjugated anti-rabbit, and Alexa 647 conjugated anti-mouse secondary antibodies (right panel) (Lin et al., 2015).

Table 4 List of conjugated antibodies used in CycIF.

	Alexa-488/FITC	**Alexa-555/Cy3**	**Alexa-647/Cy5**
Cycle 1	p53 Antibody (DO-1, sc-126) Dilution 1:400	ActinRed 555 (Invitrogen #R371112, Lot #1646656)	FoxO3a (75D8) Rabbit mAb (CST #2497, Lot #10) Dilution 1:400
Cycle 2	p-ERK1/2 T202/Y204 (CST #4344, Lot #12) Dilution: 1:200	p-Rb S807/S811 (CST #8957, Lot #1) Dilution: 1:400	p21 Waf1/Cip1 (CST #8587, Lot #3) Dilution: 1:200
Cycle 3	Cyclin D1 (AB #AB190194, Lot #GR199456-1) Dilution: 1:400	p-AuroraABC (CST #13464, Lot #1) Dilution: 1:200	p27 (AB #AB194234, Lot #GR200274-1) Dilution: 1:400
Cycle 4	p-S6 S240/S244 (CST #5018, Lot #4) Dilution: 1:800	p-Histone H3 S10 (CST #3475, Lot #2) Dilution: 1:800	p-S6 S235/S236 (CST #4851, Lot #22) Dilution: 1:400
Cycle 5	Bax (BIO #633603, Lot #B169774) Dilution: 1:400	S6 (CST #6989, Lot #2) Dilution: 1:200	p-H2.AX S139 (BIO #613407, Lot #B199199) Dilution: 1:400

Cycle 6	PCNA (CST #8580, Lot #1) Dilution: 1:400	pan-Keratin (CST #3478, Lot #4) Dilution: 1:200	pan-Akt (CST #5186, Lot #3) Dilution: 1:400
Cycle 7	EGFR (CST #5616, Lot #4) Dilution: 1:400	VEGFR2 (CST #12872, Lot #1) Dilution: 1:400	mTOR (CST #5048, Lot #2) Dilution: 1:300
Cycle 8	E-Cadherin (CST #3199, Lot #11) Dilution: 1:200	β-Actin (CST #8046, Lot #1) Dilution: 1:200	Vimentin (CST #9856, Lot #7) Dilution: 1:800
Cycle 9	Ki-67 (CST #11882, Lot #4) Dilution: 1:400	cPARP (CST #6894, Lot #1) Dilution: 1:200	p65 NFkB (AB #AB190589, Lot #GR199457-1) Dilution: 1:800

1.3.4.1 CycIF image processing

Plates were imaged with 10x objective using a Cytell Cell Imaging System (GE). All raw images are available on HMS-LINCS webpage (http://lincs.hms.harvard.edu/). Image segmentation and analysis were performed using ImageJ. Hoechst images were converted to nuclear masks and ROIs. The same ROIs were applied to images for all data channels (488/555/647) and the fluorescent intensities were obtained. The nuclear masks were then converted into RING ROIs outside the nuclei and used to quantify channels of interest. The intensity data generated by ImageJ were then passed to MATLAB for further processing and analysis.

For sequential imaging of CycIF, image registration was accomplished using ImageJ software package scripts and the provided plugins (StackReg: http://bigwww.epfl.ch/thevenaz/stackreg/; MultiStackReg: http://bradbusse.net/downloads.html). Hoechst images from different cycles were inputted as reference images to generate registration information. The same registration information was used to transform images from other channels. The transformed images were compiled into multi-image stacks and the image segmentation and data retrieval were performed as described above. All ImageJ and MATLAB scripts are available on this website (http://lincs.hms.harvard.edu/lin-NatCommun-2015/).

1.3.4.2 CycIF data analysis

The viSNE and Wanderlust Matlab codes in the CYT package were obtained from the Pe'er lab webpage (http://www.c2b2.columbia.edu/danapeerlab/html/software.html). The raw data generated from CycIF was imported into FlowJo and converted to FCS files. FCS files were then used as input for both the viSNE and Wanderlust toolkits. All data files were aggregated and used to generate viSNE diagrams. For Wanderlust, the same FCS files were normalized using the Wanderlust script with default parameters (L number = 30; K number = 5; Number of landmarks = 20; Number of graphs = 25; Distance Metric = Cosine). Data from the DMSO-treated control sample were the starting point for the Wanderlust trajectory.

1.3.5 Analysis and statistics

1.3.5.1 Parameterization of dose-response curves

Variability in shape of dose-response curves can be quantified by performing a multiparametric analysis using a conventional logistical sigmoidal function

Equation 1

$$y = E_{inf} + \left(\frac{E_0 - E_{inf}}{1 + \left(\frac{D}{EC_{50}} \right)^{HS}} \right)$$

where y is a response measure at dose D (typically the experimental data), E_0 and E_{inf} are the top and bottom asymptotes of the response, EC_{50} is the concentration at half-maximal effect, and Hill slope *(HS)* is a slope parameter analogous to the Hill coefficient. Three values derived from equation 1 are in common use: IC_{50}, E_{max} and the area under the dose-response curve *(AUC)*. Although they are not strictly parameters of equation 1, we refer to IC_{50}, E_{max} and *AUC* as 'parameters' for simplicity. EC_{50} and IC_{50} are the classic measures of drug potency, and E_{max} and E_{inf} are measures of drug efficacy (for anticancer drugs, E_{max} varies between 1 at low doses and 0 at high doses, which corresponds to the maximum response of the cells). *AUC* combines potency and efficacy of a drug into a single parameter. *AUC* values can be compared for a single drug across multiple cell lines exposed to the same range of drug concentrations, but comparison of different drugs is problematic (because the scaling between drugs and dose ranges is generally arbitrary). In the simple case of second-order competitive inhibition, the case considered in most pharmacology textbooks, $E_0 = 1$, $E_{max} = E_{\mathrm{inf}} = 0$, $EC_{50} = IC_{50}$ and $HS = 1$ (Figure 2.7).

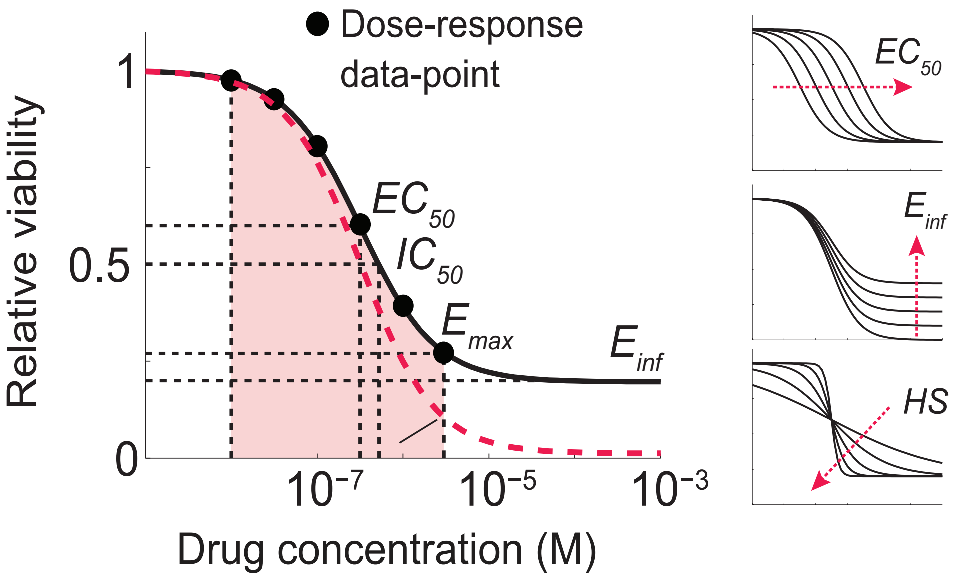

Figure 2.7 Parameterization of dose-response curves.

Schematic of key dose-response parameters (EC_{50}, IC_{50}, E_{inf}, E_{max} and AUC) calculated following curve fitting to the cell survival data. The pink area represents the AUC. The red dashed line represents the simple case of $E_0 = 1$, $E_{max} = E_{inf} = 0$, $EC_{50} = IC_{50}$ and HS = 1. Effects of variations in EC_{50}, hill slope (HS) and E_{inf} on the shape of dose-response curve are shown on the right. Details of parameters and logistic equation are described in the text (Fallahi-Sichani et al., 2013).

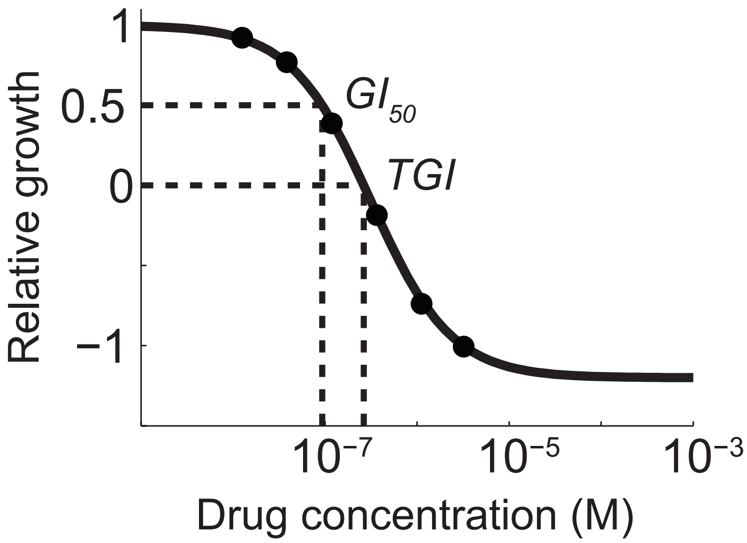

Figure 2.8 Growth inhibition curves.

Schematic of key dose-response parameters. Half-maximal growth inhibition (GI_{50}) and total growth inhibition (TGI) that can be calculated by fitting logistic curves to data on relative cell growth comprising a change in cell number after drug treatment normalized to the change in cell number in an untreated control well (Fallahi-Sichani et al., 2013).

1.3.5.2 Multiparametric analysis of dose-response curves

Methodologies for multiparametric analysis of dose response curves were adopted from previously published work (Fallahi-Sichani et al., 2013) that used previously published data comprising CellTiter-Glo measurement of per-well ATP concentrations (a metric of metabolically active cells) for 64 anti-cancer drugs and 53 well-characterized breast cell lines (Heiser et al., 2012). In this dataset, assays were performed before and 3 days after exposure to drugs at nine doses spanning a ~10^5-fold range (with maximum doses between 0.5 µM and 20 mM depending on potency. We computed viability as $y = N/N_C$, where the cell number N was measured in the presence of drug, and cell number N_C is measured in a no-drug control. As the number of cells present before the start of the experiment was available (N_0), we also computed $y^* = (N - N_0)/(N_C - N_0)$ to yield the GI_{50} value for $y^* = 0.5$. We confirmed key findings using independent dose-response data released through the Cancer Cell Line Project (for which estimates of N_0 are not available) (Barretina et al., 2012). Multiparametric analysis yielded values for EC_{50}, IC_{50}, GI_{50}, HS, E_{inf}, E_{max} and AUC for 2,789 drug–cell line combinations; data filtering described in the text and revealed substantial differences from one drug and cell line to the next (Figure 2.8).

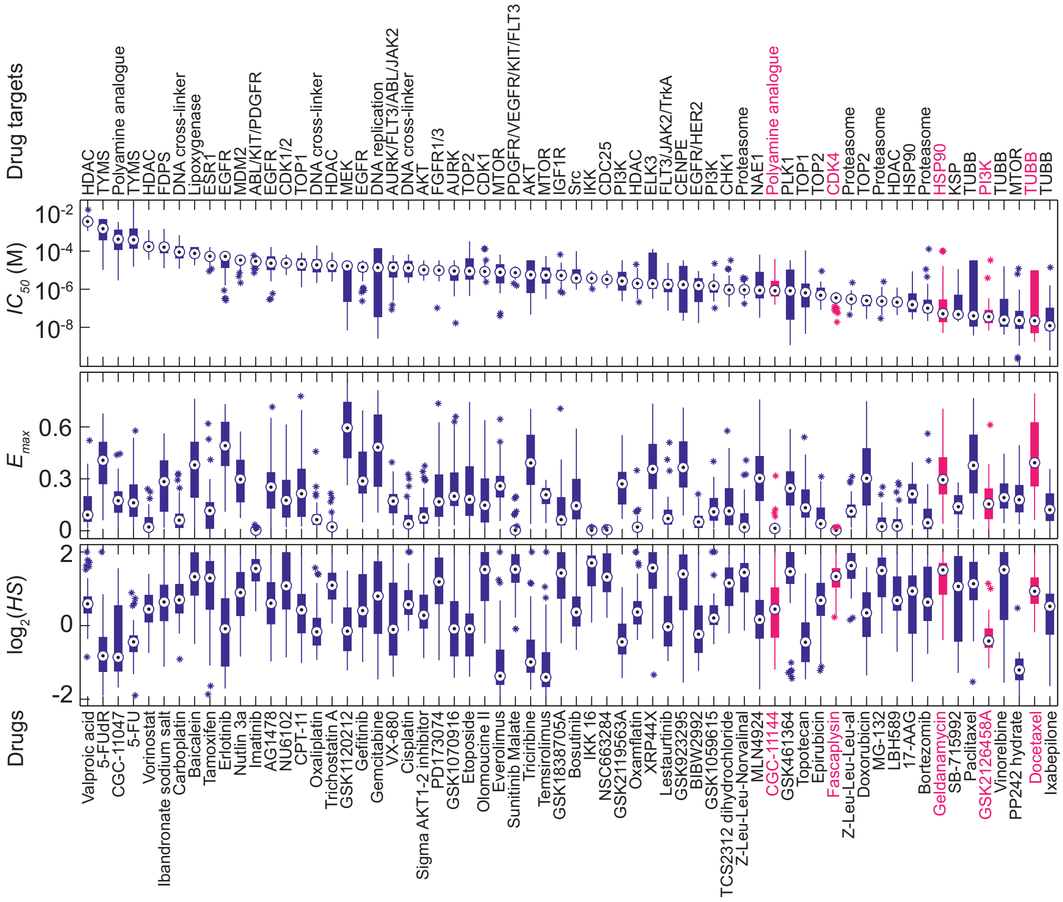

Figure 2.9 Parameters derived from drug response measured by relative ATP content.

The range of dose-response parameters, IC_{50} *(a measure of potency),* E_{max} *(a measure of efficacy) and HS (a measure of curve steepness) estimated for 64 compounds across 53 of the breast cell lines are represented by box-and-whisker plots and median parameter values and interquartile ranges; bars extending to 1.5x the interquartile range are shown for each drug as a measure of variance. Parameter values for outlier cell lines are marked with asterisks. Compounds are sorted on the basis of the median* IC_{50} *value. Drug targets are nominal and do not include off-target effects (Fallahi-Sichani et al., 2013).*

1.3.5.3 Principal component analysis (PCA)

Principal component analysis (PCA) is a dimensionality reduction method that rotates the high-dimensional data set, seeking to capture most variance in a small number of successively chosen orthogonal axes of measurement combinations. PCA can be thought of as fitting a quadratic surface with *n* dimensions to the data, where each axis of the surface represents a principal component. To find these axes, the averaged data points must be subtracted from the origin in order to zero-center the data points. Then, a covariance matrix of the data points needs to be computed so that the eigenvalues with their corresponding eigenvectors could be calculated.

The principal components are defined by weighting signals with high covariance and de-emphasizing signals that show little covariation with other signals. In this way, PCA condenses measurements to highlight the global patterns in the data set as reflected by just two or three dimensions that capture the maximal covariation between all of the signals (Janes and Yaffe, 2006; Wikipedia, 2015).

1.3.5.4 *K*-means clustering

Clustering is a simple data-mining tool for analyzing large-scale datasets. Many clustering methods are based on global optimization of a criterion that measures compatibility of the clustering result to the data. *K*-means and mixture Gaussian model-based clustering are examples of this category (Tseng, 2007). *K*-means clustering is an unsupervised learning algorithm that solves the well-known clustering problem. This statistical clustering method that partitions *n* data points into *k* clusters in a way that each observation will belong to the cluster with the closest mean. To start the clustering, *k* center-points need to be defined for each cluster. These center-points are placed as far as possible in respect to each other. Then, data points from each cluster are assigned to nearest center-points until there are no data points left. Afterwards, new center-points are calculated which might lead to a change in their location and the process is repeated until the cluster centroids do not reposition anymore. Therefore, the drawback of this method is that it heavily dependens on the prior selection of the center-points (Abdul Nazeer and Sebastian, 2010).

1.3.5.5 viSNE (Stochastic Neighboring Embedding)

Reducing the dimensionality of data involving heterogeneous cell populations can be accomplished using t-distributed stochastic neighbor embedding (t-SNE) (Maaten and Hinton, 2008) which projects cell populations in a two-dimensional space while attempting to preserve local neighbor relationships. SNE methods accomplish this by distributing data points so that distributions of pairwise similarity scores for each point to all others are minimally divergent between the original and the projected data (Hinton and Roweis, 2002). To obtain a flat projection that better retains the heterogeneity of cells than the projection of *k*-means clusters, t-SNE implementation viSNE could be used as an alternative approach motivated for the analysis of CyTOF data (Amir el et al., 2013).

1.3.5.6 Wanderlust

Because cells in normally growing populations of cells are present at different points in the cell cycle, it is possible to reconstruct cell cycle trajectories from certain kinds of fixed cell data (Kafri et al., 2013). A widely used method to this end is the Wanderlust algorithm (Bendall et al., 2014), which connects paths of nearest neighbors among subsampled single-cell readouts in order to place cells on a shared axis that may correspond to progression through a differentiation program or the cell cycle (Gut et al., 2015).

3. RESULTS

1.4 Dissecting population averaged drug response

1.4.1 Results from high-content immunofluorescence (IF) imaging and biochemical methods

1.4.1.1 Multiparametric analysis of dose-response curves

We derived different dose-response parameters from each individual curve, including GI_{50}, AUC, Hill slope (HS), and E_{max}. Instead of reporting a single parameter as a measure of potency or efficacy, we plotted pairwise combinations against each other while surmising dependencies between some parameters and target identity. Overall, MEK inhibitors (PD0325901 and Selumetinib) were most potent in inhibiting growth, followed by mTOR (Dactolisib and PP242) and EGFR (Gefitinib and Erlotinib) inhibitors, and AKT targeting drugs (MK2206 and Triciribine) were least potent (Figure 3.1). This ranking of target classes by potency was largely consistent between AUC and GI_{50}.

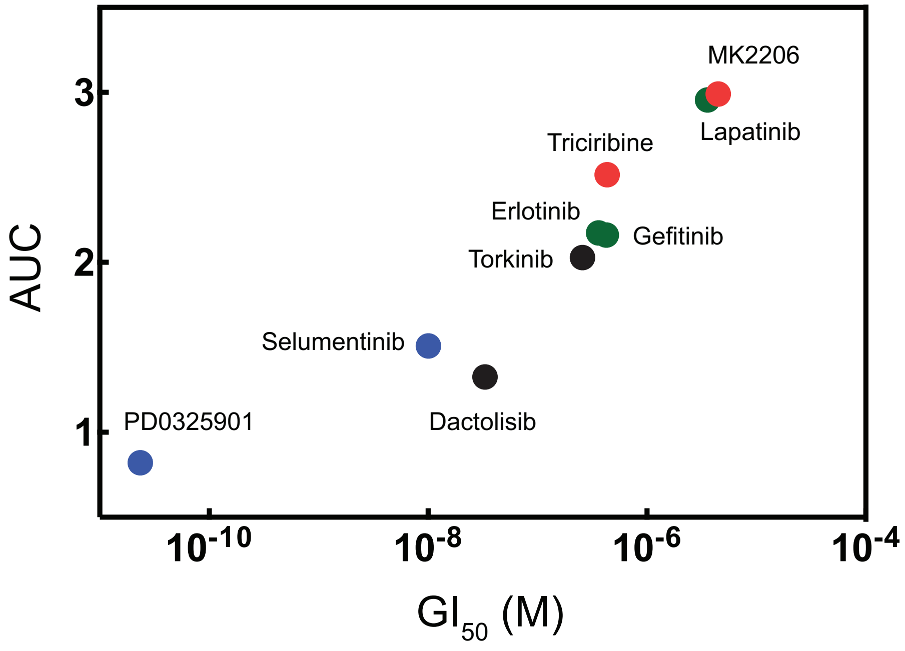

Figure 3.1 Measurement of drug potency by pairwise combinations of two parameters.

Rank orders of most potent to least potent inhibitors of growth in MCF10a cell line. MEK inhibitors (PD0325901 and Selumetinib in blue), mTOR inhibitors (Dactolisib and PP242 in black), EGFR inhibitors (Gefitinib, Erlotinib and Lapatinib in green) and AKT inhibitors (Triciribine and MK2206 in red).

When maximal effect (E_{max}) was plotted against *HS*, drugs sharing a nominal target always cluster together. Among those clusters, EGFR targeting drugs implicate a much steeper *HS* than all other target classes. Furthermore, all drugs other than the AKT-targeting ones have very similar maximal cytostatic effects (E_{max}) (Figure 3.2).

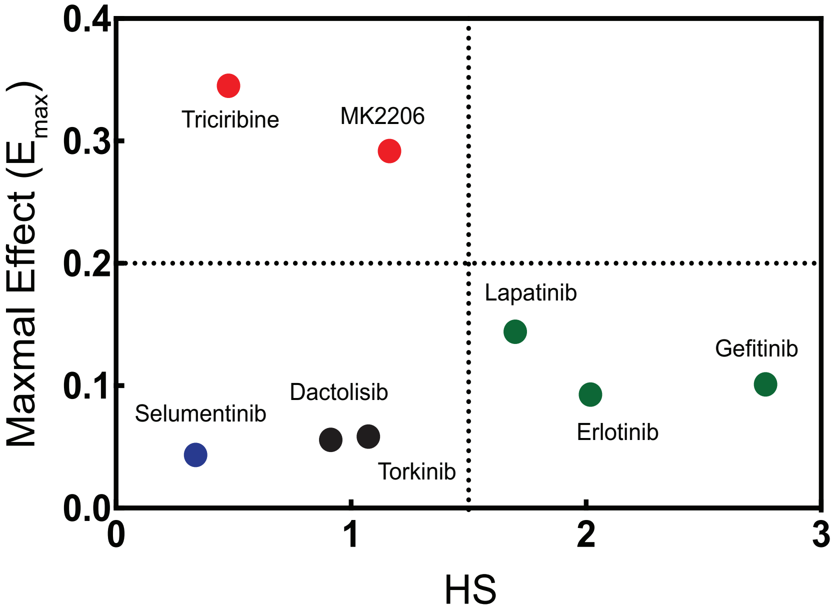

Figure 3.2 Measurement of drug efficacy and hill slope reveals clusters based on drug target.

All tested drugs with different targets (EGFR, MEK and mTOR) are effective in inhibiting growth at highest tested dose with E_{max} *~0.1, beside AKT inhibitors with* E_{max} *~0.35. EGFR targeting drugs (Erlotinib, Gefitinib and Lapatinib) have much steeper hill slope (HS>1.5) compared to MEK-, AKT- and mTOR targeting drugs.*

1.4.1.2 Averaged signal-response parameters

To explore differences in the signaling response between drugs, we averaged signals such as p-ERK1/2, p-S6, and p-4EBP1, which had shifting but always unimodal distributions across cells. We confirmed that MEK and EGFR drugs inhibited ERK signaling, but unexpectedly, AKT/mTOR drugs, in particular Torkinib, increased the phosphorylation of ERK1/2 in a dose-dependent manner. This suggests a feedback mechanism whereby mTOR activity negatively regulates ERK activation. Besides AKT inhibitors, which had no effect, and MEK inhibitors, which were minimally effective, other drugs fully suppressed S6 phosphorylation, and only mTOR-targeting drugs fully suppressed 4E-BP phosphorylation (Figure 3.3).

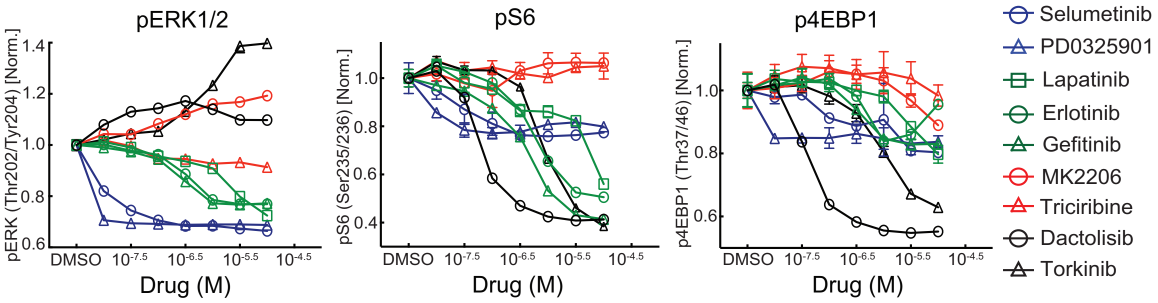

Figure 3.3 Averaged signal analysis reveals significant molecular complexity underlying phenotypic differences.

Dactolisib was very potent against p-S6 and p-4E-PB1, two proteins involved in translational control, whereas Selumetinib, which is even more potent as an inhibitor of cell growth, had little effect. In the case of the mTOR inhibitor (Torkinib), dose-dependent increase in p-ERK1/2 is evident.

1.4.1.3 Dynamics of MAP kinase signaling in response to EGFR inhibitors

In order to probe how dynamics of MAPK signaling relates to response to EGFR/ERBB2 inhibition, we treated a panel of 11 cell lines (four human mammary epithelial cells, four HER2 positive breast cancer cells and three lung cancer cell lines) with increasing dose of Lapatinib (9 doses and DMSO) and measured the phosphorylated levels of ERK1/2 after 1 hour and 6 hours and plotted the IC_{50} of p-ERK1/2 signal response curves at 1 hour in blue, 6 hour in green and the IC_{50} of the growth inhibition curve after 72 hours in red (Figure 3.4).

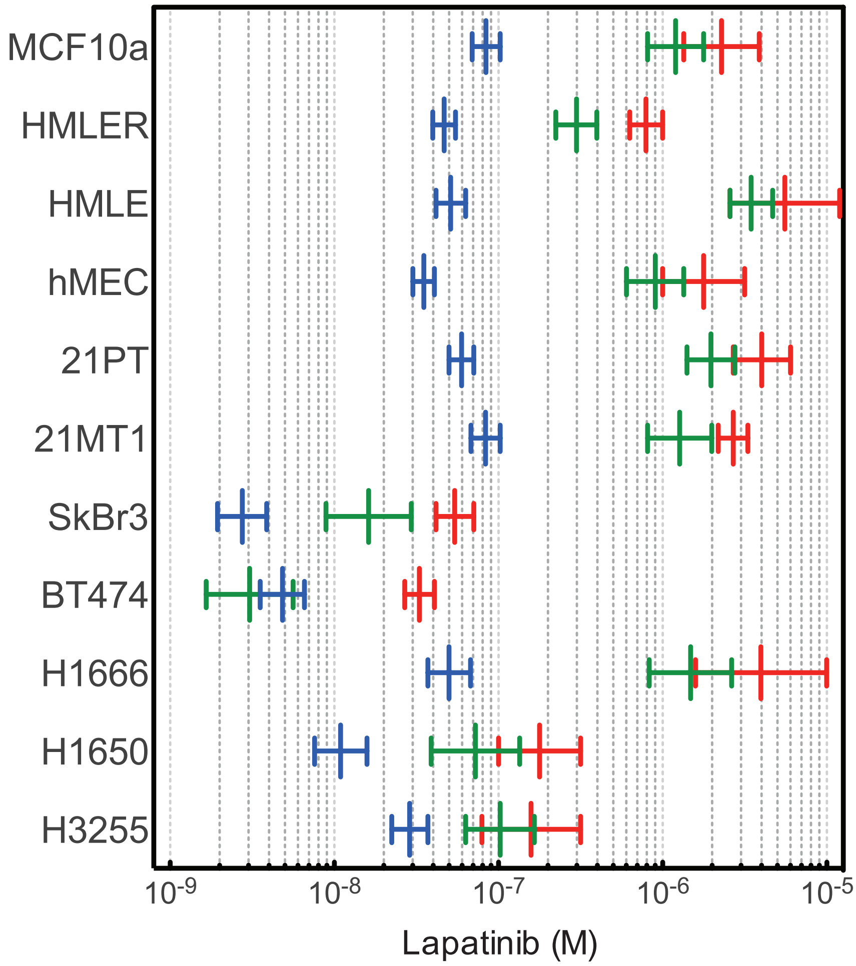

Figure 3.4 MAPK dynamics in response to EGFR/HER2 inhibiting by lapatinib.

Averaged p-ERK1/2 IC_{50} curves after 1 hour (blue) and 6 hours (green) and averaged GI_{50} curves after 72 hours (red) in 3 immortalized human mammary epithelial cells (MCF10a, HMLER, HMLE and hMEC), 4 HER2 positive breast cancer cells (21MT1, 21PT, SkBr3 and BT474) and 3 non-small cell lung cancer cell lines (H1666, H1650 and H3255). SkBr3, BT474, H1650 and H3255 are sensitive and the rest of the cell lines are resistant to lapatinib measured by the GI_{50}.

As it can be seen in Figure 3.4, in sensitive cell lines, where the GI_{50} concentration is about 100 nM, the p-ERK1/2 IC_{50} does not change much over time. However in resistant cell lines, the IC_{50} of p-ERK1/2 signal response curve is about 100 nM at 1 hour but it recovers after 6 hours of drug treatment. Moreover, the IC_{50} of p-ERK1/2 at 6 hours has a value similar to the IC_{50} of the growth inhibition curve at 72 hours.

To examine the degree of correlation between early (1 hour) and intermediate (6 hours) p-ERK1/2 response and the late phenotypic response GI_{50}, we calculated the linear correlation between these data points for all the cell lines. As it can be seen in Figure 3.5, there is a good linear relationship (R^2=0.80) between the early signal and late phenotype and this correlation improves (R^2=0.96) with time.

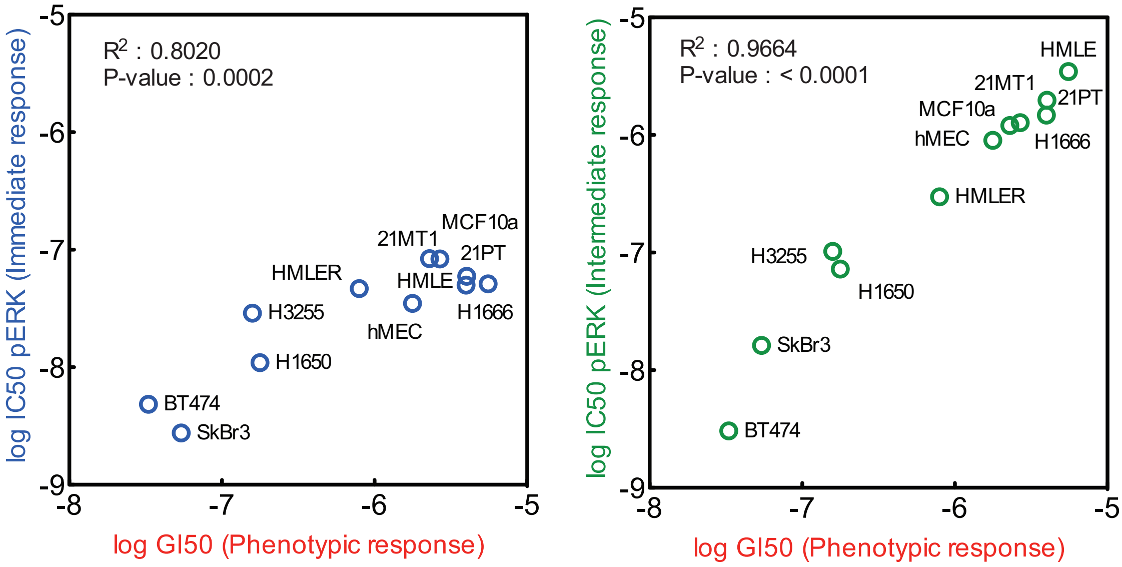

Figure 3.5 Linear correlation between dynamics of p-ERK1/2 and growth inhibition.

The x-axis shows the phenotypic response curves measured by GI_{50} *and y-axis the* IC_{50} *of p-ERK1/2 signal response curves for all the cell lines. The left panel shows the correlation of the phenotype with p-ERK1/2 at 1 hour and the right panel shows the correlation between p-ERK1/2 and phenotype after 6 hours of drug exposure.*

This result shows the importance of MAPK signaling and its dynamics in response to EGFR/HER2 targeted inhibition. Among many possible mechanisms that could explain the transient inactivation of MAPK signaling in response to EGFR/HER2 therapies, drug metabolization (Duckett and Cameron, 2010), efflux by ABC transporters (Sharom, 2008) and activation of autocrine loops (Gazdar and Minna, 2008) have been described extensively in the literature. To investigate whether the drug is still active post treatment, we treated MCF10a cells with increasing dose of Lapatinib for 5 hours and took the conditioned media and drug that have been on cells during this time and put it on fresh cells that had no memory of drug treatment and measured p-ERK1/2 activity after 1 hour. Interestingly, the 1 hour signal response curve of the drug that had been on cells in total for 6 hours was very similar to the signal response curve of the drug that was only on cells for 1 hour. In addition, we performed a reverse experiment where we took the cells that have been in the presence of drug for 5 hours and put fresh media and drug on them for 1 hour. The resulting signal response curve was very similar to cells that have been in the presence of the drug for 6 hours (Figure 3.6).

This result not only shows that the drug is not degraded and remains fully active after 6 hours but also indicates that the recovery is an induced state of cells, as cells that had the memory of being in the presence of drug remained resistant to p-ERK1/2 inhibition when exposed to fresh drug.

Another possible mechanism for the recovery is activation of an autocrine loop or drug efflux that may potentially lead to reactivation of the drug target, the former by more extracellular EGF and thereby receptor activation and the latter by reducing the intracellular drug concentrations. To investigate this, we pretreated cells with Batimastat an inhibitor of ligand shedding and then treated cells with Cetuximab and EGFR neutralization antibody that competes with EGFR specific ligands. Surprisingly, the same behavior of p-ERK1/2 signaling was observed with Cetuximab in the absence or presence of Batimastat, providing evidence that EGFR autocrine loop is not the cause of recovery (Figure 3.7).

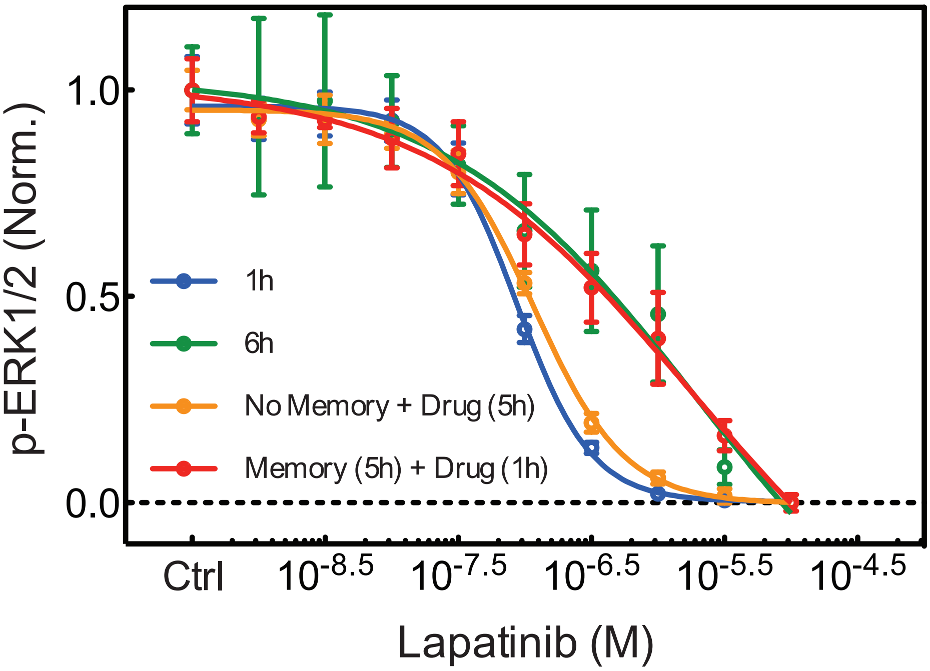

Figure 3.6 p-ERK1/2 recovery is an induced state.

Averaged p-ERK1/2 signal responses to Lapatinib were assessed in 4 different conditions. p-ERK1/2 signal response after 1 hour (blue) treatment with fresh Lapatinib, after 6 hours (green) of treatment with fresh Lapatinib, after 1 hour of treatment with Lapatinib that was exposed to cells for 5 hours (yellow) and after 1 hours of treatment with fresh Lapatinib on cells pretreated with the drug for 5 hours (red).

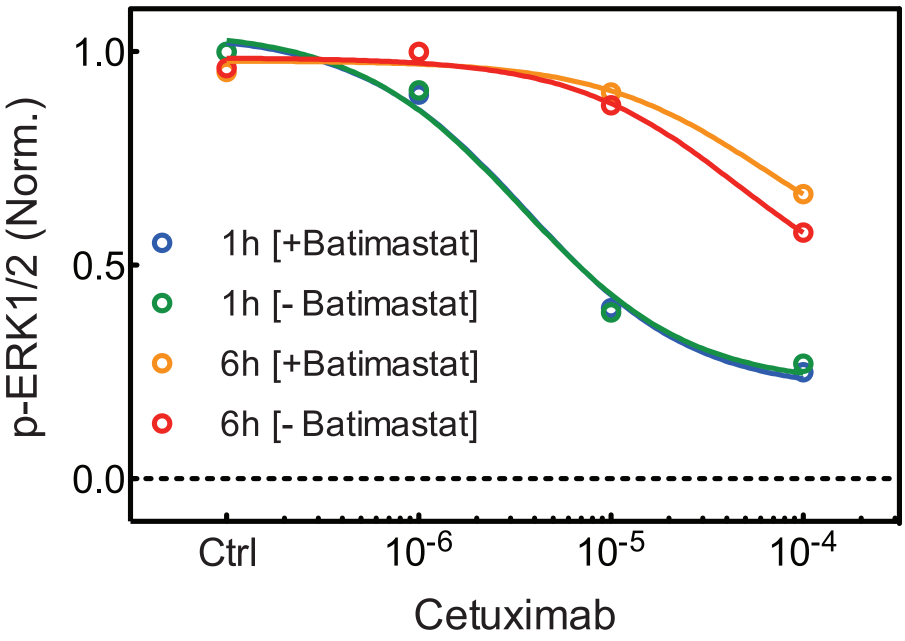

Figure 3.7 p-ERK1/2 recovery is not regulated by an autocrine loop activation.

Averaged p-ERK1/2 signal response to Cetuximab (Erbitux) in the presence or absence of Batimastat a ligand shedding inhibitor. p-ERK1/2 signal response curve after 1 hour of exposure to Erbitux in the presence of Batimastat (blue), after 1 hour of exposure to Erbitux in the absence of Batimastat (green), after 6 hour of exposure to Erbitux in presence of Batimastat (yellow) and after 6 hour of exposure to Erbitux in the absence of Batimastat (red).

Furthermore, Cetuximab cannot be a substrate for an ABC transporter and the evidence in the literature (Dai et al., 2008) shows that Lapatinib is rather an inhibitor of ABCG2 drug pumps. However, observing similar results from small-molecule and antibody inhibition pointed us to the drug target itself.

1.4.1.4 Dynamics of drug target inhibition

To quantify the activity of EGFR/HER2, we performed quantitative ELISA on a subset of cell lines treated with 1 μM Lapatinib. Figure 3.8 shows that after 1 hour with Lapatinib, p-EGFR and p-HER2 are fully inhibited in all cell lines. However, after 6 hours, both drug targets get reactivated in resistant cell lines, while they remain inactive in sensitive cell lines.

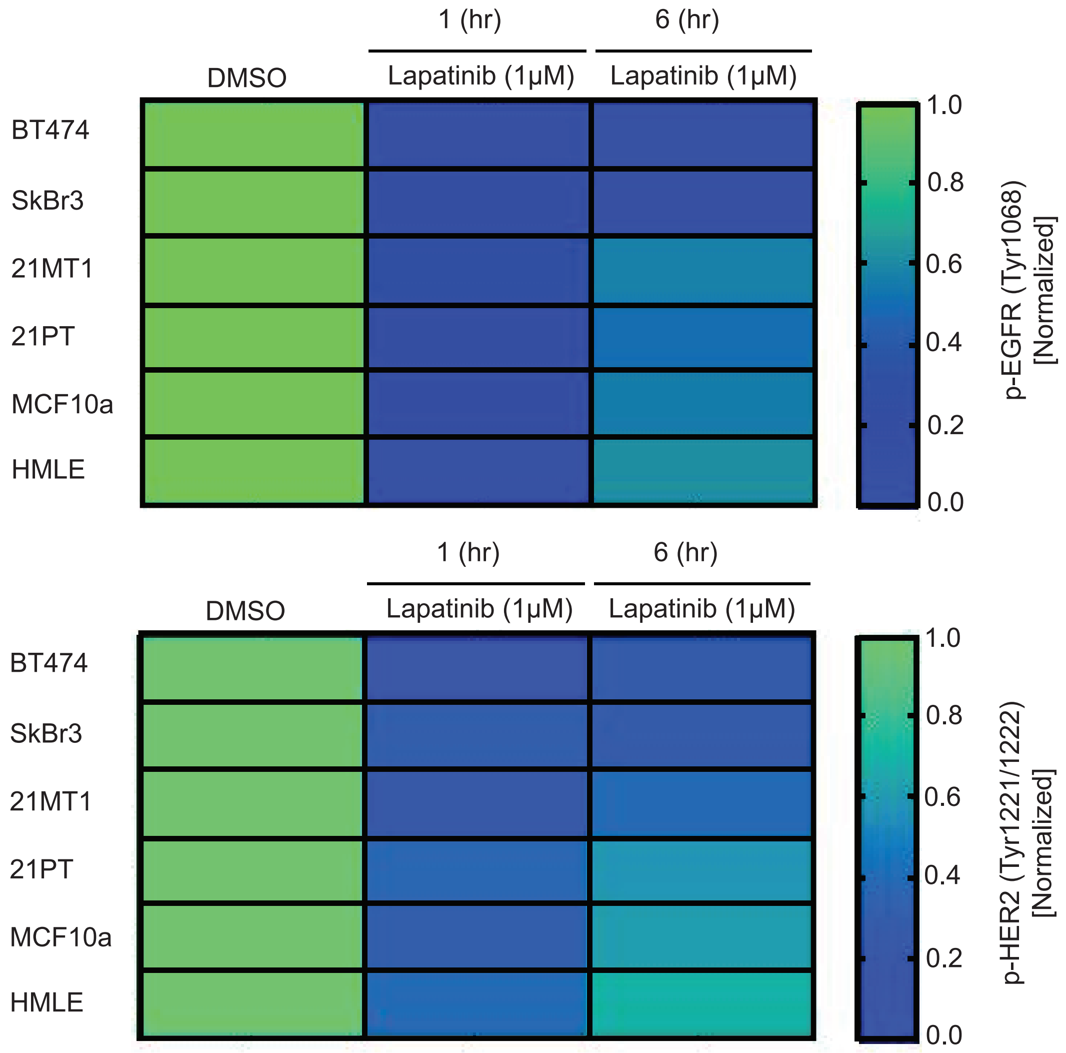

Figure 3.8 Recovery of MAP kinase signaling is regulated at the receptor level.

Phosphorylated levels of EGFR and HER2; Lapatinib targets were quantified by ELISA. Both phosphorylated forms of EGFR and HER2 are inhibited after 1 hour of exposure to Lapatinib, however both targets recover only in resistant cell lines. Top panel shows phosphorylated EGFR at Tyr1068 residue and the bottom panel shows phosphorylated levels of HER2 at Tyr1221/1222 residues.

To investigate the origin of this recovery we used high-content imaging and western blot analysis to have a relative view on the localization and activity of the receptor (EGFR).

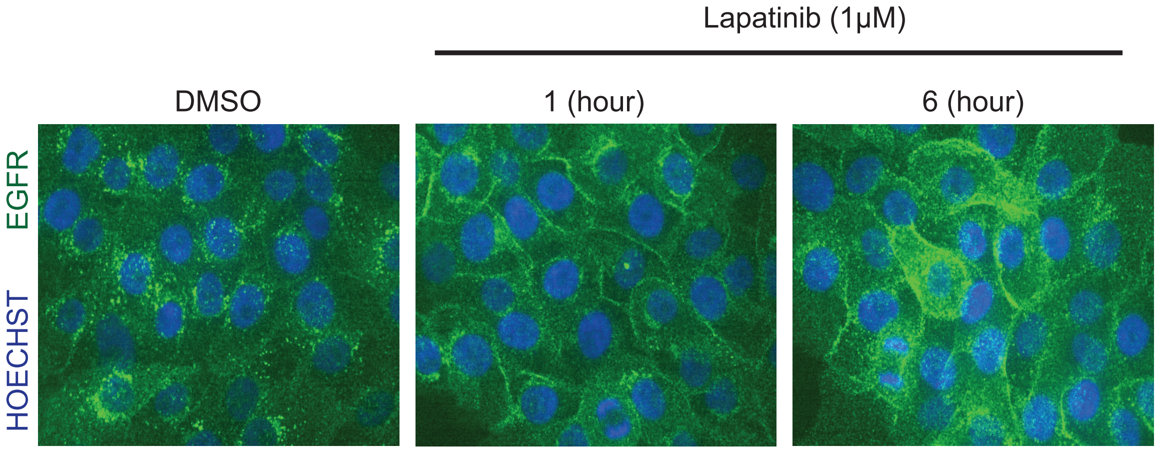

Figure 3.9 Total EGFR localizations in response to lapatinib in full serum. *EGFR localization in full serum media after 1 or 6 hours treatment with DMSO or 1 μM lapatinib.*

As it can be seen in Figure 3.9, EGFR in cells cultured in full serum media seem to be internalized, detected as punctuates inside the cell. However, 1 hour post Lapatinib treatment, the EGFR punctuates quantified as spots seem to diffuse rapidly accompanied by reduction of clathrin heavy chain spots with a very similar rate (Figure 3.10). The rate seems to decline between 1 hour and 6 hours in a way that the ratio of total levels and membrane levels of EGFR remain constant but both increase during these time points. The phosphorylation of the receptor at two different sites and its direct downstream binding protein Shc seems to follow the same trend which is inhibition at 1 hour accompanied by subsequent recovery and reactivation later on.

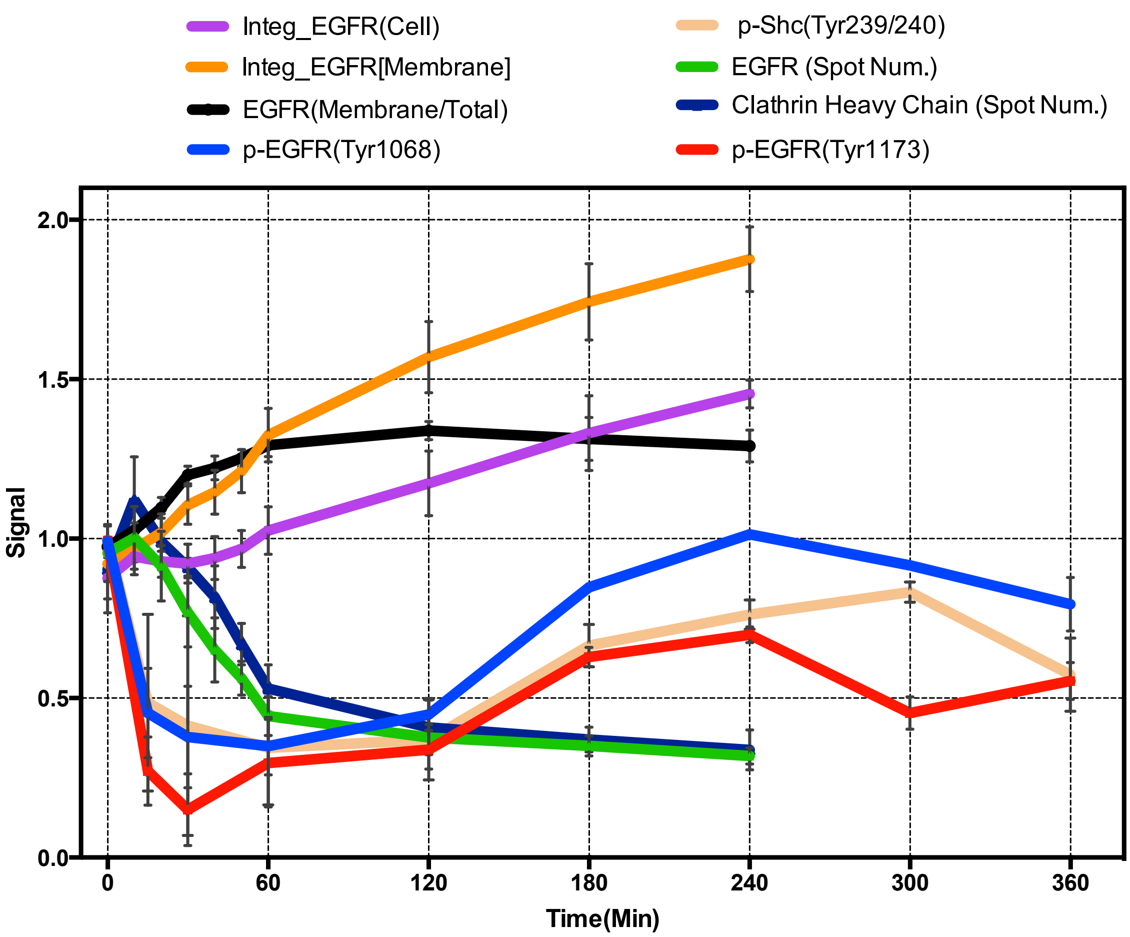

Figure 3.10 Recovery of EGFR phosphorylation is accompanied by EGFR translocation to plasma membrane.

Phosphorylated levels of EGFR at Tyr1068 and Tyr1173 residues get inhibited after 1 hour of drug exposure. This reduction is associated with a sharp decline in the number of EGFR and clathrin heavy chain punctuates as well as increased levels of EGFR localization at the cell membrane. The number of EGFR and clathrin heavy chain spots flat out after 1 hour, while the membrane levels of EGFR continue to rise during the process of p-EGFR recovery.

1.4.1.5 Drug combination to overcome recovery

We argue that localization of the receptor at cell membrane facilitates ligand binding and thereby causes activation of the reserved receptor that was internalized prior to drug treatment.

Due to post-treatment recovery of the drug target itself, we examined combined treatment of Lapatinib with Erlotinib, another EGFR inhibitor. In other words, we hypothesized that inhibiting the activity of the same target with multiple drugs would likely lead to sustained inhibition (Figure 3.11).

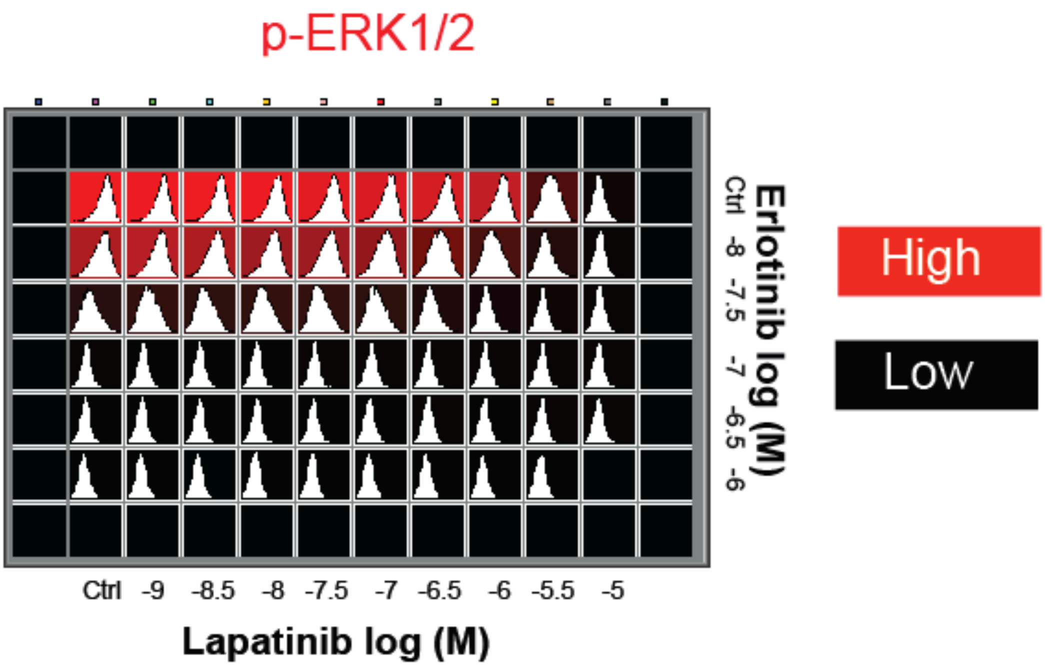

Figure 3.11 Sustained inhibition of p-ERK1/2 by drug combination.

On the x-axis increasing doses of Lapatinib was combined with increasing doses of Erlotinib on the y-axis of a 96-well plate and p-ERK1/2 was measured. Single-cell frequency plots for cells in each well show how the population behaves across dose combinations. Red color indicates high levels and black indicates low levels of p-ERK1/2.

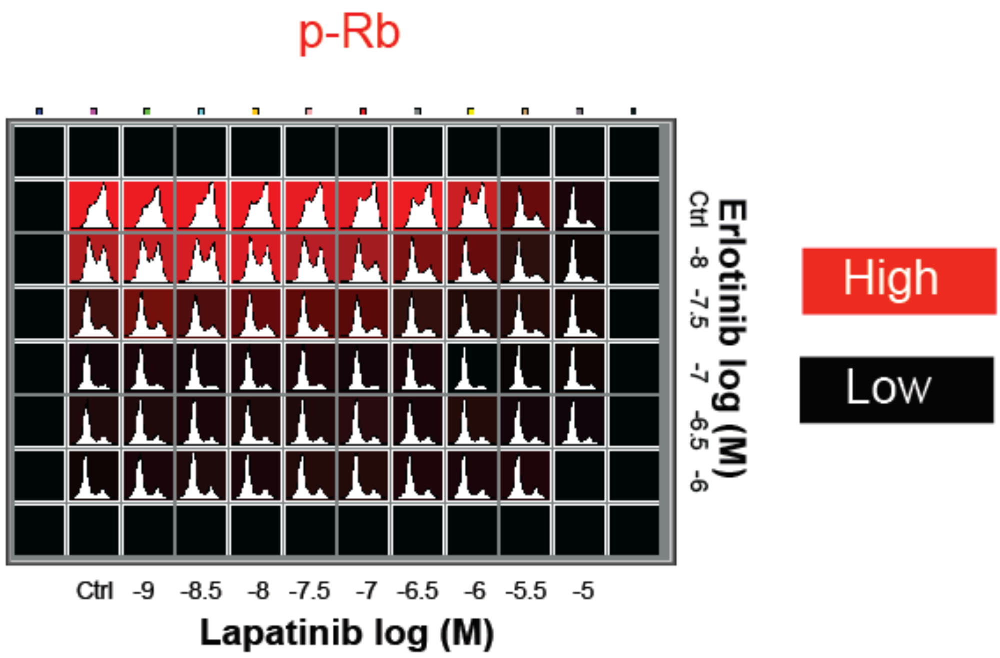

Figure 3.12 Combination of EGFR targeting drugs leads to sustained inhibition of proliferation signaling.

On the x-axis increasing doses of lapatinib was combined with increasing doses of Erlotinib on the y-axis of a 96-well plate and p-Rb was measured. Single-cell frequency plots for cells in each well show how the population behaves across dose combinations. Red color indicates high levels and black indicates low levels of p-Rb.

As it can be seen in Figures 3.11 and 3.12 at the level of p-ERK1/2 and p-RB, Lapatinib combined with Erlotinib leads to a synergistic effect resulting in a full and sustained inhibition of these signals compared to Lapatinib alone after 24 hours of drug treatment.

1.4.1.6 Principal component analysis of drug response data

To explore the space of signaling changes in response to all drugs along all measured signaling markers, we performed principal component analysis (PCA) over all drug treated conditions after normalizing bulk signals against

DMSO-treated samples and converting into log ratios. PCA rotates the high-dimensional data set, seeking to capture most variance in a small number of successively chosen orthogonal axes of stain combinations. We found that two such principal component axes alone were sufficient to capture 88% of all variance, indicating that the bulk signaling changes in response to each of the tested drugs collectively occurred in a flat plane (Figure 3.13). Increasing doses of kinase inhibitors perturbed the bulk signaling state of cells in a characteristic direction for each target class. While all MEK, EGFR, and mTOR inhibitors reduced signals along the first component, which was largely a projection of p-CDK2, differences in the effects between target classes lied mostly in ERK activation and p-S6. p-ERK1/2 was the largest negative loading of the second principal component, and suppression of p-S6 and p-4E-BP were strongly positive loadings of both. This largely reflects induction of p-ERK1/2 by mTOR inhibitors and a declining effect of drugs on p-S6 and p-4E-BP from mTOR inhibitors, which were strong suppressors, over EGFR inhibitors to MEK inhibitors, which had no effect. The signaling axis along the cell growth markers p-S6 and p-4E-BP was virtually orthogonal to that of the cell cycle progression markers p-CDK2 (see compass inset) and p-Rb.

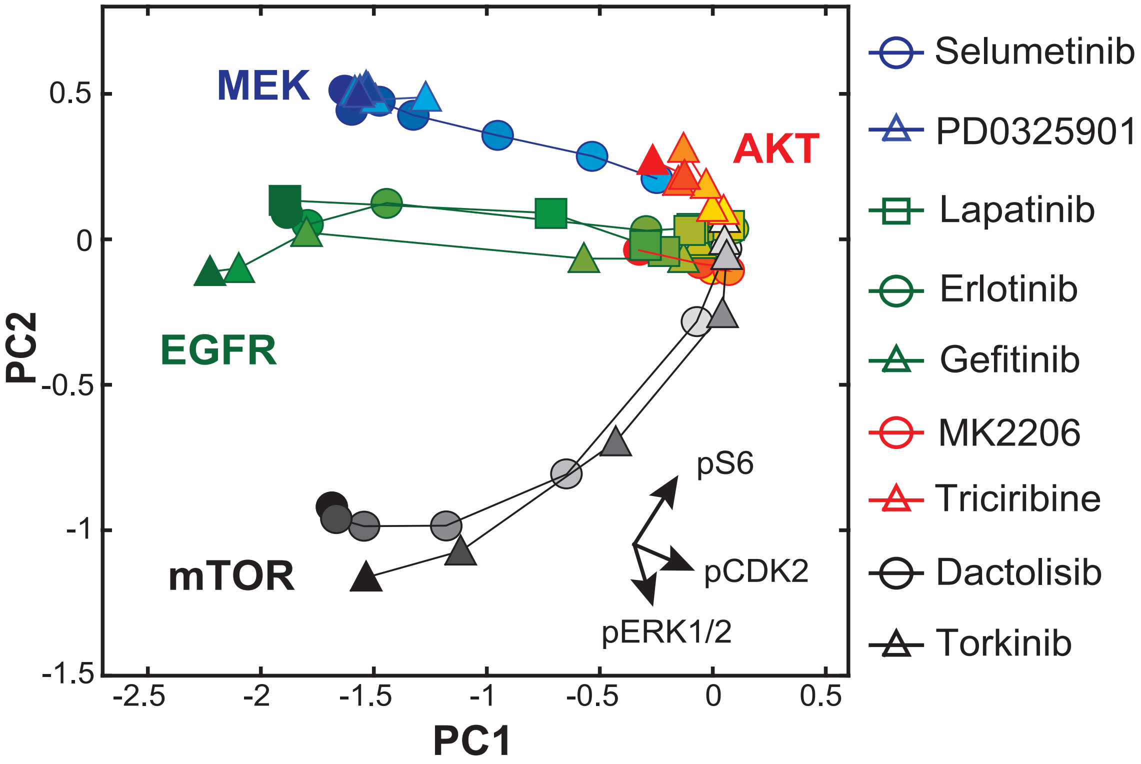

Figure 3.13 Principal component analysis (PCA) of drug effects clusters inhibitors that have similar nominal targets.
PCA analysis of MEK inhibitors (PD0325901 and Selumetinib), EGFR inhibitors (Erlotinib, Gefitinib and Lapatinib) AKT inhibitors (Triciribine and MK2206) and mTOR inhibitors (Dactolisib and Torkinib).

To challenge this interpretation with an alternative analysis, we normalized the log ratios by the standard deviation of each signal in freely cycling cells. Intuitively, this normalization emphasizes drug-induced changes in signaling markers that are otherwise more tightly regulated. The corresponding PCA therefore yielded different loadings, with the direct CDK2 inhibitory protein p27 as the main loading of the first principal component, and p-AKT and p-4E-BP as the main loadings of the second (Figure 3.13). The projection of drug effects along the p27/Kip1 axis was oriented in opposite direction to the p-CDK2 axis in Figure 3.12, consistent with mutually antagonistic interactions between CDK2 and p27/Kip1. While the protein synthesis marker p-4E-BP was shared between the second principal components of both analyses, the mTOR regulator AKT and the mTOR substrate p-S6 were concordant readouts of growth regulation as well. This confirms that the bulk signaling changes in response to treatment with drugs from the kinase inhibitor panel largely occur within a plane spanned by growth and cell cycle progression axes.

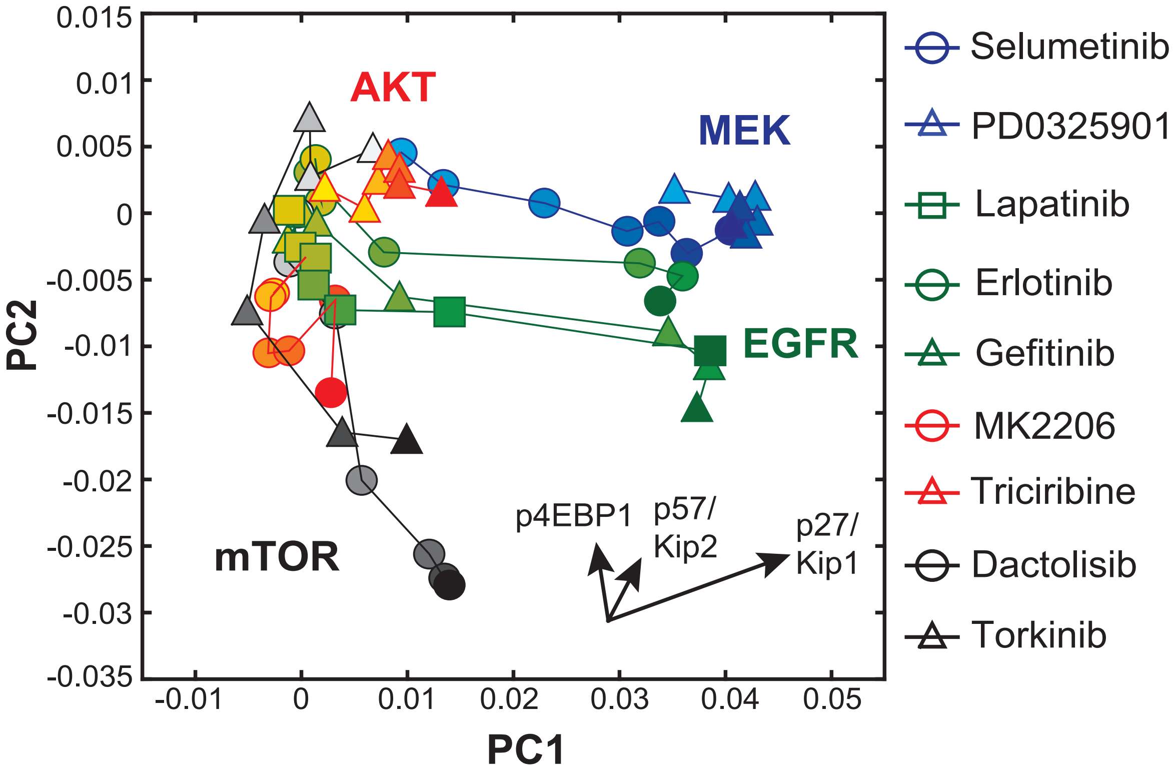

Figure 3.14 Principal component analysis (PCA) of drug effects clusters inhibitors that have similar nominal targets.

PCA analysis of MEK inhibitors (PD0325901 and Selumetinib), EGFR inhibitors (Erlotinib, Gefitinib and Lapatinib) AKT inhibitors (Triciribine and MK2206) and mTOR inhibitors (Dactolisib and Torkinib). PC1 and PC2 in this PCA model are indicated with an apostrophe in the text.

1.5 Dissecting single-cell level variability in drug response

1.5.1 Results from high-content immunofluorescence (IF) imaging

1.5.1.1 Fractional analysis of signal-response curves

To test the predictive value of some of the strongest loadings of the PCA model, we first integrated those signals over all doses by computing the *AUCs* of the p-ERK1/2, p-S6, and p-CDK2 mean signals. Because some of these signals where highly variable from cell to cell (Figure 3.15), we also calculated the *AUCs* of the fractions of cells that either p-CDK2 positive or were p-CDK2/p-Rb double positive after treatment with drugs for 24 hours.

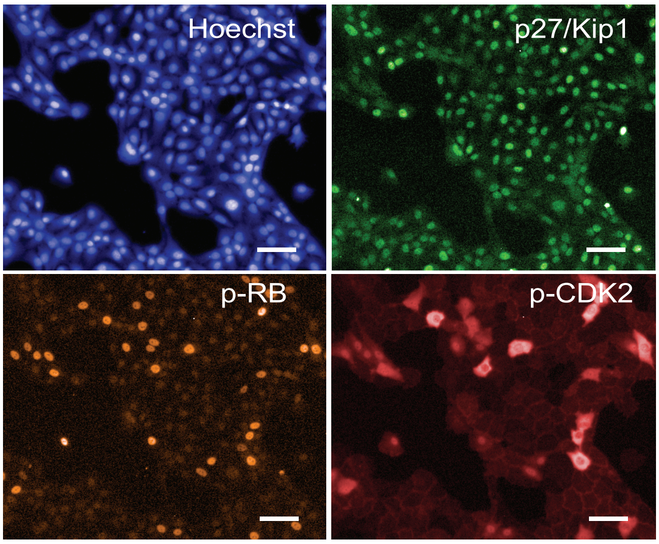

Figure 3.15 Representative images of graded and on or off signals.
Representative images of population of cells stained with Hoechst dye and Whole Cell Blue to label nuclei and cytoplasm (blue) as well as stained with primary mouse p27/Kip1 antibody (green), goat p-Rb antibody (orange) and rabbit p-CDK2 antibody (red) together with respective species-specific secondary antibodies. p27/Kip1 has a graded distribution across single cells compared to p-Rb that is either on or off and p-CDK2 signal that is either on or off and either cytoplasmic or nuclear. Bars correspond to ~10 µm.

We then assessed the correlation of these metrics with the *AUC* of growth inhibition after 48 hours (Figure 3.16). We found no significant correlation between the phenotypic response (*AUC* of GI_{50} after 48 hours) and the *AUC* of upstream signaling nodes such as p-ERK or p-S6. However, p-CDK2, a downstream cell cycle regulator showed a much better linear relationship with the 48-hour phenotype. This correlation significantly improved when the fraction of p-CDK2 positive cells was used instead of the mean p-CDK2 signal. Notably, the fraction of p-CDK2/p-Rb double positive cells did not improve predictions beyond using p-CDK2 alone, thus emphasizing the crucial role of CDK2 in controlling drug response upstream of p-Rb in MCF10A cells. More generally, the results show that an analysis based on fractions of positive or negative cells can be more informative of drug response signaling than simply using population averages.

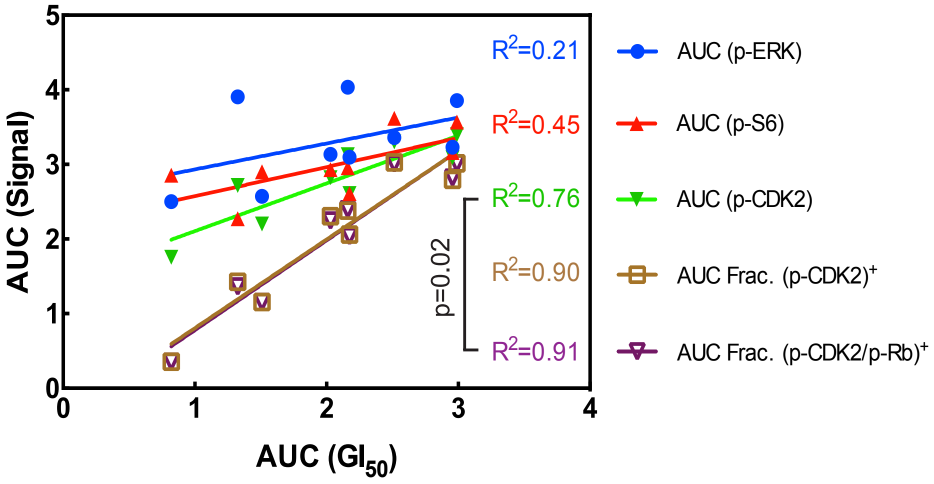

Figure 3.16 Single-cell fractions better predict growth inhibition phenotype. *The linear correlation between AUC of signal response curves of phospho-specific measured markers (strongest loadings of PCA model) (p-ERK1/2, p-S6, p-CDK2 as well as positive p-CDK2 fraction and p-CDK2 and p-Rb double positive fraction) after 24 hours and the AUC of growth inhibition curve after 48 hours. Statstical significance was assessed by Fisher's r-to-z transformation.*

1.5.1.2 Single-cell visualization of cytostatic states

To assess the role of the strongest loadings in the second PCA model (Figure 3.14), we plotted the single-cell drug responses of Cyclin-dependent kinase inhibitors (CDKIs) p21/Cip1, p27/Kip1, and p57/Kip2 against p-RB for the maximal tested drug dose (10 µM, Figure 3.17). We found that EGFR- and MEK-targeting drugs caused an accumulation of these CDKIs, whereas mTOR drugs not only failed to increase p27/Kip1 and p57/Kip2 levels, they even led to a reduction in p21/Cip1. This was similar for AKT inhibitors, which we showed not to be effective in inhibiting growth. These results illustrate the value of high-content imaging compared to methods that measure viability or surrogates such as ATP concentrations, while EGFR-, MEK- and mTOR-targeting drugs shared similar E_{max}, yet our high-content molecular analysis revealed quite different cytostatic states.

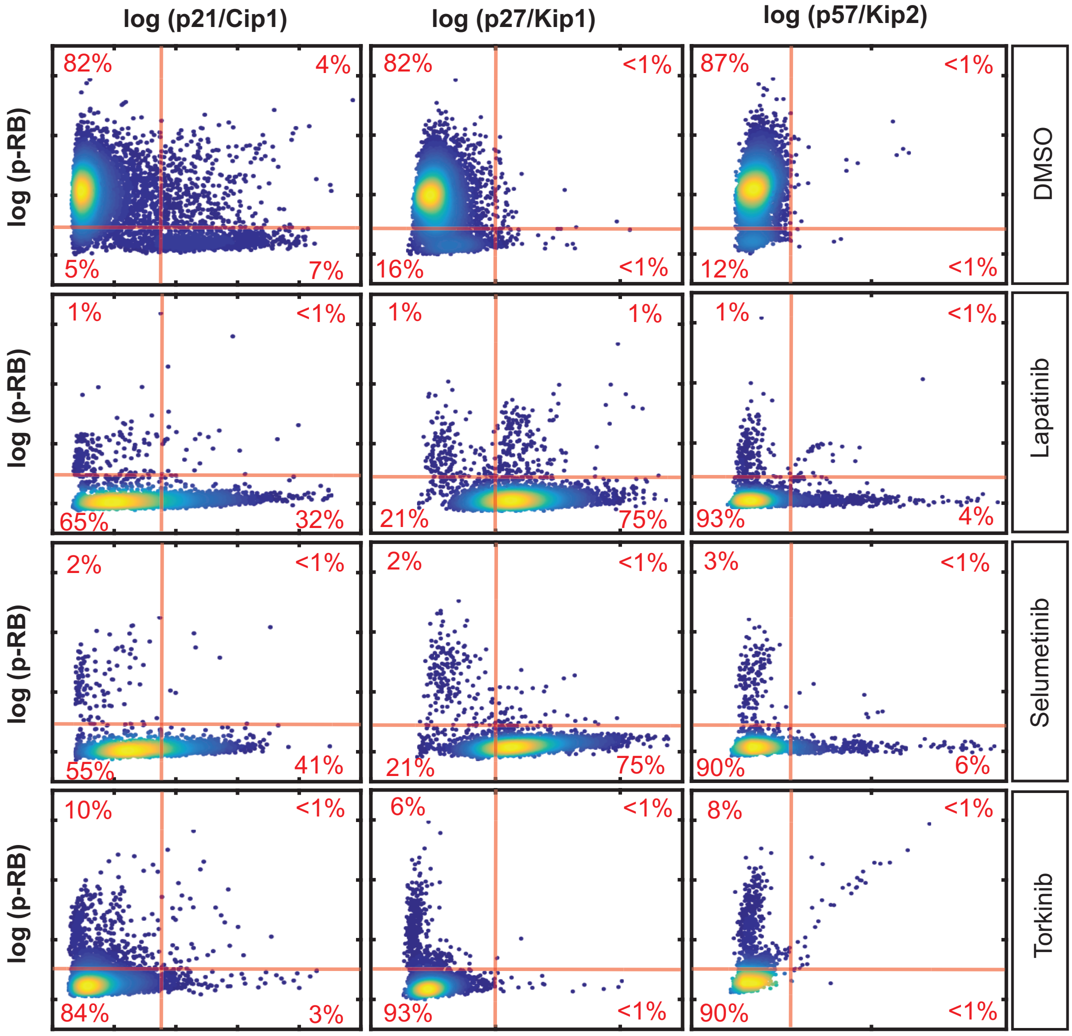

Figure 3.17 Molecular details of cytostasis are different from one drug to the next.

Abundance of CDKIs (p21/Cip1, p27/Kip1 and p57/Kip2) was assessed across non-treated cells and highest tested dose of 3 inhibitors of EGFR (Lapatinib), MEK (Selumetinib) and mTOR (Torkinib). Unlike mTOR inhibitor (Torkinib) that shows reduction in p21/Cip1 and no induction of p27/Kip1 and p57/Kip2, EGFR- (Lapatinib) and MEK- (Selumetinib) targeting drugs lead to upregulation of all measured CDKIs.

1.5.2 Results from cyclic immunofluorescence (CycIF) imaging

1.5.2.1 *K*-means clustering in PCA space

Cell cycle regulators have previously been implicated as drivers of phenotypic cell-to-cell variability (Buettner et al., 2015; Overton et al., 2014; Patel et al., 2014; Powers and Satija, 2015) (Figure 3.15). Because different drugs also elicited distinct co-distributions of p-Rb with the CDKI proteins p21/Cip1, p27/Kip1, and p57/Kip2 in pairwise co-stained MCF10A cultures, we decided to escalate the dimensionality of observed co-distributions to 19 signaling readouts by means of CycIF measurements after 24 hours of drug treatment. To survey unperturbed cultures for distinct subpopulations, we conducted *k*-means clustering, starting with $k = 5$ and using the cosine distance metric, which distinguishes the directions of marker combinations in signaling space. We then iteratively merged clusters while projections along pairwise centroid lines were not bimodal. Because this procedure yielded $k = 3$ well-defined clusters, we projected the single-cell densities into the plane defined by cluster centroids (Figure 3.18). This projection revealed a difference between the two most populated clusters mostly in an increase in p-Rb, PCNA, and a decrease in the quiescence marker p27/Kip1. These clusters thus corresponded to proliferating (blue) and non-proliferating cells (black). A third, much less populated cluster (red) could be distinguished from the remaining population by a large increase in γ-H2A.X, p-Histone H3, and pan-p-Aurora staining, each indicative of the mitotic fraction. This shows that our dataset captures at least three distinct proliferation states in unperturbed cultures.

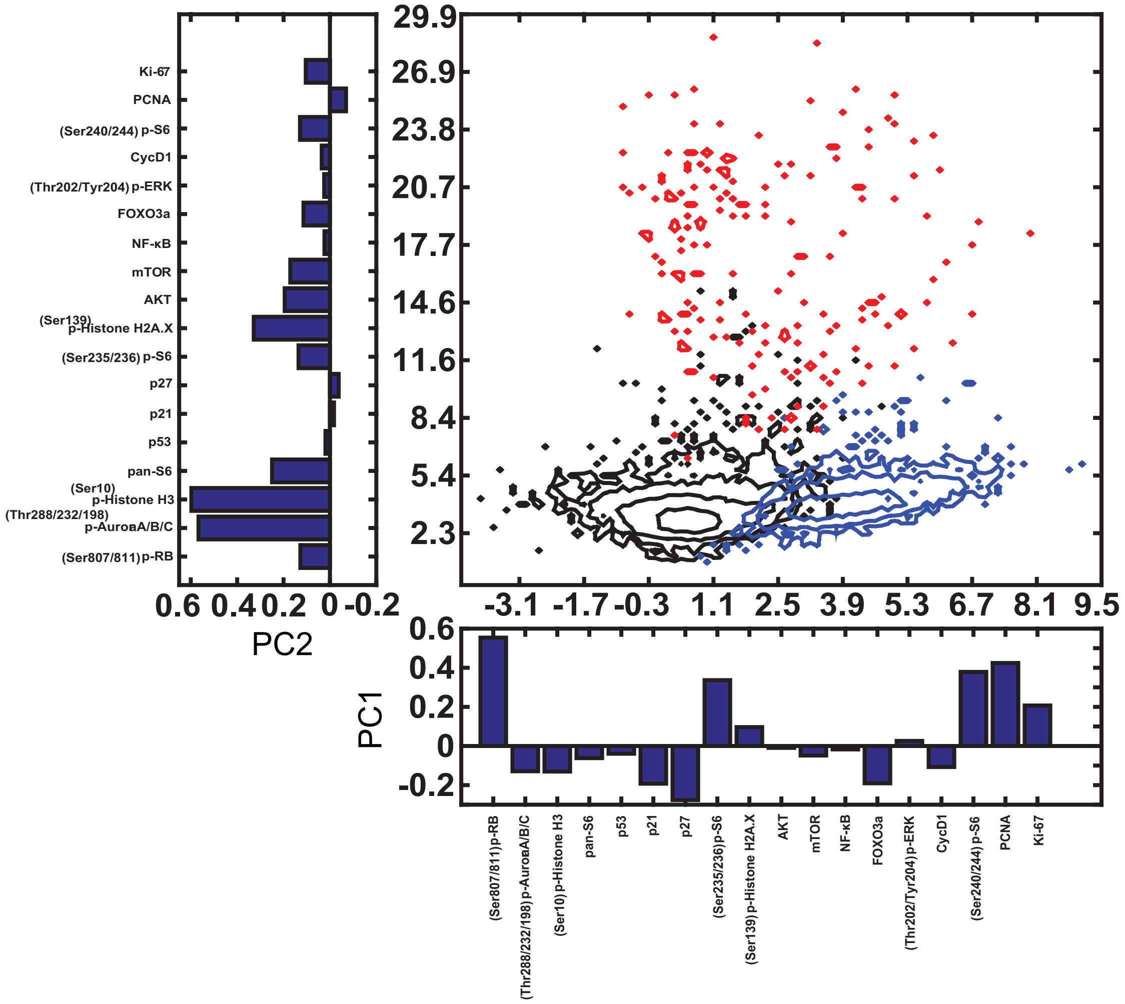

Figure 3.18 *k*-means clustering in unperturbed cells reveals existence 3 distinct cellular states corresponding to cell cycle.

K-means clustering of CycIF data from unperturbed cells showed 3 cluster centers corresponding to quiescence enriched with low levels of p-Rb, p-S6, PCNA (black) and proliferation enriched with high levels of p-Rb, p-S6, PCNA (blue) and mitotic state enriched with p-Aurora and p-Histone H3 (red).

To explore and compare the effects of kinase inhibitors on single-cell co-distributions, we first performed a PCA on all drug-induced shifts of population averages as we did for the dataset obtained by conventional IF microscopy. In agreement with the conventional dataset, the plane spanned by the first two principal components (Figure 3.19) described drug-induced changes that were separable between p-S6 and p-Rb (compass inset). The second principal component reproduced the induction of p27/Kip1 in response to MEK inhibition by Selumetinib that we had observed in traditional IF experiments, and made for an additional reduction in p-Rb. Overall, our coarse analysis raises the hypothesis that p27/Kip1 induction due to MEK inhibition is a critical mechanism that distinguishes kinase inhibitors in their ability to suppress p-Rb-mediated cell cycle progression.

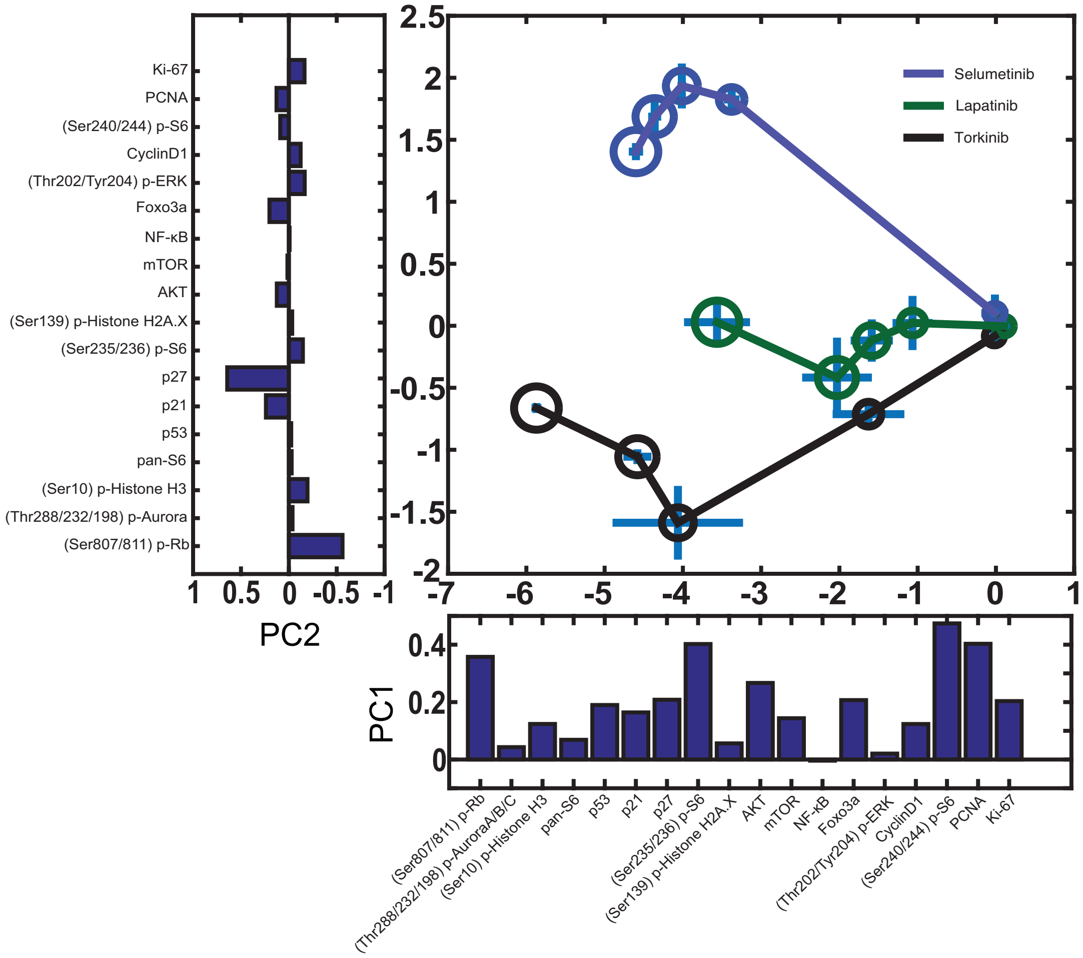

Figure 3.19 Principal component analysis (PCA) of CycIF data is consistent with conventional IF data.

PCA analysis of 3 drugs targeting MEK (Selumetinib), EGFR (Lapatinib) and mTOR (Torkinib). Increasing drug doses are illustrated by increasing sizes of symbols for each drug.

We then used the PCA-derived transformation to project single-cell states into density plots for increasing concentrations of kinase inhibitors (Figure 3.20). The projection revealed a bimodal distribution of proliferation markers in cells treated with DMSO alone, with the largest fraction corresponding to cells expressing high abundances of p27/Kip1. Treatment with high concentrations of any one drug yielded tight unimodal distributions, but Lapatinib- and Selumetinib-treated cells congregated in a state with higher p27/Kip1 concentrations than Torkinib-treated cells. The density plot for cells treated with a close to IC_{50} concentration of Selumetinib revealed that the highest bulk abundance of p27/Kip1 comprised of unusually disperse single-cell distributions. A limitation of this analysis is, however, that the linear projection based on bulk changes is unlikely to capture the full heterogeneity of cells.

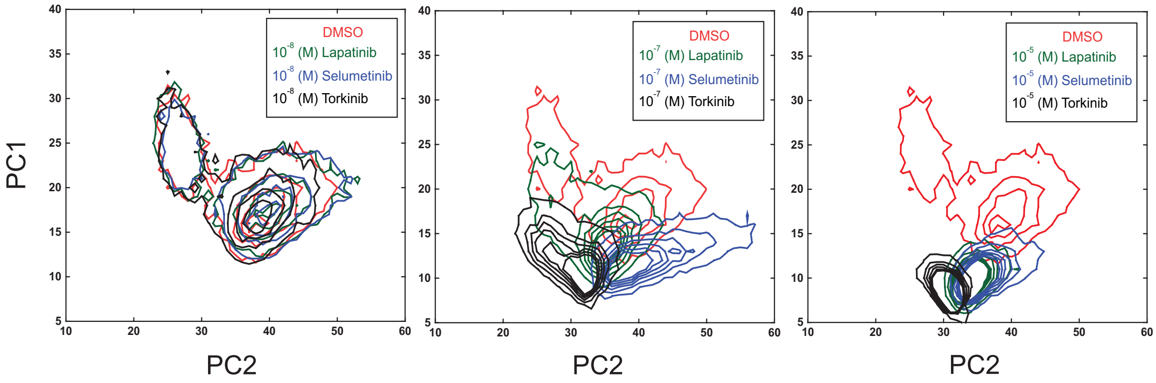

Figure 3.20 Single-cell projection on *k*-means clusters in PCA space reveals differential cytostatic states.

Single-cell projection of k-mean cluster in presence of increasing doses of 3 drugs targeting MEK (Selumetinib), EGFR (Lapatinib) and mTOR (Torkinib) shows differential single-cell distributions.

1.5.2.2 viSNE visualization of drug response data

It is in fact challenging to visualize high-dimensional single-cells data in bi-axial plots and typically dimension reduction methods fail to give good separations of single cells in higher dimension. Thus, we applied a non-linear stochastic neighboring embedding dimension-reduction method (viSNE), which retains high-dimensional structure of data but yields better separations in different sub-populations with distinct signatures. First, four replicates of control/DMSO-treated samples were analyzed by viSNE, and as expected all controls are inseparable (Figure 3.21).

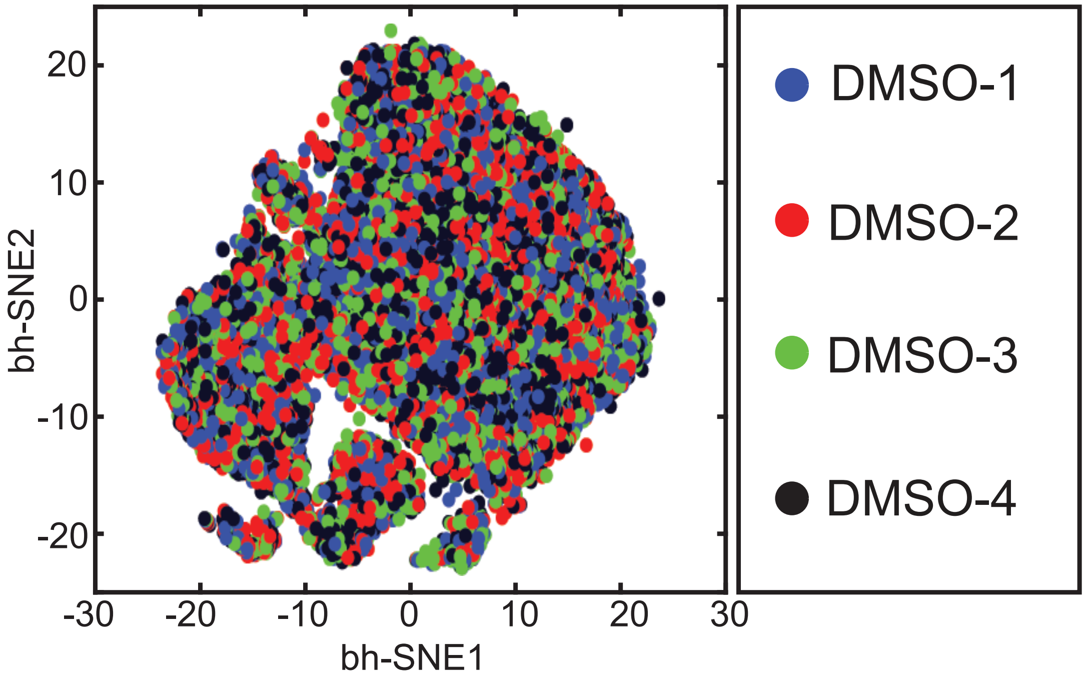

Figure 3.21 DMSO-treated cells in viSNE space are inseparable.
4 independent DMSO-treated samples were compared using viSNE analysis showing that they occupy the same domains in viSNE projection.

However, examining drug-treated samples, shows distinct sub-domains on the viSNE projects, with clear DMSO occupied domain, mTOR/PI3K drugs (Torkinib and Dactolisib) domain and overlapping but still distinguishable domain consisted by EGFR/MEK drugs (Lapatinib and Selumetinib) (Figure 3.22).

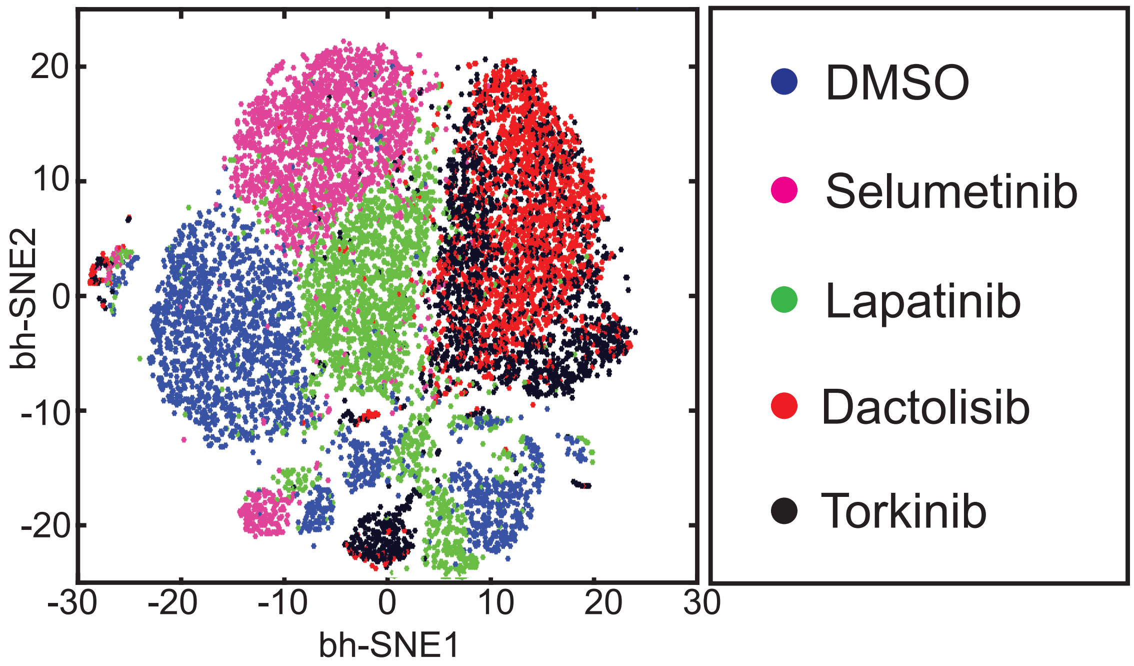

Figure 3.22 viSNE analysis of perturbed cells implies drug specific induced subpopulations.

Single-cell viSNE analysis of drug perturbed states at the GI_{50} *concentrations. DMSO-treated sample (blue), MEK inhibitor (Selumetinib, pink), EGFR inhibitor (Lapatinib, green), PI3K-mTOR inhibitor (Dactolisib, red) and mTOR inhibitor (Torkinib, black) populate different subdomains.*

For the purpose of mapping single-cell heterogeneity in drug induced states, we separated the data by drug target, which further separated clear differences compared to DMSO-treated cells for each drug at the GI_{50} concentration (Figure 3.23).

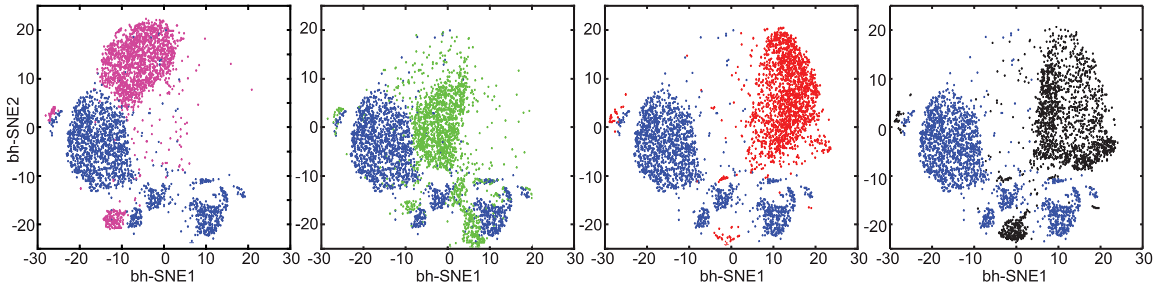

Figure 3.23 viSNE analysis of single drugs implies similarity in single-cell phenotypes across drug target subsets.

Single-cell viSNE analysis of drug perturbed states at the GI_{50} *concentrations. DMSO-treated sample (blue), MEK inhibitor (Selumetinib, pink), EGFR inhibitor (Lapatinib, green), PI3K-mTOR inhibitor (Dactolisib, red) and mTOR inhibitor (Torkinib, black) populate different subdomains. MEK and EGFR inhibitors are similar but distinguishable and PI3K-mTOR inhibitor and mTOR inhibitors show high degree of similarity.*

These results indicate the power of single-cell visualization of CycIF data using viSNE algorithm for potential application in preclinical drug discovery. In order to investigate the variation in single-cell drug responses at the level of signaling, we further examined the distribution of each individual signal by viSNE. As shown in Figure 3.24, viSNE plots indicated that Ki-67 covers the most area of cycling cells, while PCNA and p-RB labeled different subsets of proliferative cells. Interestingly, while Cyclin D1 is normally considered as a proliferative marker, high Cyclin D1 cells were p-RB negative and with strong p21/Cip1 and p53 staining. As previous studies suggested, the subpopulation might correspond to quiescent or senescent states that may be induced by drugs (Chen et al., 2013). By comparing the distribution of signals and their corresponding drug treatments, we found that similar to conventional (IF) results, EGFR and MEK inhibitor (Lapatinib and Selumetinib) treated cells have relatively high levels of p27/Kip1 and FOXO3a compared to mTOR inhibitors (Dactolisib and Torkinib). In addition, we examined the distributions of p-ERK1/2 and p-S6, signals upstream of cell cycle regulators as well as downstream targets of the inhibitors. As we expected, two p-S6 sites are decreased by mTOR targeting drugs and the cells with highest p-ERK signal seem to be enriched in the mTOR inhibitor treated cells, which agreed with the previous findings on the negative feedback loop between PI3K/mTOR and ERK pathways (Carracedo et al., 2008). Lastly, although the Ki-67 plot indicates all these drugs efficiently put cells into non-proliferative state, the γH2A.X plot suggests that the overall DNA damage/cell death were low in these treatments.

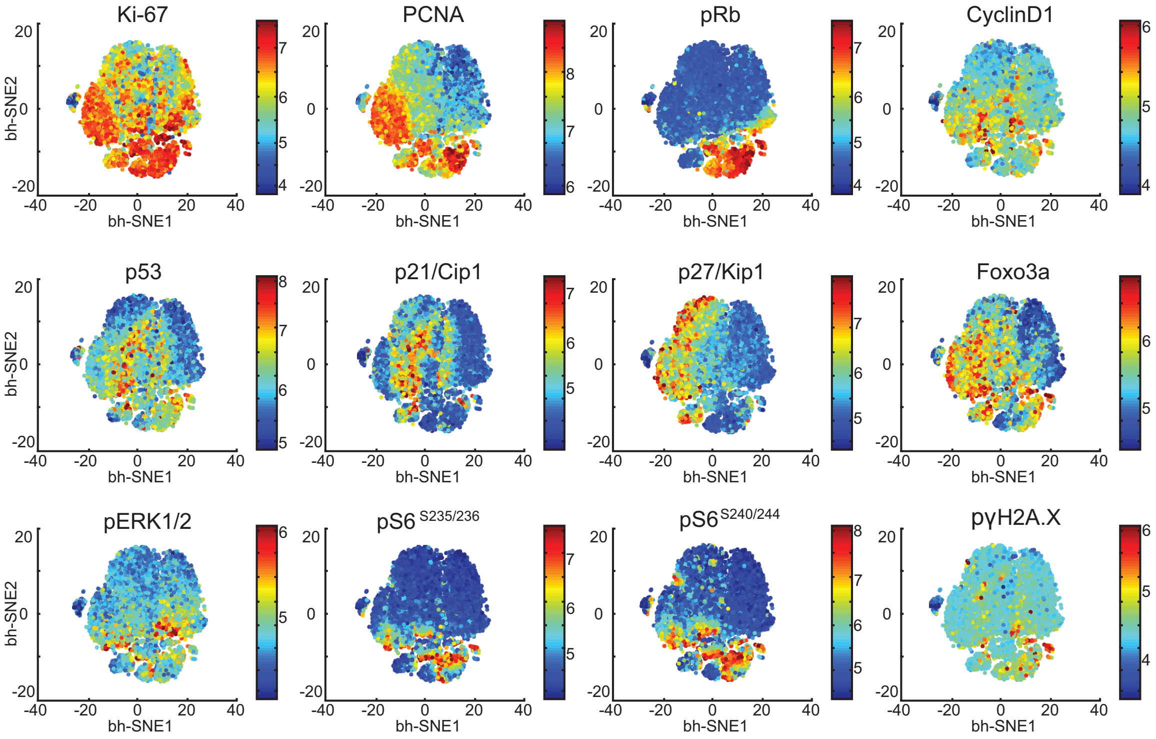

Figure 3.24 viSNE analysis of drug induced domains across 12 signals reveals distinct signaling states across different drugs.

Assessment of enrichment of 12 different drug induced signals in viSNE space. Proliferation markers (Ki-67, PCNA, p-Rb and Cyclin D1) occupy differential domains in viSNE space. Cyclin-dependent kinase inhibitor p21/Cip1 occupies similar domains as p53, while p27/Kip1 occupies similar domain as Foxo3a. p-ERK1/2 remains active in some cells and different active phospho residues on S6 occupy similar single-cell domains.

1.5.2.3 Fractional analysis in viSNE space

In addition to probing the overall signaling responses of different drugs by viSNE, we took advantage of multi-dimensional single-cell data to dissect different phenotypic responses of subpopulations. We resampled the Torkinib treated cells into 3 different sub-populations by gating their p-Rb levels. Surprisingly, we found that cells high with p-RB (drug resistant cells) are mostly enriched in S/G_2, with high Ki-67, PCNA and low p21/Cip1 (Figure 3.25). We also found that these resistant cells might have slightly higher total-AKT, which may account for sensitivity to PI3K/mTOR inhibition.

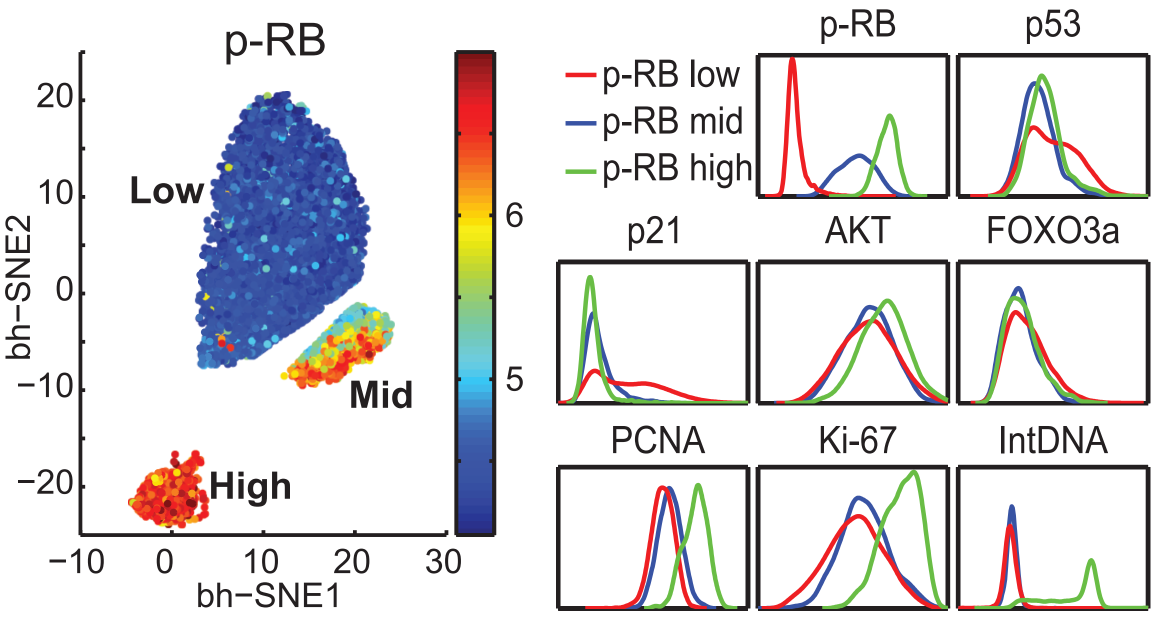

Figure 3.25 Torkinib resistant subpopulation is in S/G_2 cell cycle phase and enriched with markers of proliferation.

In viSNE space, cells that were treated with Torkinib were gated based of p-Rb levels (high, medium and low) (left panel). Cells that are high with p-Rb signal in presence of drug seem to be in S/G2 cell cycle phase based on DNA content and enriched with markers of proliferation (Pan-AKT, PCNA and Ki-67, left panel). Cells with low p-Rb signal seem to have high levels of p21/Cip1.

1.5.2.4 Wanderlust visualization of steady states

Even though, the viSNE algorithm was powerful in visualizing high-dimensional subpopulation differences in mTOR targeting drugs by keeping single-cell information intact, due to static representation of the signals in such analysis, it lackes clear information on transitional states. Thus, we addressed this issue by performing Wanderlust algorithm on CycIF dataset initially for cell cycle regulating proteins in unperturbed cells (Figure 3.26).

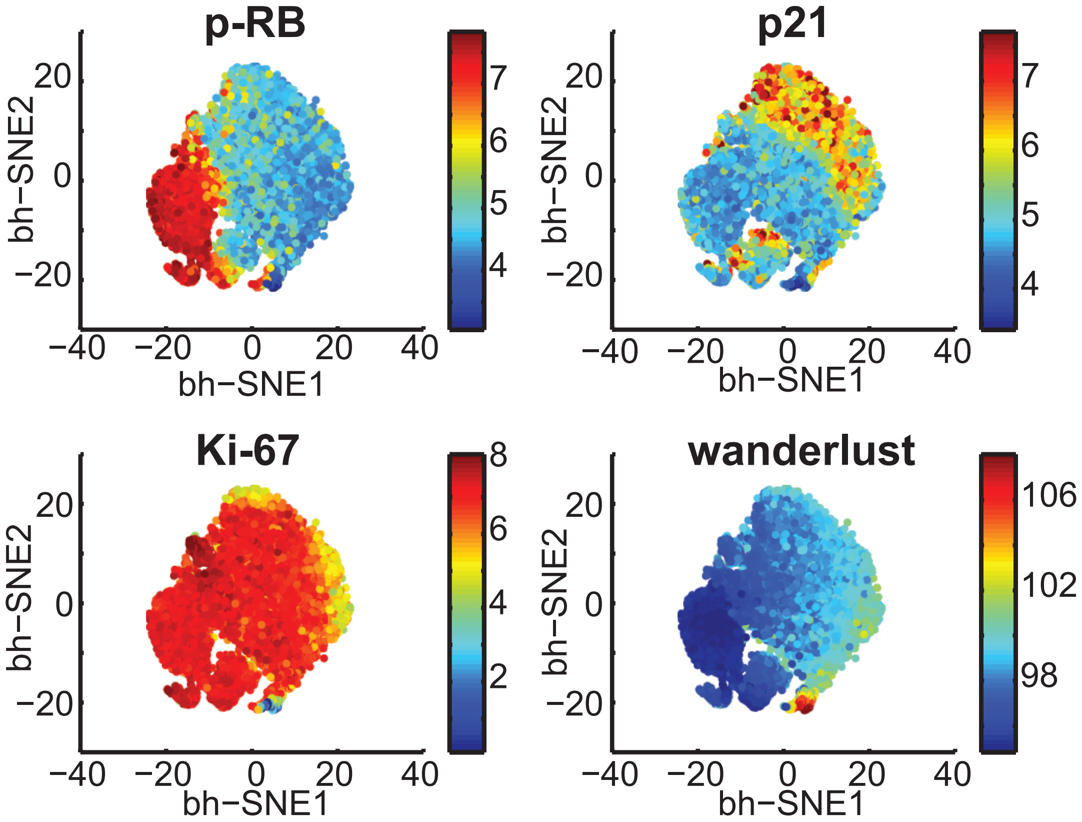

Figure 3.26 Single-cell distribution of cell cycle markers in viSNE space combined with Wanderlust axis recapitulates direction of cell cycle progression.

Single-cell distributions of cell cycle markers such as p-Rb, Ki-67 and p21/Cip1 in single cells shows distinct cellular states. Wanderlust overlay on viSNE space shows the direction of cell cycle progression (bottom right).

Additionally, we were able to reconstitute different stages of cell cycle from Wanderlust trajectory. In G_0/G_1 stage, DNA content is the lowest accompanied by low levels of p-RB and rising levels of Ki-67, PCNA and Cyclin D1 as well as accumulation of p27/Kip1 and p21/Cip1. In G_1/S phase, levels of Ki-67 and Cyclin D1 continue to rise at a slower rate, whereas PCNA levels do not rise much while the levels of p27/Kip1 and p21/Cip1 decline, former with a slow and latter with a faster rate until cells pass the restriction point and commit to DNA synthesis that is accompanied by a sharp increase of p-RB. In S/G_2/M cell cycle stage, p27/Kip1 and p21/Cip1 continue to degrade with similar rates accompanied by degradation of Cyclin D1 and this time levels of Ki-67 reach a plateau, while the PCNA levels sharply rise (Figure 3.27).

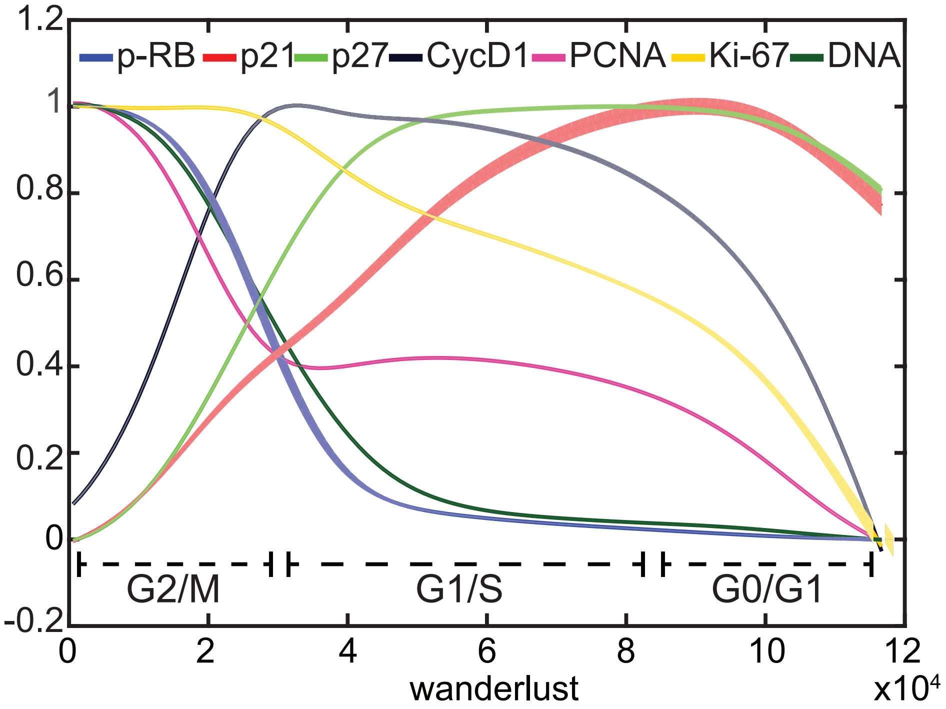

Figure 3.27 Reconstruction of cell cycle progression by Wanderlust analysis of static cell cycle regulator markers.

Different markers of cell cycle progression such as p-Rb, p21/Cip1, p27/Kip1, Cyclin D1, PCNA, Ki-67 and DNA content were measured in unperturbed cells and Wanderlust analysis correctly reconstituted G_0/G_1, G_1/S and G_2/M cell cycle stages.

In principal, Wanderlust graph-based trajectory reconstruction is useful in understanding the dynamical changes in abundance of proteins along a continuous system such as cell cycle. However, it is able to reconstruct only non-branching trajectories, underlining a requirement for different analytical methods to study bifurcating cell populations. This is crucial as we show in the viSNE section that all tested drugs generated significant cell-to-cell heterogeneity, particularly when their response was incomplete ($E_{max}>0$). Different subpopulations of cells arise in this case because of branching in cell cycle trajectories, with some cells exiting the cell cycle and others continuing to proliferate. Newly developed algorithms such as Wishbone (Setty et al., 2016) can deal with bifurcations in developmental systems, however to the best of our knowledge have not been tested in pharmacology so far.

4. DISCUSSION

Discovery and development of new medicines is expensive and prone to failures (Bains, 2004; Swinney and Anthony, 2011). Reducing the high cost of failures could remove a huge burden from pharmaceutical companies and opens possibilities to focus investments on R&D in a more productive manner. Among many reasons for failure in development of new drugs, safety and efficacy seem to play a major role (Hughes et al., 2011). While there are only limited approaches to assess drug safety in preclinical studies, the potential applications of novel technologies and computational frameworks in preclinical stages of drug discovery is evident (Sorger et al., 2011). Recruitment of such approaches in early phases of drug development will likely lead to lower number of potential drug candidates progressing to late clinical phases, but at the same time increases the likelihood of success in a few rigorously tested safe, potent and effective chemical agents to be approved and used in therapy (Paul et al., 2010).

Understanding the molecular mechanisms of drug action requires characterizing drug-induced changes in cellular states. In the case of targeted anti-cancer drugs these typically involve inhibition of oncogene signaling, changes in cell cycle distribution and induction of senescence or apoptosis. Conventional high-throughput screening approaches that examine bulk drug effects fail to systematically assess this complexity and multiplex methods are required to collect well-average drug dose-response data for multiple molecular signals and cellular phenotypes along a response pathway. Because imaging allows data to be acquired at relatively low cost, it is feasible to obtain detailed information on the impact of dose and time across multiple compounds. We believe that this will be particularly useful in the later stages of pre-clinical drug development in which the aim is to select candidates among dozens of lead compounds with similar structures (structure-activity relationships).

In this thesis, we have shown that microscopy represents effective means to characterize differences among drugs that relate to drug resistance or sensitivity. We show how the focus to date on drug potency (typically IC_{50} or AUC) ignores the potential impact and biological importance of variation in other parameters, such as the steepness of the dose-response curve hill slope (HS) or differences in maximum effect (E_{max}). Interestingly, analysis of drug dose-response curves revealed that within effective drug groups, drugs that have different potency seem to lead to similar levels of growth inhibition at highest tested dose of each drug. In addition, unlike drugs that target intracellular biochemical nodes like MEK (PD0325901 and Selumetinib), AKT (MK2206 and Triciribine) or mTOR (Dactolisib and Torkinib) that have shallow dose response curves (HS<~1), EGF receptor targeting drugs (Erlotinib, Gefitinib and Lapatinib) lead to much steeper dose responses (HS >1.5).

Averaged analysis of activity for a few signaling kinases like p-ERK1/2, p-S6 and p-4EB-BP1 post perturbation with the drug panel, revealed significant molecular complexity underlying the phenotypic differences. For example, the PI3K/mTOR inhibitor Dactolisib was a very potent suppressor of the phosphorylation of S6 and 4E-BP1, two major proteins involved in translational control, whereas Selumetinib, which is even more potent as an inhibitor of cell growth, had little effect. In the case of the mTOR inhibitor Torkinib, we observed dose-dependent increases in p-ERK1/2, a pro-growth counter therapeutic effect consistent with negative regulation of MAP kinase signaling by mTOR.

To investigate the role of MAPK signaling in drug response and importance of time and dose on phenotypic regulation, we screened the response of a panel of non-transformed as well as cancer cell lines to Lapatinib; an FDA approved small-molecule dual tyrosine kinase inhibitor targeting EGFR/HER2 and showed that the dynamics of ERK phosphorylation is important in predicting the response to Lapatinib in a way that ERK phosphorylation is a good predictor of late phenotypic response only at intermediate time points. In fact, unlike intermediate p-ERK1/2 response, early-immediate p-ERK1/2 signal response can only poorly predict the phenotype. We investigated the origins of p-

ERK1/2 recovery post treatment with Lapatinib in one of the resistant cell lines (MCF10a) by providing evidence against drug efflux, metabolization or activation of an autocrine loop.

Through time series experiments, using combination of high-content imaging, ELISA and western blot methods we provided evidence toward a dynamic behavior of drug target (EGFR/HER2) post exposure to Lapatinib. Since our aim was to examine a focused case in a typical protocol used in high-throughput drug screens, we assessed Lapatinib response using the exact protocol. In this protocol drug is combined with full serum media and added to cells, which could influence cell signaling in steady state. In basal conditions, most EGFR seemed to be localized in the cytosol as punctuates, likely in multivesicular bodies. Upon drug exposure, immediate reduction in EGFR phosphorylation at multiple residues is detected, cytosolic EGFR translocates to plasma membrane, where it has access to extracellular EGF ligand in the full serum media, which in turn leads to EGFR reactivation and p-ERK1/2 recovery. This translocation was associated with a reduction in the number of intracellular EGFR and clathrin heavy chain punctates suggesting a clathrin-mediated receptor internalization in basal conditions. In order to sustain EGFR/ERK inhibition, we hypothesized that by combining two inhibitors for the same target (EGFR), we could not only sustain the EGFR/ERK inhibition by a synergistic effect, but also reduce the toxicity caused by high concentrations of drugs as each single agents used as monotherapy. In result, we observed that the combination of Lapatinib and Gefitinib caused p-ERK1/2 to remain inhibited as measured at 24 hours, which also resulted in the inhibition of a downstream cell cycle regulator (p-Rb). It is of importance to note that EGFR/ERK recovery only occurred at the Lapatinib concentrations below sub-saturation. In fact, the shift of p-ERK1/2 IC_{50} between immediate and intermediate time points happens only at concentrations below 3.2 nM suggesting that the activation of reserved intracellular EGFR fraction does not lead to recovery at high concentrations due to the presence of sufficient drug amounts of drug in the surrounding microenvironment. This alone, at least partially explains the steep hill slope of the response to Lapatinib. Because all EGFR molecules need to remain inhibited in order to sustain pathway inhibition consistent with the regulation of EGFR activity by threshold effects (Sigismund et al., 2013).

In order to identify the dominant signaling axis of drug response, we performed principal component analysis on bulk drug effects and applied PCA to the relative changes of signaling readouts. Two PCs captured ~90% of variance, indicating that the bulk signaling changes in response to all drugs explored in this dataset can be understood within a plane spanned by two axes. One axis (PC1) corresponded primarily to the phosphorylated levels of the CDK2 cell cycle kinase (p-CDK2). PC2 largely comprised p-ERK1/2 with negative loading and the phosphorylated forms of the ribosomal S6 subunit (p-S6$^{S235/236}$) and of the translation repressor 4E-BP with positive loadings. S6 is activated by phosphorylation at multiple sites by TORC1 (Gonzalez et al., 2015) and by the p90 ribosomal S6 kinase (RSK; which in turn lies downstream of the MEK/ERK kinase cascade). Thus, virtually all of the effects of the nine drugs tested can be captured in a two-dimensional landscape in which proliferation (p-CDK2), MAPK signaling (p-ERK1/2) and protein translation (p-S6) are the most important molecular features.

Dose-response trajectories were distinct for each target class, with PC2 accounting for the greatest variation. For example, the AKT inhibitors (MK2206 and Triciribine) resulted in dose-response trajectories that were similar to each other, yet distinct from those of the mTOR inhibitors (Dactolisib and Torkinib). The three ErbB receptor inhibitors tested, Gefitinib, Lapatinib and Erlotinib were also similar to each other, however distinct from all other drug classes. Altogether, the tight grouping of dose-response trajectories by drug class in signaling space suggests high selectivity of these compounds. The signaling plane identified by PCA also serves to illustrate that with increasing dose of mTOR drugs, the dose-response trajectories depart from a pure effect along the S6 axis and progressively induce mitogenic ERK signaling. In contrast, MEK inhibitors affected readouts more broadly and resulted in trajectories with many other components orthogonal to the p-ERK1/2 vector. Thus, MEK inhibitors did not point in the opposite direction from p-ERK1/2.

Multiple methods exist for normalizing and scaling experimental data prior to analysis methods such as PCA and it is not always clear which is the most appropriate method of choice for a given data set. Initially, raw intensity values obtained from image processing algorithms were divided by intensity values for DMSO only controls to obtain $\log_2$ fold-change ratios. As an alternative approach that aimed to highlight the elevated signaling states in drug-treated cells, log ratios were normalized by the cell-to-cell variability (as measured by standard deviation) for each IF signal in unperturbed cells. PCA of data normalized in this way yielded different loadings with the abundance of p27/Kip1 as the primary PC1' loading and p-4E-BP1 as the primary PC2' loading; PC1' and PC2' captured 75% of variance. Drug-response data projected differently in the PCA space defined by PC1'/PC2' relative to PC1/PC2 but key biological features were retained. For example, in both cases drugs with similar targets mapped close together and drugs with different targets were distinct. PC1 and PC1' were nearly the opposite of each other, consistent with mutually antagonistic interactions between CDK2 and p27/Kip1. With respect to PC2 and PC2', it is reasonable to consider p-4E-BP1 as a stand-in for pS6, given that both lie downstream of AKT/mTOR. Thus, even though the two PCA plots appear to be different, they both capture the fact that the drugs tested move cells across a plane defined by cell cycle progression and protein translational activity.

Single-cell profiling uncovers relationships between drug-target engagement and induction of cellular phenotypes that are obscured by population average methods, fitting well into the workflow of drug discovery. It can also be very economical with respect to reagents and numbers of cells (an important consideration with patient-derived materials). The data described in this thesis illustrate the potential of simple well-average data derived from imaging to characterize the diversity of cellular response to drugs. The analysis and insights are fundamentally similar to what can be achieved with multiplex biochemical assays. However, for proteins and modification states that are bimodally distributed across the cell cycle, such as p-CDK2, averaging signals across an entire plate is suboptimal. We therefore compared the correlation between the computed *AUC* of average relative upstream signals such as p-ERK1/2 and p-S6 as well as averages of most downstream signals such as p-CDK2 response curves and the *AUC* of the growth inhibition curve at 48 h and compared this to the correlation between fraction p-CDK2 positive fraction and phenotypic response. We observed no linear relationship between p-ERK1/2 or p-S6 and the phenotypes when all drugs were loaded in the model, however averaged p-CDK2 response correlated well with growth inhibition (R^2=0.71). A statistically significant (p=0.02 by Fisher's r-to-z transformation test) improvement was achieved when instead of averaged p-CDK2, the fraction double-positive p-CDK2/p-Rb fraction was used in the regression model (R^2=0.91).

Furthermore, to assess the molecular details of single-cell cytostatic phenotypes induced by drugs at the highest tested dose, we plotted of Cyclin-dependent kinase inhibitors (CDKIs) (p21/Cip1, p27/Kip1 and p57/Kip2) abundance against p-Rb to quantify quiescent and proliferative subpopulation fractions. Analysis of the single-cell scatter plots revealed significant differences in molecular phenotypes induced by different drugs. Even though the averaged relative growth of all drugs, aside from AKT targeting-drugs were similar (E_{max} ~ 1), mTOR targeting-drugs like Torkinib not only led to accumulation of p27/Kip1 and p57/Kip2, but also reduced p21/Cip1 levels, whereas EGFR and MEK targeting-drugs perturbed all 3 CDKIs. These results underlie the value of high-content single-cell microscopy in characterization of drug-induced cellular phenotypes, given that similar bulk growth inhibition does not necessarily correspond to similar cytostatic phenotype at single-cell level.

Analysis of the well-average changes induced by a representative subset of the kinase inhibitors (one drug per target class) in the highly multiplexed CycIF dataset yielded comparable observations with respect to the underlying biology, although the sets of antibodies used for conventional IF and CycIF were largely distinct due to differing criteria for selection and optimization. For example, a

PCA of the well-averaged changes also revealed a planar surface that is sufficient to distinguish all drug classes. In this dataset as well, induction of p27/Kip1 is the major upstream distinction between the molecular effects of Torkinib, Lapatinib, and Selumetinib. A fundamental advantage of highly multiplexed single-cell measurements is the ability to reveal correlations between different signals within a population beyond the bulk changes. Such correlations can be used to infer functional relationships among proteins that are obscured by population average measurements or even by multiple-rounds of single-cell low-plex measurements.

As a first step in analyzing single-cell distributions in CycIF data, we performed *k*-means clustering and chose unperturbed cells. We started with $k = 5$ clusters and used the cosine distance metric, which distinguishes marker combinations primarily by their orientation in signaling space. We then iteratively merged clusters in cases where projections along pairwise centroid lines were not bimodal. This procedure yielded $k = 3$ well-defined clusters that can be projected as single-cell densities into a plane defined by cluster centroids. These clusters appear to correspond to three distinct cell cycle states. Most populated cluster (77% of cells) was distinguished from the next-most populated cluster of cells (22%) by lower levels of pRb, PCNA, and higher levels of p27/Kip1, suggesting that the clusters correspond to non-proliferating and proliferating cells. A third, relatively disperse cluster (red, 1%) was distinguished by higher γ-H2AX, p-Histone H3, and p-AuroraA/B/C staining, each of which is indicative of mitosis. A limitation of this analysis is, however, that a linear planar projection is unlikely to capture the full heterogeneity of the cells, and that no additional states or transitions of cell cycle progression were resolved by *k*-means.

Graph-based trajectory reconstruction can be used as means to interpret high-dimensional data based on the inference of temporal order. It has been shown that cell-cycle trajectories can be reconstructed from fixed cell images (Kafri et al., 2013) and complex differentiation programs from CyTOF data (Bendall et al., 2014). The Wanderlust algorithm accomplishes this by connecting nearest neighbors among subsampled single-cell readouts as a means to place them on single axis (Gut et al., 2015). When applied to CycIF data from unperturbed MCF10A cultures, the Wanderlust algorithm indeed reconstructed known cell cycle transitions, in support of antibody selectivity and the notion that CycIF data captures a rich set of biological information. We saw that on the Wanderlust axis, normalized DNA content (Hoechst 33342 staining) is low from $6x10^4$ to $12x10^4$, at which point it rises steadily, concomitant with a rise in Rb phosphorylation. Between $6x10^4$ and $12x10^4$ the levels of the p21/Cip1 and p27/Kip1 CDKIs were high and Cyclin D1 levels increased rapidly. These trajectories recapitulated well-documented changes in cell cycle regulators whereby expression of Cyclin D1 in G_0/G_1 permits CDK2 to overcome p27/Kip1 inhibition and mark it for degradation. This leads to activation of a switch that leads to Rb phosphorylation and thereby, licensing of DNA replication, and entry into S phase. Cyclin D1 concentration occurs in cells with 4N DNA followed by mitosis in cells with high PCNA levels, at which point the Wanderlust plot can be assumed to wrap over to the left.

Multiplex imaging reveals that the exposure of cells to targeted anti-cancer drugs induces cell cycle states that are not found in normal cells and that these can be heterogeneous across the population. We and others and we have linked such heterogeneity among genetically identical cells to submaximal drug response and the perdurance of drug-resistant subpopulations potentially involved in residual disease. The t-SNE implementation viSNE yields a flat projection that better represents heterogeneity than conventional projection of *k*-means clusters and has previously been shown to work well with CyTOF data (Amir el et al., 2013). The same data used to generate the Wanderlust plot were projected here using viSNE algorithm. The viSNE plots from p-RB and Ki-67 stainings (both of which are markers of cell proliferation) occupy the territories opposite to the p21/Cip1 (negative cell cycle regulator). When viSNE was used to project data from untreated MCF10a and cells color-coded by Wanderlust index, we observed that the cell cycle precedes counter-clockwise through the projection. A “peninsula” in the edge of the viSNE space encompasses the Ki-67 negative cells subset of non-cycling cells and likely corresponded to the quiescent fraction of the MCF10A culture. As a control in contrast, merging four replicate sets from DMSO-treated cultures yielded a viSNE projection in which none of the replicates segregated.

To compare drug responses at a single-cell level we merged CycIF data from cells treated with each of the four different kinase inhibitors or with DMSO alone. The doses of drugs used here were selected to lie between GI_{50} and GI_{80}. Projecting the data with viSNE yielded a landscape in which different drugs mapped to different regions of the space. For example the mTOR/PI3K drugs Torkinib and Dactolisib were distinct from the populated patch corresponding to treatment with the EGFR or MEK inhibitors Lapatinib and Selumetinib. This shows that the localization of cells in the viSNE projection reflects differences in drug response. These projections also demonstrated numerous subpopulations after drug treatment that fragmented landscapes.

To interpret these viSNE clusters at the level of signaling, we color-coded data points in the same viSNE projection according to the relative intensity of each CycIF signal. Antibodies specific to different cell cycle proteins and phosphorylation states revealed multiple subpopulations distinguished by antigens commonly thought to exhibit similar regulation of biological processes. Specifically, antibodies against Ki-67 stained the largest number of cells whereas antibodies against PCNA and p-Rb labeled only distinct subpopulations within the Ki-67 domain. Because Cyclin D/CDK complexes promote Rb phosphorylation, the point in the cell cycle at which Cyclin D1 abundance is highest is usually thought to correspond to the point of maximal Rb phosphorylation. However, we found that cells with the highest Cyclin D1 concentrations were p-Rb negative and exhibited strong p21/Cip1 and p53 staining. This subpopulation likely corresponds to a non-proliferative state that has previously been described as an alternative mode of cell cycle exit (Chen et al., 2013).

Consistent with our PCA of the traditional IF drug screen dataset, viSNE domains populated by cells treated with EGFR or MEK inhibitor (Lapatinib or Selumetinib) featured higher levels of p27/Kip1 (and also FOXO3a) than viSNE domains corresponding to mTOR inhibition by Dactolisib or Torkinib. When we examined the distribution of p-ERK1/2 and p-S6, which function as signals downstream of all drugs in our panel but upstream of cell cycle regulators we found that viSNE domains corresponding to treatment of cells with Torkinib exhibited greatly reduced S6 phosphorylation at S235/236 and S240/244 but high p-ERK1/2 levels. This is in agreement with previous data showing that mTOR inhibition relieves ERK from negative feedback, albeit through an unclear mechanism (Albert et al., 2009; Carracedo et al., 2008).

To explore the ability of viSNE to dissect drug responses in cell subpopulations in comparison with classic scatter plots, we gated on the cluster of Torkinib-treated cells that featured the highest p-Rb levels and examined the marginal distributions of the signaling proteins in this cluster. This analysis revealed strong Ki-67 and PCNA expression, low p21/Cip1 and p27/Kip1 expressions and 2N DNA content indicative of S/G_2-like cells that are still proliferating. We conclude that although most MCF10A cells arrest in the presence of Torkinib, a subset of cells escapes this effect, which may underlie the reduced E_{max} observed for Torkinib. More generally, the ability to isolate this subset suggests that our dataset is informative of abnormal cell cycle states that may potentially underlie resistance.

Further research is required to test these ideas. However it is evident that the near-universal use of population average measurements to characterize drug response at cellular level is prone to missing important information. However, effective analysis of single-cell data involving drug-induced subpopulations and cell-cycle bifurcations will requires the development of new algorithms. Existing graph reconstruction methods such as Wanderlust and Wishbone are not yet fully able to fully deal with this complexity in the context of pharmacology.

While multiplex single-cell imaging using methods such as CycIF are no more complicated than conventional IF, they are substantially cost-effective since they cut down on the amount of cell culture material and reveal connections between molecular signals and phenotypes that cannot be discerned using population average methods or multiple rounds of low-plex measurement across many cell culture samples. Cell cycle progression, for example, can be directly inferred from such data using graph-based trajectory reconstruction. The image segmentation and analysis routines used in this thesis are intentionally simple ones and primarily yielding per-cell intensity data. The addition of morphometric data (on cell shape or the organization of the cytoskeleton for example) will most certainly yield additional insight. I hope that the data in this thesis will motivate methodologies for analyzing or visualizing of high-dimensional single-cell data on normally growing and drug-treated cells.

5. SUMMARY

The activities of small molecule anti-cancer drugs are commonly measured in cell-based assays as means to optimize drug properties, study biological processes such as cell growth and death, and identify factors that control drug sensitivity and resistance. Most of these assays involve measurement of a single parameter in drug-treated cells, commonly the number of viable cells. However, understanding the mechanisms of action of therapeutics requires characterizing drug-induced changes in intracellular states. This typically involves inhibition of oncogene signaling, changes in cell cycle distribution and induction of senescence or apoptosis. Near-universal use of conventional single-parameter screening techniques used in drug discovery fail to systematically assess this complexity. Thus, multiplex methods are required to collect drug dose-responses from multiple molecular signals and cellular phenotypes along a response pathway. Multiplex assays such as flow-based methods have the potential to provide data on many more features of drug-perturbed cells but are difficult to perform in high-throughput on adherent cells; bead-based immuno-assays are expensive and provide only well-average data. In this thesis, we argue that high-content and high-throughput microscopy is ideal for this purpose as it not only combines aspects of phenotypic and target-centric approaches in cell populations, but also sheds light on the molecular details of drug-induced phenotypes at single-cell level.

Analysis of phenotypic dose-response curves from 9 kinase inhibitors measured by high-throughput microscopy revealed systematic similarities and variations between different drugs. For example, EGFR-targeting drugs exhibited much steeper hill slope (HS) compared to drugs targeting MEK, AKT or mTOR. While all effective drugs had similar averaged maximal cytostatic effects (E_{max}~1.1), the accumulation of Cyclin-dependent kinase inhibitors (CDKIs) varied from one drug to the next.

Principal component analysis (PCA) on the measured molecular signals captured 90% of the variance in two principal components (PCs) indicating that the bulk signaling changes in response to all explored drugs can be understood within a plane spanned by two orthogonal axes of protein synthesis (p-4EBP1 and p-S6) and cell cycle progression (p-CDK2, p27/Kip1). Interestingly, mTOR inhibition caused dose-dependent upregulation of ERK1/2 phosphorylation that may be counter-therapeutic. Furthermore, we investigated the importance of MAPK signaling dynamics in a panel of immortalized and cancer cell lines in response to a dual EGFR/HER tyrosine kinase inhibitor (Lapatinib). Averaged ERK1/2 phosphorylation response curve at intermediate time points was highly correlated with the late phenotypic response (R^2=0.96) and the transient p-ERK1/2 inhibition was associated with translocation of EGFR to plasma membrane and recovery of EGFR phosphorylation. Combination of two EGFR inhibitors led to sustained inhibition of EGFR/MEK/ERK signaling pathway and thereby the inhibition of proliferation measured by Rb phosphorylation.

Even though averaged measurements of drug response is clearly useful in investigating how cells at the population level behave in response to drugs, single cell profiling is increasingly recognized as means to understand natural and induced changes in cellular physiology. Progress has been particularly rapid in the case of highly multiplexed flow-based methods but in contrast, microscopy-based profiling approaches have lagged behind both with respect to the development of easily implemented assays and computational analysis frameworks.

We monitored the response to 4 kinase inhibitors targeting immediate-early signaling pathways in the widely used, non-transformed mammary epithelial cell line using a novel “cyclic immunofluorescence” method (CycIF) capable of imaging up to 30 channels and analyzed the data using existing tools like *k*-means clustering, viSNE and Wanderlust algorithms. We were able to reconstitute different stages of cell cycle from Wanderlust trajectory. Using viSNE algorithm, we showed that different drugs lead to emergence of distinct subpopulations. In particular, response to mTOR targeting drugs was associated with resistance of a subpopulation in S/G_2 cell cycle phase that was highly enriched with markers of proliferation. Thus, highly multiplexed single-cell imaging reveals valuable insight into mechanisms of drug action and cell-to-cell variability in drug response.

6. ZUSAMMENFASSUNG

Die Wirkung von niedermolekularen Krebsmedikamenten wird normalerweise mittels zell-basierten Analysen getestet, um die Wirksamkeit zu optimieren, Erkenntnisse über Zellwachstum und -tod zu gewinnen, sowie Faktoren zu identifizieren, die Resistenz und Sensitivität beeinflussen.

Viele dieser Methoden umfassen die Messung eines einzelnen Parameters der medikamentös-behandelten Zellen, meist die Anzahl lebender Zellen. Um die Wirkmechanismen von Therapeutika zu verstehen, müssen die arzneimittelbedingten Veränderungen auch hinsichtlich des intrazellulären Zustandes charakterisiert werden. Dies beinhaltet üblicherweise die Inhibition der Onkogen-Signalwege, Veränderungen in dem Zellzyklus und Induktion von Seneszenz oder Apoptose. Naheliegende konventionelle Einzelparameter Screening Techniken, wie sie in der Arzneimittelforschung genutzt werden, sind nicht im Stande diese Komplexität methodisch zu bewerten. Deshalb sind Multiplex Methoden erforderlich, um den Dosis-Wirkungs-Verlauf von multiplen molekularen Signalen und zellulären Phänotypen zu erfassen. Multiplex Analysen, wie durchfluss-basierte Methoden, haben das Potential Daten zu vielen Eigenschaften von medikamentös behandelten Zellen zu liefern, es ist aber schwierig dieses im Hochdurchsatz mit adhärenten Zellen durchzuführen. Bead-basierte Immuntests sind teuer und liefern nur Durchschnittswerte je Well. In dieser These behaupten wir, dass hochauflösende und Hochdurchsatz-Mikroskopie für diesen Verwendungszweck ideal ist, da nicht nur Aspekte wie Phänotyp- und Ziel-basierende Ansätze, sondern auch molekulare Details der medikamentös-induzierten Phänotypen der einzelnen Zellen einbezogen werden können.

Die Analyse der phänotypischen Dosis-Wirkungs-Kurven von neun Kinase-Inhibitoren, gemessen mittels Hochdurchsatz-Mikroskopie, zeigt systematische

Parallelen, aber auch Variationen zwischen den verschiedenen Medikamenten. Zum Beispiel zeigen EGFR-modifizierte Medikamente einen steileren Hill-Anstieg im Vergleich zu Medikamenten, die MEK, AKT oder mTOR modifizieren. Während alle wirksamen Medikamente vergleichbare durchschnittliche maximale zytostatische Effekte (E_{max}~1.1) hatten, variierte die Zunahme von Cyclin-abhängigen Kinase Inhibitoren (CDKIs) der einzelnen Medikamente.

Die Hauptkomponentenanalyse (PCA) der gemessenen molekularen Signale erfasst 90% der Varianz von zwei wesentlichen Bestandteilen (PCs), daraus ergibt sich, dass ein Großteil der veränderten Signale im Zusammenhang mit allen erforschten Medikamenten mittels einer zweidimensionalen Fläche zwischen orthogonalen Axen für Protein-Synthese (p-4EBP1 und p-S6) und Zellzyklus-Verlauf (p-CDK2, p27/Kip1) beschreiben werden kann. Interessanterweise verursacht die Inhibition von mTOR einen dosisabhängigen Anstieg der Phosphorylation von ERK1/2, der die Wirkung verringern könnte. Außerdem untersuchten wir die Bedeutung von MAPK-Signalwegen in einem “Panel” von immortalisierten und Krebszelllinien in Reaktion auf einen doppelten EGFR/HER Tyrosin-Kinase-Inhibitor (Lapatinib). Im Durchschnitt gab es eine hohe Korrelation des Verlaufs der ERK1/2-Phophorylation mit der phänotypischen Reaktion (R^2=0.96), und die transiente Inhibition von p-ERK1/2 wurde mit der Translokation von EGFR zur Plasmamembran und Wiederherstellung der EGFR Phosphorylation in Zusammenhang gebracht. Die Kombination von zwei EGFR Inhibitoren führte zu kontinuierlicher Inhibition des EGFR/MEK/ERK Signalwegs und in der Folge zur Inhibition der Proliferation, gemessen anhand der Phosphorylierung von Rb.

Obwohl die durchschnittlichen Messungen der Dosiswirkung zweifellos nützlich sind, um das Verhalten der gesamten Zellenpopulation auf die entsprechenden Medikamente zu erforschen, wird die Einzel-Zell-Analyse zunehmend als Möglichkeit für die Erforschung von natürlichen und induzierten Veränderungen in der Zellphysiologie anerkannt. Die Entwicklung war besonders schnell im Fall von Hochdurchsatz-durchfluss-basierten Methoden, demgegenüber war das

Entstehen von Mikroskopie-basiertem “Profiling” verzögert wegen der Entwicklung von einfach umzusetzenden Analysen sowie von rechnerisch analytischen Systemen.

Wir überwachten die Reaktion auf vier Kinase-Inhibitoren, die auf den frühen Signalweg wirken. Wir verwendeten dafür die häufig genutzten, nicht umgewandelten, mamillären epithelialen Zellinien und dazu eine neuartige “zyklische Immunfluoreszenz” Methode (CycIF), die fähig ist bis zu 30 Kanäle gleichzeitig abzubilden. Zur Datenanalyse wurden bereits bestehende Hilfsmittel wie *k*-means-Algorithmus, viSNE- und Wanderlust-Algorithmus verwendet. Wir waren in der Lage verschiedene Abschnitte des Zellzyklus mit der Wanderlust-Zeitschiene darzustellen. Mittels viSNE-Algorithmus konnten wir zeigen, dass verschiedene Medikamente zur Entstehung von eigenständigen Subpopulationen führen. Im Besonderen konnte die Reaktion von Medikamenten die auf mTOR wirken, mit einer Resistenz einer Subpopulation im S/G_2 Zellzyklus in Zusammenhang gebracht werden. In dieser Subpopulation waren Proliferationsmarker sehr stark angereichert. Folglich offenbart das “Multiplex-Single-Cell-Imaging” nützliche Einblicke in die Wirkmechanismen von Medikamenten und Zell-zu-Zell-Variabilität.

7. REFERENCES

Abdul Nazeer, K.A., and Sebastian, M.P. (2010). Clustering biological data using enhanced k-means algorithm. Electronic Engineering and Computing Technology, Lecture Notes in Electrical Engineering 60.

Abràmoff, M.D., Magalhães, P.J., and Ram, S.J. (2004). Image Processing with ImageJ. Biophotonics Intern.

Albert, L., Karsy, M., Murali, R., and Jhanwar-Uniyal, M. (2009). Inhibition of mTOR Activates the MAPK Pathway in Glioblastoma Multiforme. Cancer Genomics & Proteomics *6*.

Amir el, A.D., Davis, K.L., Tadmor, M.D., Simonds, E.F., Levine, J.H., Bendall, S.C., Shenfeld, D.K., Krishnaswamy, S., Nolan, G.P., and Pe'er, D. (2013). viSNE enables visualization of high dimensional single-cell data and reveals phenotypic heterogeneity of leukemia. Nat Biotechnol *31*, 545-552.

Arora, A., and Scholar, E.M. (2005). Role of tyrosine kinase inhibitors in cancer therapy. J Pharmacol Exp Ther *315*, 971-979.

Bains, W. (2004). Failure rates in drug discovery and development: will we ever get any better? In DDW (http://www.ddw-online.com: Drug Discovery World).

Barretina, J., Caponigro, G., Stransky, N., Venkatesan, K., Margolin, A.A., Kim, S., Wilson, C.J., Lehar, J., Kryukov, G.V., Sonkin, D.*, et al.* (2012). The Cancer Cell Line Encyclopedia enables predictive modelling of anticancer drug sensitivity. Nature *483*, 603-607.

Bendall, S.C., Davis, K.L., Amir el, A.D., Tadmor, M.D., Simonds, E.F., Chen, T.J., Shenfeld, D.K., Nolan, G.P., and Pe'er, D. (2014). Single-cell trajectory detection uncovers progression and regulatory coordination in human B cell development. Cell *157*, 714-725.

Buettner, F., Natarajan, K.N., Casale, F.P., Proserpio, V., Scialdone, A., Theis, F.J., Teichmann, S.A., Marioni, J.C., and Stegle, O. (2015). Computational analysis of cell-to-cell heterogeneity in single-cell RNA-sequencing data reveals hidden subpopulations of cells. Nat Biotechnol *33*, 155-160.

Carracedo, A., Ma, L., Teruya-Feldstein, J., Rojo, F., Salmena, L., Alimonti, A., Egia, A., Sasaki, A.T., Thomas, G., Kozma, S.C.*, et al.* (2008). Inhibition of mTORC1 leads to MAPK pathway activation through a PI3K-dependent feedback loop in human cancer. J Clin Invest *118*, 3065-3074.

Chen, J.Y., Lin, J.R., Tsai, F.C., and Meyer, T. (2013). Dosage of Dyrk1a shifts cells within a p21-cyclin D1 signaling map to control the decision to enter the cell cycle. Mol Cell *52*, 87-100.

Dai, C.L., Tiwari, A.K., Wu, C.P., Su, X.D., Wang, S.R., Liu, D.G., Ashby, C.R., Jr., Huang, Y., Robey, R.W., Liang, Y.J.*, et al.* (2008). Lapatinib (Tykerb, GW572016) reverses multidrug resistance in cancer cells by inhibiting the activity of ATP-binding cassette subfamily B member 1 and G member 2. Cancer Res *68*, 7905-7914.

Duckett, D.R., and Cameron, M.D. (2010). Metabolism considerations for kinase inhibitors in cancer treatment. Expert Opin Drug Metab Toxicol *6*, 1175-1193.

Earm, K., and Earm, Y.E. (2014). Integrative approach in the era of failing drug discovery and development. Integrative Medicine Research *3*, 211-216.

Fallahi-Sichani, M., Honarnejad, S., Heiser, L.M., Gray, J.W., and Sorger, P.K. (2013). Metrics other than potency reveal systematic variation in responses to cancer drugs. Nat Chem Biol *9*, 708-714.

Flusberg, D.A., and Sorger, P.K. (2013). Modulating cell-to-cell variability and sensitivity to death ligands by co-drugging. Phys Biol *10*, 035002.

Garnett, M.J., Edelman, E.J., Heidorn, S.J., Greenman, C.D., Dastur, A., Lau, K.W., Greninger, P., Thompson, I.R., Luo, X., Soares, J.*, et al.* (2012). Systematic identification of genomic markers of drug sensitivity in cancer cells. Nature *483*, 570-575.

Gazdar, A.F., and Minna, J.D. (2008). Deregulated EGFR signaling during lung cancer progression: mutations, amplicons, and autocrine loops. Cancer Prev Res (Phila) *1*, 156-160.

Gonzalez, A., Shimobayashi, M., Eisenberg, T., Merle, D.A., Pendl, T., Hall, M.N., and Moustafa, T. (2015). TORC1 promotes phosphorylation of ribosomal protein S6 via the AGC kinase Ypk3 in Saccharomyces cerevisiae. PLoS One *10*, e0120250.

Gut, G., Tadmor, M.D., Pe'er, D., Pelkmans, L., and Liberali, P. (2015). Trajectories of cell-cycle progression from fixed cell populations. Nat Methods *12*, 951-954.

Hanahan, D., and Weinberg, R.A. (2011). Hallmarks of cancer: the next generation. Cell *144*, 646-674.

Heiser, L.M., Sadanandam, A., Kuo, W.-L., Benz, S.C., Goldstein, T.C., Ng, S., Gibb, W.J., Wang, N.J., Ziyad, S., Tong, F.*, et al.* (2012). Subtype and pathway specific responses to anticancer compounds in breast cancer. PNAS *109*.

Hinton, G., and Roweis, S. (2002). Stochastic Neighbor Embedding, U.o.T. Department of Computer Science, ed.

Hoelder, S., Clarke, P.A., and Workman, P. (2012). Discovery of small molecule cancer drugs: successes, challenges and opportunities. Mol Oncol *6*, 155-176.

Hughes, J.P., Rees, S., Kalindjian, S.B., and Philpott, K.L. (2011). Principles of early drug discovery. Br J Pharmacol *162*, 1239–1249.

Janes, K.A., and Yaffe, M.B. (2006). Data-driven modelling of signal-transduction networks. Nat Rev Mol Cell Biol *7*, 820-828.

Kafri, R., Levy, J., Ginzberg, M.B., Oh, S., Lahav, G., and Kirschner, M.W. (2013). Dynamics extracted from fixed cells reveal feedback linking cell growth to cell cycle. Nature *494*, 480-483.

Kleiman, L.B., Maiwald, T., Conzelmann, H., Lauffenburger, D.A., and Sorger, P.K. (2011). Rapid phospho-turnover by receptor tyrosine kinases impacts downstream signaling and drug binding. Mol Cell *43*, 723-737.

Levin, D., Harari, D., and Schreiber, G. (2011). Stochastic receptor expression determines cell fate upon interferon treatment. Mol Cell Biol *31*, 3252-3266.

Lin, J.R., Fallahi-Sichani, M., and Sorger, P.K. (2015). Highly multiplexed imaging of single cells using a high-throughput cyclic immunofluorescence method. Nat Commun *6*, 8390.

Maaten, L.v.d., and Hinton, G. (2008). Visualizing Data using t-SNE. Journal of Machine Learning Research *8*.

Michor, F., and Polyak, K. (2010). The origins and implications of intratumor heterogeneity. Cancer Prev Res (Phila) *3*, 1361-1364.

Overton, K.W., Spencer, S.L., Noderer, W.L., Meyer, T., and Wang, C.L. (2014). Basal p21 controls population heterogeneity in cycling and quiescent cell cycle states. Proc Natl Acad Sci U S A *111*, E4386-4393.

Patel, A.P., Tirosh, I., Trombetta, J.J., Shalek, A.K., Gillespie, S.M., Wakimoto, H., Cahill, D.P., Nahed, B.V., Curry, W.T., Martuza, R.L.*, et al.* (2014). Single-cell RNA-seq highlights intratumoral heterogeneity in primary glioblastoma. Science *344*.

Paul, S.M., Mytelka, D.S., Dunwiddie, C.T., Persinger, C.C., Munos, B.H., Lindborg, S.R., and Schacht, A.L. (2010). How to improve R&D productivity: the pharmaceutical industry's grand challenge. Nat Rev Drug Discov *9*, 203-214.

Powers, A.N., and Satija, R. (2015). Single-cell analysis reveals key roles for Bcl11a in regulating stem cell fate decisions. Genome Biol *16*, 199.

Reguera, R.M., Calvo-Alvarez, E., Alvarez-Velilla, R., and Balana-Fouce, R. (2014). Target-based vs. phenotypic screenings in Leishmania drug discovery: A marriage of convenience or a dialogue of the deaf? Int J Parasitol Drugs Drug Resist *4*, 355-357.

Roses, A.D. (2008). Pharmacogenetics in drug discovery and development: a translational perspective. Nature Reviews *7*.

Samsdodd, F. (2005). Target-based drug discovery: is something wrong? Drug Discovery Today *10*, 139-147.

Setty, M., Tadmor, M.D., Reich-Zeliger, S., Angel, O., Salame, T.M., Kathail, P., Choi, K., Bendall, S., Friedman, N., and Pe’er, D. (2016). Wishbone identifies bifurcating developmental trajectories from single-cell data. Nat Biotechnol *34*.

Sharom, F.J. (2008). ABC multidrug transposters: structure, function and role in chemoresistance. Pharmacogenomics *9*.

Sigismund, S., Algisi, V., Nappo, G., Conte, A., Pascolutti, R., Cuomo, A., Bonaldi, T., Argenzio, E., Verhoef, L.G., Maspero, E.*, et al.* (2013). Threshold-controlled ubiquitination of the EGFR directs receptor fate. EMBO J *32*, 2140-2157.

Sorger, P.K., Allerheiligen, S.R.B., Abernethy, D.R., Altman, R.B., Brouwer, K.L.R., Califano, A., D'Argenio, D.Z., Iyengar, R., Jusko, W.J., Lalonde, R.*, et al.* (2011). Quantitative and Systems Pharmacology in the Post-genomic Era: New Approaches to Discovering Drugs and Understanding Therapeutic Mechanisms (NIH).

Spencer, S.L., Gaudet, S., Albeck, J.G., Burke, J.M., and Sorger, P.K. (2009). Non-genetic origins of cell-to-cell variability in TRAIL-induced apoptosis. Nature *459*, 428-432.

Swinney, D.C., and Anthony, J. (2011). How were new medicines discovered? Nat Rev Drug Discov *10*, 507-519.

Tseng, G.C. (2007). Penalized and weighted K-means for clustering with scattered objects and prior information in high-throughput biological data. Bioinformatics *23*, 2247–2255.

Tyson, D.R., Garbett, S.P., Frick, P.L., and Quaranta, V. (2012). Fractional proliferation: a method to deconvolve cell population dynamics from single-cell data. Nat Methods *9*, 923-928.

Wikipedia (2015). Principal component analysis (https://en.wikipedia.org/wiki/Principal_component_analysis: Wikipedia, the free encyclopedia).

Xia, X., Owen, M.S., Lee, R.E., and Gaudet, S. (2014). Cell-to-cell variability in cell death: can systems biology help us make sense of it all? Cell Death Dis *5*, e1261.

Yang, R., Niepel, M., Mitchison, T.K., and Sorger, P.K. (2010). Dissecting variability in responses to cancer chemotherapy through systems pharmacology. Clin Pharmacol Ther *88*, 34-38.

Yano, S., Zhang, Y., Miwa, S., Tome, Y., Hiroshima, Y., Uehara, F., Yamamoto, M., Suetsugu, A., Kishimoto, H., Tazawa, H.*, et al.* (2014). Spatial-temporal FUCCI imaging of each cell in a tumor demonstrates locational dependence of cell cycle dynamics and chemoresponsiveness. Cell Cycle *13*, 2110-2119.

Yegnasubramanian, S., and Maitra, A. (2013). Aiming for the outliers: cancer precision medicine through targeting kinases with extreme expression. Cancer Discov *3*, 252-254.

Zhang, J., Yang, P.L., and Gray, N.S. (2009). Targeting cancer with small molecule kinase inhibitors. Nat Rev Cancer *9*, 28-39.

8. APPENDIX

1.6 List of figures

Figure 1.1 Drug discovery and development paradigm. 7

Figure 1.2 Variability in shape of drug-response behavior in breast cancer cell line. 10

Figure 1.3 Characteristics of heterogeneous and homogeneous signaling responses for different forms of measurements. 12

Figure 2.1 Nominal targets of ligand and kinase inhibitor panel. 16

Figure 2.2 Antibodies tested for immunofluorescence imaging. 18

Figure 2.3 Antibodies used for high-content immunofluorescence imaging and drug screening. 19

Figure 2.4 Antibodies used for cyclic immunofluorescence (CycIF) ligand response and drug screen. 20

Figure 2.5 High-content/high-throughput IF and CycIF imaging pipeline............ 26

Figure 2.6 CycIF imaging method variants. 29

Figure 2.7 Parameterization of dose-response curves. 34

Figure 2.8 Growth inhibition curves. 35

Figure 2.9 Parameters derived from drug response measured by relative ATP content. 36

Figure 3.1 Measurement of drug potency by pairwise combinations of two parameters.. 40

Figure 3.2 Measurement of drug efficacy and hill slope reveals clusters based on drug target. 41

Figure 3.3 Averaged signal analysis reveals significant molecular complexity underlying phenotypic differences. 42

Figure 3.4 MAPK dynamics in response to EGFR/HER2 inhibiting by lapatinib. 43

Figure 3.5 Linear correlation between dynamics of p-ERK1/2 and growth inhibition.. 44

Figure 3.6 p-ERK1/2 recovery is an induced state. 46

Figure 3.7 p-ERK1/2 recovery is not regulated by an autocrine loop activation. 47

Figure 3.8 Recovery of MAP kinase signaling is regulated at the receptor level. 48

Figure 3.9 Total EGFR localizations in response to lapatinib in full serum. 49

Figure 3.10 Recovery of EGFR phosphorylation is accompanied by EGFR translocation to plasma membrane. 50

Figure 3.11 Sustained inhibition of p-ERK1/2 by drug combination. 51

Figure 3.12 Combination of EGFR targeting drugs leads to sustained inhibition of proliferation signaling. 52

Figure 3.13 Principal component analysis (PCA) of drug effects clusters inhibitors that have similar nominal targets. 54

Figure 3.14 Principal component analysis (PCA) of drug effects clusters inhibitors that have similar nominal targets. 55

Figure 3.15 Representative images of graded and on or off signals. 56

Figure 3.16 Single-cell fractions better predict growth inhibition phenotype. 57

Figure 3.17 Molecular details of cytostasis are different from one drug to the next. 59

Figure 3.18 *k*-means clustering in unperturbed cells reveals existence 3 distinct cellular states corresponding to cell cycle. 61

Figure 3.19 Principal component analysis (PCA) of CycIF data is consistent with conventional IF data. 62

Figure 3.20 Single-cell projection on *k*-means clusters in PCA space reveals differential cytostatic states. 63

Figure 3.21 DMSO-treated cells in viSNE space are inseparable. 64

Figure 3.22 viSNE analysis of perturbed cells implies drug specific induced subpopulations. 65

Figure 3.23 viSNE analysis of single drugs implies similarity in single-cell phenotypes across drug target subsets. 66

Figure 3.24 viSNE analysis of drug induced domains across 12 signals reveals distinct signaling states across different drugs. 67

Figure 3.25 Torkinib resistant subpopulation is in S/G_2 cell cycle phase and enriched with markers of proliferation. 68

Figure 3.26 Single-cell distribution of cell cycle markers in viSNE space combined with Wanderlust axis recapitulates direction of cell cycle progression. 69

Figure 3.27 Reconstruction of cell cycle progression by Wanderlust analysis of static cell cycle regulator markers. 70

1.7 List of tables

Table 1 List of primary antibodies for ligand and drug response. 25

Table 2 List of secondary antibodies for ligand and drug response. 27

Table 3 List of filters used for IF imaging. 27

Table 4 List of conjugated antibodies used in CycIF. 30

1.8 List of equations

Equation 1 32

1.9 Publications derived from this work

Saman Honarnejad, Jia-Ren Lin, Samuel Bandara, Mathias Hafner, Peter K. Sorger. Measuring drug response in cancer cells using well-average and single-cell multiplexed imaging assays, *Nature Scientific Data* (2016, in revision)

Mohammad Fallahi-Sichani, Saman Honarnejad, Laura M Heiser, Joe W Gray, Peter K Sorger. Metrics other than potency reveal systematic variation in responses to cancer drugs, *Nature Chemical Biology* (2013).

9. CURRICULUM VITAE

PERSONAL DATA

Name:	Saman Honarnejad
DOB:	21.09.1983
POB:	Tehran, Iran
Marital Status:	Single
Father:	Rahim Honarnejad
Mother:	Rouhangiz Eatemad

SCHOOL (EDUCATION)

(1989) – (1990)	Elementary School: Ghods Public School, Rasht, Iran
(1990) – (1991)	Elementary School: Ghods Private School, Rasht, Iran
(1991) – (1992)	Elementary School: W. P. Bate, Saskatoon, Canada
(1992) – (1994)	Elementary School: Ghods Private School, Rasht, Iran
(1994) – (1997)	Middle School: Abooreyhan Private School, Rasht, Iran
(1997) – (2000)	High School: Koushyar Private School, Rasht, Iran
(25 September 2001)	Pre-University Course: Koushyar Private School, Rasht, Iran

UNIVERSITY (EDUCATION)

WS2004	Biotechnology
	Mannheim University of Applied Sciences
01 March 2009	Bachelor of Science (B.Sc.)
SS2009	Biotechnology
	Mannheim University of Applied Sciences
(2009) – (2010)	Dissecting the Consequence of Cell-to-Cell Variability on Drug Response in Human Breast Cancer Cells
01 September 2010	Master of Science (M.Sc.) Note: 1.8

10. ACKNOWLEDGMENT

There are many people to thank for making this thesis work possible. First, I would like to thank both my advisors, Mathias Hafner at the Institute for Medical Technology of Heidelberg University and Mannheim University of Applied Sciences for scientific supervision, guidance and unlimited personal support and Peter Sorger at the Department of Systems Biology, Harvard Medical School for providing me with an exciting research environment that changed my view of the state-of-the-art biomedical research. During my stay in his lab, Peter allowed me to freely peruse my scientific interests and generously supported me with extreme patience. Because of this, I was exposed to an approach to biology previously unknown me. I learned a diverse set of techniques and gained new skills.

I would also like to thank my collaborators who contributed to this project, both experimentally and computationally. Experimental methods developed by Jia-Ren Lin and help with the computational analysis frameworks from him and Samuel Bandara formed the backbone of my project, for which I am extremely grateful. Collaboration with Mohammad Fallahi-Sichani at the early stages of my thesis was very valuable for setting the basis of my dissertation. Laura Kleiman, Mario Niepel, Bjorn Millard, William Chen and Verena Becker were also helpful teachers and advisors when I first joined the lab, and freely provided advice, constructs and cell lines. I would like to thank Joshua Sims and Laura Kleiman for their biochemistry expertise, invaluable technical assistance, discussions, experimental help and fresh outlook on my project and Mirra Chung for the help with cell culture material. I thank Chris Bird for administrative help throughout my stay in Sorger lab. Also, I appreciate the help of current and former members of Sorger and Hafner labs who all contributed in various ways to this project.

Last but not least, I would like to deeply thank my family for their unconditional support. Specifically, my father and brother who are both scientists and their advice always came handy at different stages of my higher education as well as my mother for her guidance throughout my life. Finally, I would like to thank my brother Kamran again for carefully reading my thesis and my friend Shirin who had an enormous role in my scientific and personal life.